Charles University in Prague

Faculty of Mathematics and Physics

DOCTORAL THESIS

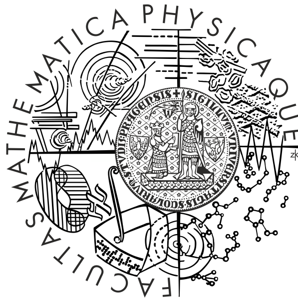

Martin Dubau

Preparation and Characterization of Porous Cerium Oxide/Carbon Bilayers on Silicon Substrates

Department of Plasma and Surface Science

Supervisor: doc. Mgr. Iva Matolínová, Dr.

Study programme: Physics

Study branch: 4-f5 Physics of Surfaces and Interfaces

Prague 2016

I declare that I carried out this doctoral thesis independently, and only with the cited sources, literature and other professional sources.

I understand that my work relates to the rights and obligations under the Act No. 121/2000 Sb., the Copyright Act, as amended, in particular the fact that the Charles University in Prague has the right to conclude a license agreement on the use of this work as a school work pursuant to Section 60 subsection 1 of the Copyright Act.

PRAGUE, 26.07.2016 signature of the author

Title: Preparation and Characterization of Porous Cerium Oxide/Carbon Bilayers on Silicon Substrates

Author: Martin Dubau

Department: Plasma and Surface Science

Supervisor: doc. Mgr. Iva Matolínová, Dr.

Abstract:
This doctoral thesis concerns the preparation of porous cerium oxide/carbon bilayers on silicon substrates. In this regard, carbonaceous films in the form of amorphous carbon (a-C) and nitrogenated amorphous carbon (CN_x) are considered. The influence of various process parameters of the cerium oxide deposition on the morphology of the final cerium oxide/carbon bilayer is investigated. A correlation could be found between the morphology of the bilayer and the stoichiometry of the cerium oxide film determined by means of XPS. Furthermore, a study regarding the chemical composition of the used carbonaceous films by means of various spectroscopic techniques is presented. It was found that the chemical composition of the carbonaceous films strongly depends on the deposition conditions of these films and influences the behaviour of these films during oxygen plasma treatment and cerium oxide deposition, respectively.

Keywords:
Magnetron sputtering, porous cerium oxide, nitrogenated amorphous carbon, oxygen plasma treatment, chemical composition

Contents

I Introduction 8

1 Motivation and aim of the work 9

1.1 Introduction . . . 9
1.2 Deposition of porous cerium oxide films — state of the art . . . 10
1.3 Carbon-based thin films — a short review . . . 11
1.3.1 Amorphous carbon films . . . 11
1.3.2 Nitrogenated amorphous carbon films . . . 13
1.4 Aim of the work . . . 15

II The used experimental methods and techniques 17

2 Film preparation 19

2.1 The used substrates . . . 19
2.2 Magnetron sputtering . . . 19
2.2.1 Fundamentals of the sputtering technique . . . 19
2.2.2 Deposition of the carbonaceous films . . . 21
2.2.3 Cerium oxide deposition . . . 21
2.2.4 Deposition of platinum-doped cerium oxide films . . . 22
2.3 Oxygen plasma treatment . . . 23

3 Film characterization 24

3.1 Scanning electron microscopy . . . 24
3.1.1 Surface morphology . . . 25
3.1.2 Determination of the elemental composition . . . 25
3.2 Atomic force microscopy . . . 25
3.3 Transmission electron microscopy . . . 26
3.3.1 Cross-sectional view of the prepared films . . . 26
3.3.2 Electron energy loss spectroscopy . . . 26
3.4 Photoelectron spectroscopy . . . 27
3.4.1 Fitting of the PES spectra . . . 30
3.5 Near-edge X-ray absorption fine structure spectroscopy . . . 30
3.5.1 Experimetal details . . . 31

III Preparation and morphological properties of car-

bonaceous films and cerium oxide/carbon bilayers 32

4 Preparation and morphological properties of the carbonaceous films on silicon 33
4.1 Preparation of various carbonaceous films on silicon 33
4.1.1 Deposition of carbonaceous single layers 33
4.1.2 Adhesion improvement of the deposited films on silicon substrates 34
4.1.3 Concluding remarks 35
4.2 Investigation of the morphological properties 37
4.2.1 Information about the used samples 37
4.2.2 Morphological properties investigated with SEM and AFM 37

5 Oxygen plasma treatment of the carbonaceous films 39
5.1 Information about the prepared samples 39
5.2 Oxygen plasma treatment of the carbonaceous films on silicon . . 39
5.2.1 Determination of the etching rate 39
5.2.2 Morphological modifications 40
5.3 Oxygen plasma treatment of the bulk substrates 41

6 Morphology of cerium oxide/carbon bilayers on silicon 46
6.1 Deposition of cerium oxide films in argon/oxygen gas mixtures . . 46
6.1.1 Influence of the oxygen concentration in the process gas . . 46
6.1.2 Influence of the cerium oxide film thickness 50
6.1.3 Influence of the cerium oxide deposition rate 51
6.1.4 Influence of the type of the used carbonaceous interlayer . 52
6.1.5 Determination of the CN_x material erosion during cerium oxide deposition 54
6.2 Deposition of cerium oxide films in mixtures argon/hydrogen . . . 55
6.3 Deposition of cerium oxide films in mixtures argon/water vapour . 55

7 Preparation and morphology of platinum-doped cerium oxide films on various substrates 58
7.1 Information about the prepared samples 58
7.2 Deposition of CeO_x-Pt films on silicon 59
7.2.1 Determination of the platinum concentration by means of XPS 59
7.2.2 Morphological investigations 59
7.3 Deposition of CeO_x-Pt films on nanoGDL 60

IV Elemental and chemical composition of the carbonaceous films 63

8 Determination of the element composition of the carbonaceous films on silicon 64
8.1 Composition of the as-prepared films 64
8.1.1 Information about the used methods and samples 64
8.1.2 Determination of the nitrogen concentration 65

8.1.3 Discussion 66
8.2 Composition of the oxygen plasma treated and cerium oxide covered carbonaceous films 67
8.2.1 Information about the used samples 67
8.2.2 Determination of the nitrogen concentration in the CN_x films 67
8.2.3 Determination of the oxygen concentration 67

9 Investigation of the stoichiometry of the cerium oxide films depending on the deposition conditions 72
9.1 Information about the used samples 72
9.2 Influence of the oxygen partial pressure 73
9.3 Influence of the cerium oxide film thickness 75
9.4 Deposition in argon/oxygen vs. argon/water vapour 77

10 Structural properties of the as-prepared carbonaceous films 78
10.1 Investigation of the bulk properties by means of HAXPES 78
10.1.1 Information about the used samples 78
10.1.2 Results 78
10.2 Depth profiling of the chemical composition 84
10.2.1 Information about the used samples and experimental techniques 84
10.2.2 Results 84

11 Chemical composition of the oxygen plasma treated and cerium oxide covered carbonaceous films 89
11.1 Investigation of the bulk properties by means of HAXPES 89
11.1.1 Information about the used samples 89
11.1.2 Results 89
11.2 Depth profiling of the chemical composition 94
11.2.1 Information about the used samples 94
11.2.2 Results of the oxygen plasma treatment 94
11.2.3 Results of the cerium oxide deposition 98

12 Investigation of the as-prepared, oxygen plasma treated and cerium oxide covered carbonaceous films by means of NEXAFS 102
12.1 Information about the used samples and experimental techniques 102
12.2 Results 102

13 Summary of the main results obtained from the spectroscopic techniques 106
13.1 Correlations between the PES and NEXAFS 106
13.2 Correlations between the chemical composition and the etching behaviour of the CN_x films in oxygen plasma and cerium oxide deposition 107

Concluding remarks 110

Summary and conclusions 110

Bibliography **117**

List of figures **122**

List of tables **123**

Abbreviations **124**

Poděkování **125**

Part I

Introduction

Chapter 1

Motivation and aim of the work

1.1 Introduction

The limited availability of fossile fuels as well as the well-known problems connected with their burning – including air pollution and greenhouse effect – encourage the development of novel methods of power generation. In this regard, alternative methods of electric power generation by means of renewable energy sources, such as wind and solar energy, are one important part in order to replace the conventional thermal and nuclear power plants. Another aspect focuses on alternative methods of powering of cars, which form an integral part of our mobility-based society. Therefore, electrically driven cars are an interesting option in order to reduce the dependence on fossile fuels. The electricity used for powering the car has to be either stored by means of accumulators or produced environmentally friendly directly on board of the vehicle. The first aspect requires accumulators allowing the long-lasting storage of a sufficiently high amount of electric energy. An interesting solution for the second aspect regarding the onboard power generation are fuel cells. Fuel cells take advantage of the direct conversion of chemical energy into electricity using the reaction between hydrogen and oxygen [1]. Effective catalysts are the key part of a fuel cell with high performance. For this purpose, usually platinum-based alloys are used [2]. The main advantages of hydrogen fuel cells are the following [3]:

- no fossile fuels required
- no production of greenhouse gases such as CO_2
- high efficiency

However, the operation of fuel cells is connected with several disadvantages [2]:

- high costs due to a large amount of the used platinum
- degradation of the catalyst and the catalyst support

Accordingly, the improvement of the catalyst is the most important task in order to improve the performance of the whole fuel cell.

Cerium oxide-based thin films — a novel catalyst for fuel cells; micro fuel cells. In recent years, cerium oxide-based materials such as Pt-cerium oxide have received much attention due to their excellent catalytic properties for a variety of reactions [4–7]. Among others, fuel cells offer an interesting application field of these materials. In the studies [8, 9] it was shown that sputtered thin Pt or Sn containing cerium oxide films, which had been deposited on the anode side of a fuel cell, exhibited a higher specific power compared to a conventional Pt-Ru catalyst. Beside the large scale fuel cells there is also an increasing interest in miniature fuel cells fabricated on silicon [10, 11], which could be used as an on-chip power supply for portable electronic devices. However, a large active surface is generally an important requirement to improve the catalytic performance of catalysts. This leads to difficulties especially if thin film catalysts have to be realized on flat substrates such as silicon. One possibility to overcome this problem is a modification of the silicon substrate itself. Porous silicon is often used as a catalyst support, gas diffusion layer or even as a membrane in micro fuel cells [10, 12]. The fabrication of porous silicon is usually realized via electrochemical etching of silicon in a HF containing solution. An alternative to this method is the direct deposition of porous thin film catalysts on the flat silicon substrate. In the previous studies [9, 13–15] it was shown that magnetron sputtered cerium oxide-based thin film catalysts exhibit a porous structure on carbon nanotubes and glassy carbon substrates. This effect was explained to be the result of an etching process of the carbon substrate by oxygen species (ions, radicals...), which occurs simultaneously with the cerium oxide deposition.

1.2 Deposition of porous cerium oxide films — state of the art

The formation of porous cerium oxide-based thin films prepared by RF magnetron sputtering has been reported by Václavů et al. on carbon nanotubes (CNTs) for the first time [8]. In the following years, the formation of cerium oxide films with high porosity has been shown for other substrates including glassy carbon [15] and graphite foil [16]. Haviar et al. investigated the influence of various process parameters of the cerium oxide sputter-deposition on the morphology of the final cerium oxide film [17]. In this study, sputtered amorphous carbon films (a-C) on silicon served as substrates. The influence of several process parameters of the cerium oxide deposition process — namely the process gas composition, the deposition rate as well as the duration of the deposition (film thickness) — on the surface morphology and the thickness of the resulting cerium oxide/a-C bilayer was investigated. The results of this study clearly reveal that the addition of a sufficient amount of oxygen to the process gas leads to the growth of highly porous cerium oxide films accompanied by etching of the a-C interlayer. On the other hand, a too high oxygen concentration in the process gas delivers cerium oxide films with a compact surface. Likewise, the deposition rate has to be sufficiently low in order to achieve porous cerium oxide film growth. Based on these experimental observations, a growth model of cerium oxide films was proposed, which is valid for cerium oxide films prepared via magnetron sputtering of a cerium oxide target using argon/oxygen as the process gas, if carbonaceous

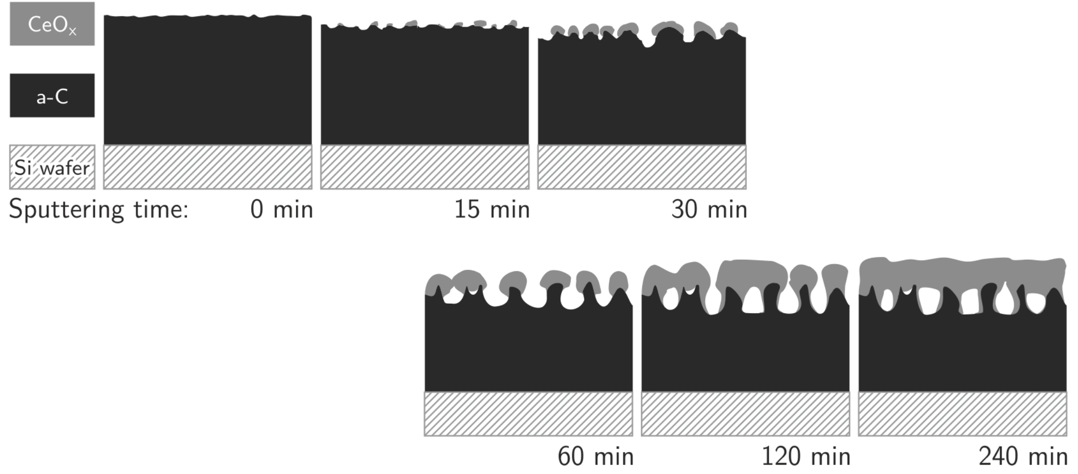

Figure 1.1: Growth model proposed for cerium oxide films prepared on an amorphous carbon on silicon via magnetron sputtering of a cerium oxide target using an argon/oxygen gas mixture as the process gas [17].

materials are used as substrates (see fig. 1.1). According to this model, the growth of porous cerium oxide films on a-C films on silicon (or any other carbonaceous substrate) can be divided into the following steps:

1. *Nucleation and etching:* During the first stage of cerium oxide film growth, nuclei of cerium oxide form on the surface of the nearly flat a-C film. The area between the nuclei is in contact with the plasma and chemically etched with oxygen species under formation of carbon-containing gaseous products, such as CO and CO_2. The cerium oxide nuclei act as an etching mask preventing etching of the carbon film below the cerium oxide nuclei. The etching leads to a reduction of the thickness of the a-C film.

2. *Growth of the nuclei and proceeding of the etching:* The cerium oxide nuclei grow into larger objects. Simultaneously, etching of the a-C film continues.

3. *Coalescence of the cerium oxide objects:* The growth of the cerium oxide objects continues until a compact film is formed due to coalescence. The etching of the a-C film is supressed at this stage of cerium oxide film growth due to masking of the whole a-C film.

A sufficiently low deposition rate is crucial in order to achieve etching of the carbon film. A high cerium oxide deposition rate leads to a fast masking of the whole carbon film. As a result, etching of the a-C support is suppressed.

1.3 Carbon-based thin films — a short review

1.3.1 Amorphous carbon films

Amorphous carbon films (a-C) have been deposited by Aisenberg and Chabot for the first time [18, 19]. These films exhibit properties, which are very close to that of diamond. For this reason, amorphous carbon films are interesting

for several applications, including e. g. the use as coatings for wear protection. However, in contrast to diamond these films are amorphous.

For the preparation of such films, several PVD[1] and CVD[2] methods are available. The latter allows the preparation of hydrogen-containing carbon films (a-C:H) only. One widely used preparation method is the magnetron sputtering technique [20, 21]. For this purpose, graphite targets are used. The process gas is usually argon.

Structural properties of amorphous carbon films. Carbon as an element of the 4th main-group has four valence electrons, two of which being s- and two being p-electrons. However, one of the two s-electrons can be excited to the p-state with low energy input. In order to describe bonding configurations of carbon, for example in molecules, the *hybridization model* is often used [22, 23]. In the frame of this model, an appropriate linear combination of the wave functions of the s- and p-electrons is performed, which delivers the optimal description of the given bonding relation. The mathematical background is delivered by the *time-independent quantum mechanical perturbation theory* of a degenerated energy level. It is considered that the energy difference between the s- and p-electrons of the excited carbon atom vanishes due to COULOMB-interaction caused by the proximity of other atomic nuclei (e. g. in molecules). For the following considerations, two bonding configurations of carbon are of fundamental interest. These can be described in the frame of the hybridization model as follows:

- sp^2 *configuration:* In this configuration, three sp^2 hybrid orbitals lying in one plane obtained from the linear combination of the s- and two p-orbitals are attributed to one carbon atom. The remaining p-orbital is not involved in the hybridization and is oriented perpendicular to this plane. One important example, where this bonding configuration of carbon can be found, is graphite; the crystal structure is shown in fig. 1.2 a). Graphite is a *layered material* consisting of *graphene layers*. Within one graphene layer, the carbon atoms are bound to each other via covalent bonds realized by the sp^2 hybrid orbitals. Between the individual graphene layers, only a weak VAN-DER-WAALS interaction is present.

- sp^3 *configuration:* In this configuration, four sp^3 hybrid orbitals obtained from the linear combination of the s- and the three p-orbitals are attributed to one carbon atom forming a tetrahedron. The crystalline representative of this bonding configuration is *diamond*, the crystal structure of which is shown in fig. 1.2 b). Diamond exhibits several extraordinary properties, including a high hardness. In contrast to graphite, diamond is an electrical insulator. Furthermore, diamond is only a metastable phase at normal conditions in contrast to graphite, which is thermodynamically stable.

In amorphous carbon films, usually both bonding configurations of carbon can be found leading to a broad structural variability of this type of films [24]. The limiting cases of mainly graphite-like and mainly diamond-like short-range order are discussed in the following paragraph.

[1] **P**hysical **V**apour **D**eposition
[2] **C**hemical **V**apour **D**eposition

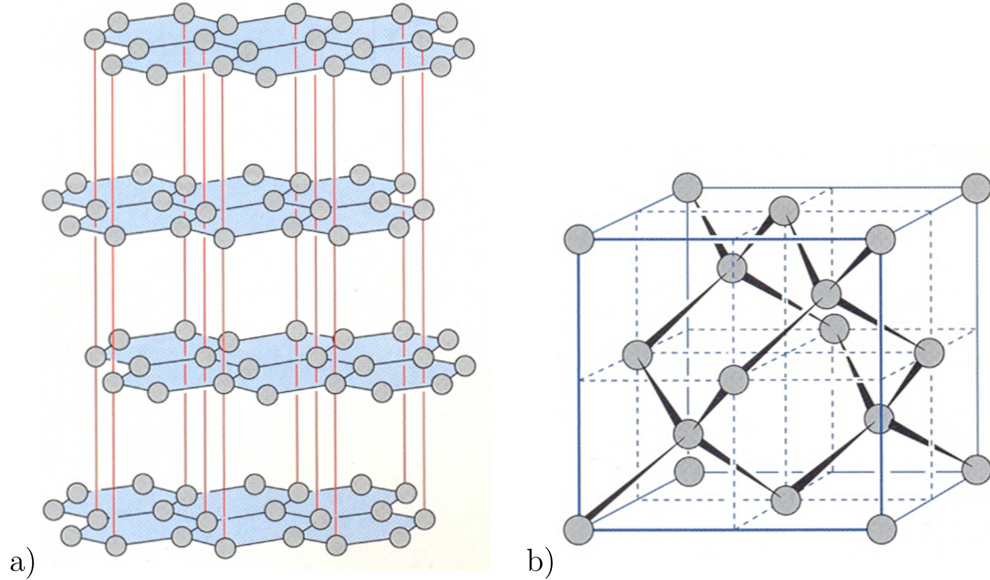

Figure 1.2: Schematic view of the crystal structure of a) graphite and b) diamond (taken from [22]).

- *Mainly diamond-like near-range order:* Especially the high hardness of amorphous carbon films is usually attributed to a high fraction of sp^3 hybridized carbon [25]. These films can exhibit sp^3 fractions up to 80%. Due to the dominating influence of tetrahedrally bonded carbon, the term ta-C was chosen for this type of films[3]. It was found out that the preparation of amorphous carbon films with a high fraction of tetrahedrally bonded carbon requires particle energies in the range 50 — 100 eV for the layer forming particles during film growth [26]. At these conditions, a process called *subplantation* takes place.

- *Mainly graphite-like near-range order:* Tamor and Wu proposed the model of a *disturbed graphite structure* for the description of amorphous carbon films with a fraction of tetrahedrally bonded carbon $< 10\%$ [27]. According to this model, locally parallel graphene layers are interconnected with randomly distributed sp^3 hybridized carbon atoms.

It can be concluded that amorphous carbon films cover a broad range of possible structures determining the mechanical, electrical and optical properties of these films. These properties can be influenced by the process conditions during the film deposition.

1.3.2 Nitrogenated amorphous carbon films

In 1982, Cohen formulated the assumption that a compound consisting of carbon and nitrogen exhibiting an extraordinary high hardness could exist [28]. A few years later, theoretical calculations led to the prediction of the hypothetical $\beta-C_3N_4$ structure [29]. The expected properties of that structure were determined

[3] **t**etrahedral **a**morphous **c**arbon

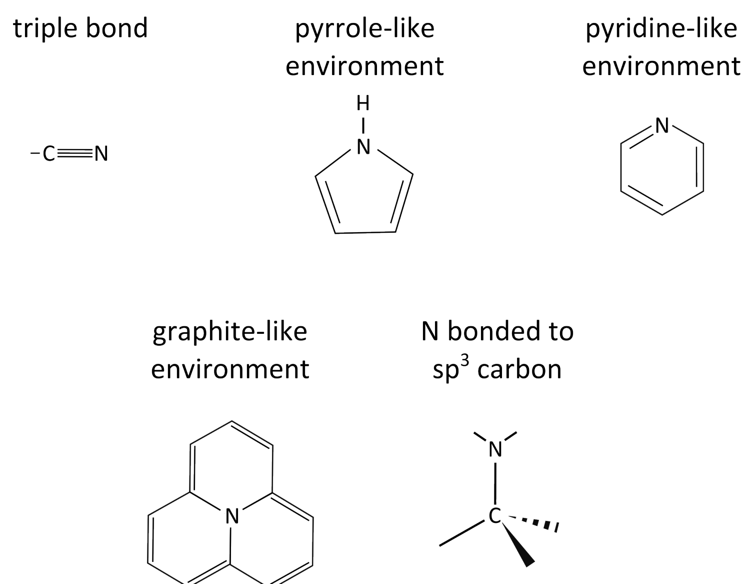

Figure 1.3: Schematic view a various C—N bonding configurations.

via model calculations. These calculations revealed that the $\beta - C_3N_4$ structure should have a bulk modulus comparable to that of diamond. For this reason it is understandable, why extended efforts have been performed in order to synthetize this phase. However, the CN_x films prepared in this regard are usually amorphous and exhibit maximal nitrogen concentration of 40%, which is considerably less than it is expected for the $\beta - C_3N_4$ phase.

Nitrogenated amorphous carbon films are likewise prepared via various PVD and CVD methods. However, reactive magnetron sputtering is an extensively used method for the deposition of these films [30–32]. As in case of the amorphous carbon films, graphite targets are used for this purpose. Gas mixtures of argon and nitrogen or pure nitrogen are usually used as the process gas.

Structure of CN_x films. Nitrogen is chemically incorporated into the carbon film. There are several possibilities how nitrogen can be incorporated into the carbon network leading to an even greater structural variability of CN_x in comparison with amorphous carbon films. The most important bonding configurations of carbon and nitrogen frequently discussed in the literature concerning nitrogenated amorphous carbon films are the following (see fig. 1.3) [33–35]:

- *Triple bond/nitriles:* In this bonding configuration, nitrogen is bound to carbon via a triple bond.
- *Pyridine-like environment:* Nitrogen is bound to two sp^2 hybridized carbon atoms as in pyridine.
- *Pyrrolic nitrogen:* This bonding configuration means a pentagon of carbon atoms, where one C-atom is substituted by a nitrogen atom as in pyrrole.
- *Graphite-like environment:* Nitrogen substitutes one carbon atom in a graphitic network.

- *Nitrogen bound to sp^3 hybridized carbon:* In this bonding configuration, nitrogen is bound to four-coordinated carbon.

The structural properties of CN_x films are usually investigated by means of spectroscopic techniques including X-ray photoelectron spectroscopy (XPS) [34, 35], Near-edge absorption fine structure spectroscopy (NEXAFS) [36, 37], Infrared (IR) spectroscopy [31] and Raman spectroscopy [31].

1.4 Aim of the work

The present work can be considered as a continuation and extension of the works published by Haviar et al. [17, 38] regarding the preparation of porous cerium oxide films on carbonaceous substrates, which is briefly summarized in the previous section. Despite representing a considerable step forward in the view of the realization of highly porous cerium oxide thin film catalysts on silicon substrates for catalytical on-chip applications, the use of interlayers in the form of a-C films delivers cerium oxide/a-C bilayers with a fine porous structure. In contrast, the direct deposition of cerium oxide films e. g. on graphite foil substrates leads to the growth of highly porous cerium oxide films [16]. However, a high porosity is crucial in order to increase the surface area of the cerium oxide-based thin film catalyst. Accordingly, the present study is focused on the modification of the carbon support in such a way that the formation of highly porous cerium oxide/carbon bilayers is enabled. The key part of this study is the introduction of a new type of substrate: *amorphous nitrogenated carbon films (CN_x).* This type of films is usually prepared via magnetron sputtering of a graphite target in a nitrogen-containing process gas [30–32]. If CN_x films have to serve as appropriate substrates for the deposition of porous cerium oxide films, they must exhibit a sufficiently low etching resistance against oxygen plasma in order to achieve sufficiently high material erosion during cerium oxide deposition in the presence of oxygen [17]. Therefore, the investigation of the behaviour of CN_x films in oxygen plasma in comparison with a-C films plays an important role for the present work. Taken as a whole, the work can be divided into the following blocks:

- *Preparation and investigation of the morphological properties of CN_x films deposited on silicon:* This part focuses on the preparation of CN_x films via magnetron sputtering on silicon substrates at various process conditions. The deposited films are investigated with respect to their morphological properties by means of Scanning Electron Microscopy (SEM) and Atomic Force Microscopy (AFM).

- *Investigation of the morphological modifications of CN_x films induced by oxygen plasma:* The main aim of this block is to obtain an insight into the etching behaviour of the CN_x films in oxygen plasma including the determination of the etching rate and morphological modifications in comparison with the as-prepared films. The information obtained from these investigations have practical importance for the preparation of porous cerium oxide/carbon bilayers, because etching of the carbon support with oxygen

species originating from the plasma is the driving force for the formation of these porous structures according to [17].

- *Deposition and morphology of cerium oxide films on silicon using interlayers in the form of CN_x films:* This block covers the preparation of cerium oxide films on CN_x films on silicon via magnetron sputtering at various process conditions. In particular, the influence of several process parameters including the oxygen concentration in the process gas, the cerium oxide deposition rate and the cerium oxide film thickness on the morphology of the final CeO_x/CN_x bilayer is investigated. This includes investigations regarding the cross-sectional structure of the bilayer and the determination of the CN_x material erosion during cerium oxide deposition. Furthermore, it is investigated whether the addition of other reactive gases to the process gas during cerium oxide deposition, namely hydrogen and water vapour, likewise leads to the formation of a porous structure of the final CeO_x/CN_x bilayer.

- *Preparation of porous platinum-doped cerium oxide films on silicon and gas diffusion layer:* This block is focused on the deposition of platinum-doped cerium oxide films, which are more interesting in the view of catalytic applications. It is investigated whether the deposition procedures leading to the porous growth of undoped cerium oxide films can be taken over for the platinum-doped films and to what extend the platinum concentration influences the morphology of the final bilayer. Furthermore, the platinum-doped cerium oxide films are deposited on a gas diffusion layer (GDL), which is a substrate commonly used in fuel cells.

- *Investigation of the chemical composition:* The last block covers the investigation of the chemical composition of the as-prepared, oxygen plasma treated and cerium oxide covered carbonaceous films on silicon. This includes investigations regarding the film composition of the carbonaceous films by means of Energy Dispersive X-ray Spectroscopy (EDX) and Electron Energy Loss Spectroscopy (EELS), as well as the identification of the various C—C and C—N bonds with the use of Photoelectron Spectroscopy (PES) at various primary photon energies (SR-PES, XPS, HAXPES) and Near-edge Absorption Fine Structure Spectroscopy (NEXAFS). In this respect it is investigated, which modifications of the chemical composition are induced by the oxygen plasma and cerium oxide deposition, respectively. In addition, it is examined whether correlations exist between the chemical composition of the carbonaceous films and their etching behaviour during oxygen plasma treatment and cerium oxide deposition, respectively.

This work has practical relevance for the realization of on-chip micro fuel cells on the basis of cerium oxide-based thin film catalysts.

Part II

The used experimental methods and techniques

Chapter 2

Film preparation

2.1 The used substrates

Several substrates were used in the frame of this work:

- *Silicon:* One-side polished silicon wafers with (100) orientation and 500 μm thickness were used. The native oxide layer was *not removed* from the surface.

- *Graphite foil:* A commercial graphite foil (Alfa Aesar, purity 99.8%) was used.

- *Gas diffusion layer with carbon nanoparticles (nanoGDL)*: A commercial nanoGDL (Alfa Aesar) suitable for fuel cell applications was used. A conventional gas diffusion layer consists of carbon nanofibres. The nanoGDL is additionally covered with carbon nanoparticles.

2.2 Magnetron sputtering

2.2.1 Fundamentals of the sputtering technique

Sputtering in general is a technique widely used in science and industries for the preparation of thin films [39]. It is based on the bombardment of a target with inert gas ions with energies in the range of several hundreds of eV, whereby the target consists of the material to be deposited on a substrate. The target atoms gain enough energy this way to leave the target via energy and momentum transfer. The sputtered target atoms are subsequently deposited on the substrate placed in front of the target. For the generation of gas ions, glow discharges are commonly used. The space between two electrodes (labeled cathode and anode) is filled with an inert gas — usually argon — and the glow discharge is ignited via applying a high DC voltage between these electrodes leading to the continuous generation of ion-electron pairs by means of collisions of electrons, which are accelerated in the electric field, with gas atoms.

Magnetron sputtering is a modification of the simple sputtering method described above using the magnetic field of permanent magnets placed below the target (see fig. 2.1). The acting Lorentz-force forces the electrons on spiral trajectories leading to an increase of the path of the electrons during their movement

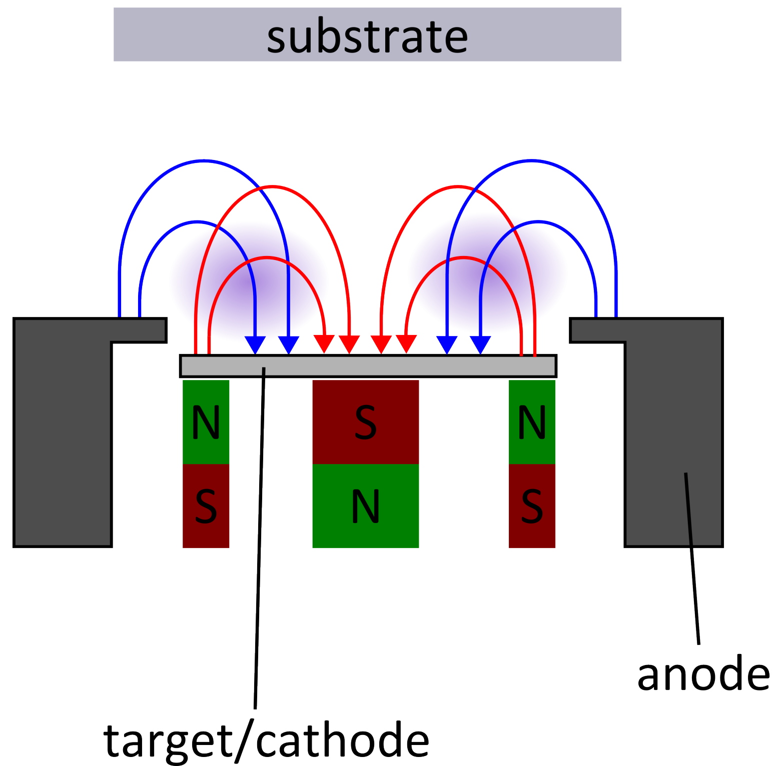

Figure 2.1: Schematic cross-sectional view of a common magnetron sputtering system. Some of the magnetic (red) and electric (blue) field lines are shown for illustration.

to the anode. Accordingly, the probability increases that the electrons collide with the gas atoms making the sputtering process more effective.

Modifications of the basic sputtering system. The basic sputtering system described in the previous paragraph is suitable for the preparation of electrically conductive films only. Due to the use of a DC power supply no discharge can be ignited in case of insulating targets. In order to have the possibility to sputter even non-conductive materials, an RF power supply can be used instead of the DC one. In this case, a sinusoidial alternating voltage with high frequency (usually 13.56 MHz denoted as **r**adio **f**requency) is applied to the target, whereas the anode is grounded. During one period, the target is not only bombarded with positively charged ions, but also with electrons enabling the compensation of positive charge accumulated on the target surface originating from the positive ions.

Another modification of the basic sputtering system is *reactive sputtering*. In this case, a reactive process gas, e. g. nitrogen or oxygen, is used instead of the inert gas [40]. The molecules of the reactive gas can react with the atoms sputtered from the target and are incorporated into the deposited film. One example for the application of this sputtering method is the preparation of *transparent conductive oxides* [41].

2.2.2 Deposition of the carbonaceous films

For the sputter-deposition of the carbonaceous films a commercial sputtering device MED020 of the company Bal-Tec was used. The system is equipped with a *turbomolecular pump* and a *rotary pump* for generating and maintaining the vacuum. The gas pressure is controlled by means of a combined Pirani and Penning gauge. The vacuum chamber can be flooded with argon, nitrogen or mixtures of both. Both gases are introduced into the vacuum chamber via two seperate mass flow controllers (one for each of the two gases). The composition of the process gas was varied by changing the ratio of the gas flows of the two gases, while keeping the total gas flow constant at $\Phi_{\mathrm{total}} = 23\,\mathrm{sccm}$. The corresponding total gas pressure is $\approx 0.8\,\mathrm{Pa}$. In addition, one type of the CN_x films was deposited in pure nitrogen at 4 Pa gas pressure.

A graphite disc (Goodfellow; 2 inch diameter; thickness 1 mm) was used as the target. The magnetron is connected to a DC power supply and is operated in the *constant current mode* with $I_{\mathrm{DC}} = 20\,\mathrm{mA}$. The discharge voltage is automatically adjusted in order to maintain the predefined value of the discharge current I_{DC}. The target-to-substrate distance used for the present study was 50 mm. The maximum substrate temperature achieved during the deposition of the carbonaceous films was measured by means of a thermocouple and does not exceed 100 °C.

2.2.3 Cerium oxide deposition

The cerium oxide films were deposited by means of RF magnetron sputtering. For this purpose, a magnetron sputtering system of own construction was used. This system consists of a vacuum chamber, which is pumped by means of a turbomolecular pump and a membrane pump to a residual gas pressure $< 1 \cdot 10^{-4}\,\mathrm{Pa}$. The gas pressure in the vacuum chamber is controlled with a combined Pirani/Penning gauge. The magnetron is equipped with a cerium oxide target (Kurt Lesker; 2 inch diameter, 0.125 inch thickness, purity 99.99%) and is connected to a RF power supply (Advanced Energy). The cerium oxide deposition rate can be changed indirectly by changing the RF power. The samples were fixed on the grounded substrate holder with conductive tape at a distance of 90 mm above the magnetron. Pure argon, argon/oxygen, argon/hydrogen or argon/water vapour gas mixtures were used as the process gas at a *total pressure* of 0.4 Pa.

- *Deposition in pure argon:* Argon was introduced into the vacuum chamber via a needle valve. The valve was adjusted in such a way that the desired total gas pressure of 0.4 Pa was achieved, which was controlled with the vacuum gauge.

- *Deposition in argon/oxygen:* During the first step, oxygen was introduced into the vacuum chamber via a seperate needle valve. The desired oxygen partial pressure p_{O_2} was adjusted according to the vacuum gauge. In the second step, argon was additionally introduced into the vacuum chamber and adjusted in such a way that the desired total gas pressure of 0.4 Pa was reached.

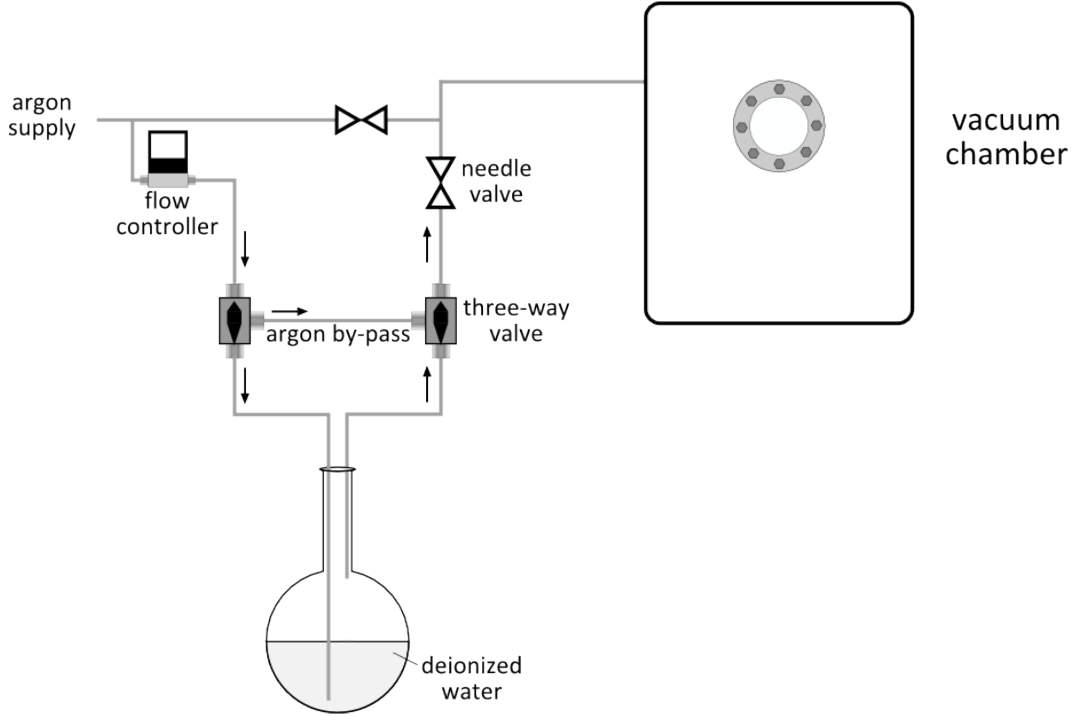

Figure 2.2: Schematic view of the construction used for introducing water vapour into the deposition chamber used for cerium oxide deposition.

- *Deposition in argon/hydrogen:* The same procedure as in case of the deposition in argon/oxygen was applied with hydrogen instead of oxygen.
- *Deposition in argon/water vapour:* In order to introduce water vapour into the deposition chamber in a defined way, a construction shown schematically in fig. 2.2 was used. A flask filled with deionized water forms the key part of this construction. Argon is introduced into the flask through a mass flow controller delivering a constant gas flow of $\Phi_{\mathrm{Ar}} = 4\,\mathrm{sccm}$. The argon serves as a carrier gas for the water vapour. The argon/water vapour gas mixture flows into the vacuum chamber via a needle valve, which is installed in order to have the possibility to change the partial pressure of water vapour in the vacuum chamber.

  The partial pressure of water vapour was determined using the following procedure: First, argon without water vapour was introduced into the vacuum chamber via the installed by-pass; the gas pressure p_{Ar} was measured with the vacuum gauge. In the second step, the argon by-pass was closed and the argon flew into the vacuum chamber through the flask with water; the pressure $p_{\mathrm{Ar+H_2O}}$ was measured with the vacuum gauge. The partial pressure of water vapour $p_{\mathrm{H_2O}}$ was calculated by subtracting both gas pressures, i. e. $p_{\mathrm{H_2O}} = p_{\mathrm{Ar+H_2O}} - p_{\mathrm{Ar}}$.

2.2.4 Deposition of platinum-doped cerium oxide films

The platinum-doped cerium oxide films were prepared in the same way as the undoped ones. Platinum doping was achieved by placing platinum wires on top

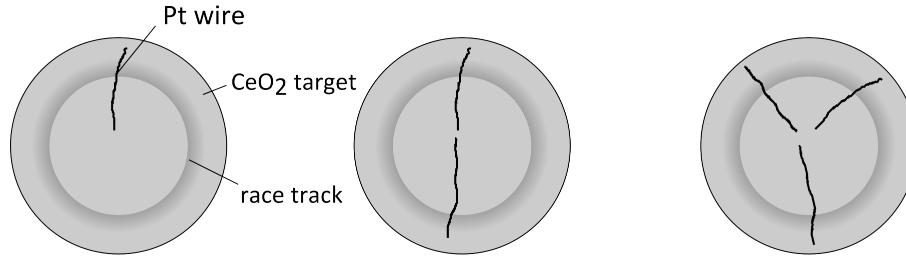

Figure 2.3: Schematic view of the arrangement of the platinum wires on the cerium oxide target used for the deposition of platinum-doped cerium oxide films.

of the cerium oxide target. The arrangement of the platinum wires is shown schematically in fig. 2.3 for three different situations relevant for the present work (one, two and three Pt wires).

2.3 Oxygen plasma treatment

The oxygen plasma treatment of the carbonaceous films was carried out in the MED020 system as well. For this purpose, an etching device schematically shown in fig. 2.4 was placed directly on the substrate holder. A ring-shaped driven electrode forms the key part of this device. Accordingly, the discharge is ignited between this electrode and the grounded substrate holder. The vacuum chamber was flooded with pure oxygen at a pressure of $p_{O_2} = 20\,\mathrm{Pa}$. A needle valve was used for adjusting the desired pressure. The etching device was connected to a DC power supply. The directly adjustable parameter is the discharge current, which was set to $2\,\mathrm{mA}$.

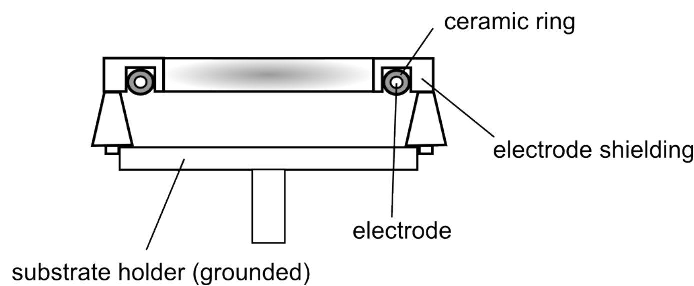

Figure 2.4: Schematic view of the glow discharge device used for the oxygen plasma treatment.

Chapter 3

Film characterization

3.1 Scanning electron microscopy

The Scanning electron microscope (SEM) was used for the investigation of the surface morphology as well as the elemental composition of the prepared films. The SEM utilizes a focused electron beam, which is scanned along the surface of the sample [42]. The most important interaction processes are the following:

- *Generation of secondary electrons:* The interaction between the electron beam and the sample leads to an excitation of electrons in the sample. If the energy transfer is sufficiently high, the excited electrons can leave the sample and are called *secondary electrons*. The secondary electrons originate from a near-surface region of only a few nanometers thickness making the information obtained from this type of electrons very surface sensitive and suitable for investigations regarding the surface morphology of the sample.

- *Electron backscattering:* Another important interaction mechanism is *elastic backscattering* of the electrons of the incident electron beam (primary electrons). The yield of backscattered electrons is extremely sensitive to the mass number of the atoms the sample consists of, which makes this type of electrons suitable for investigations, where material contrast is required. Backscattered electrons originate from regions up to several tens of nanometers below the surface.

- *X-ray emission:* The third important interaction mechanism between the incident electron beam and the sample is the emission of X-radiation. It can be divided into the *characteristic X-radiation* and *Bremsstrahlung*. The latter is correlated with the deceleration of the electrons of the incident electron beam inside the sample. The former describes the emission of photons with discrete energy values, which are characteristic for the elements present in the sample. The Energy-dispersive X-ray spectroscopy (EDX) takes advantage of the characteristic X-radiation emitted from the sample and serves as a tool for determining the elemental composition of the sample. The information depth of the emitted X-radiation is usually several hundreds of nanometers.

For the present study, a microscope Mira 3 from Tescan equipped with an electron gun of the Schottky-type was used. The microscope was used for investigations regarding the morphology and elemental composition.

3.1.1 Surface morphology

For studies related to the surface morphology, secondary electrons were detected by means of a scintillation detector directly integrated into the objective lens of the microscope (*in-beam detector*). The used acceleration voltage was 30 keV; the working distance between the objective lens and the sample was ≈ 3 mm.

3.1.2 Determination of the elemental composition

The elemental composition of the sample was determined by means of detecting the X-radiation emitted by the sample under the influence of the electron beam (EDX). In the frame of the present study, a primary electron energy of 3 keV was used. The complete EDX equipment used in the frame of the present study, i. e. a detector and the software Quantax for acquiring and evaluating of spectra, was delivered by Bruker. The used working distance was 15 mm.

The nitrogen concentration $C_{\mathrm{N}}^{\mathrm{EDX}}$ in the $\mathrm{CN_x}$ films was calculated according to eq. 3.1:

$$C_{\mathrm{N}}^{\mathrm{EDX}} = \frac{K_{\mathrm{N}}}{K_{\mathrm{N}} + K_{\mathrm{C}}} \quad (3.1)$$

The parameters K_{N} and K_{C} stand for the nitrogen (carbon) concentration delivered by the EDX software Quantax.

3.2 Atomic force microscopy

Atomic force microscopy (AFM) belongs to the group of Scanning Probe Microscopes which uses the interatomic interaction between a tip and the surface of the sample to be investigated [43]. It allows 3D imaging of the surface morphology of the sample.

In the frame of the present work the AFM was used for determining the thickness of the prepared films via step-height measurements and for morphological investigations of the carbonaceous films on silicon including the determination of the surface roughness. For this purpose, an AFM of the Multimode type from Veeco was used. The microscope was operated in the tapping mode and was equipped with a cantilever of the FESP type from Bruker; the nominal tip radius for this type of tips is 8 nm. All AFM images were measured with the same type of tip in order to ensure the comparability of the determined values of the surface roughness.

The surface roughness R_{a} was calculated using Nanoscope software from $1\,\mu\mathrm{m} \times 1\,\mu\mathrm{m}$ AFM images and is defined as:

$$R_{\mathrm{a}} = \frac{1}{L_{\mathrm{x}} L_{\mathrm{y}}} \int_0^{L_{\mathrm{y}}} \int_0^{L_{\mathrm{x}}} |f(x,y)| \mathrm{dxdy} \quad (3.2)$$

The tip is scanned along the x-y plane and the height values f are determined for each point (x,y); L_x and L_y stand for the size of the scanned area in x- and y-direction, respectively.

3.3 Transmission electron microscopy

Transmission Electron Microscopy (TEM) was used in order to obtain cross-sectional images of the prepared films. Furthermore, Electron Energy Loss Spectroscopy (EELS) was used for determining the elemental composition of the as-prepared CN_x films. The TEM and EELS study including the sample preparation in the form of lamellas was carried out by V. Potin and J. Lavková in cooperation with the Laboratoire Interdisciplinaire Carnot de Bourgogne of the Université de Bourgogne.

3.3.1 Cross-sectional view of the prepared films

The TEM observations were carried out using a JEOL 2100 (LaB_6) electron microscope with an electron beam energy of 200 keV. The samples for TEM observations in the form of thin lamellas were prepared from the thin film samples by means of a lift-out technique [44] using a dual beam microscope LYRA (SEM-FIB, Tescan) equipped with a gas injection system (GIS). A platinum or silicon oxide protection layer, which simultaneously delivers sufficient material contrast in TEM, was deposited on the surface of each sample. The lamellas were picked up with a tungsten standard probe tip (Omniprobe) and placed on copper TEM grids (Omniprobe). The thickness of each lamella was reduced to approximately 60 nm via a two-step polishing technique using the Focused Ion Beam technique [45]. In the first step, gallium ions at 30 keV kinetic energy were used for rough thinning of the lamella. Subsequently, the ion energy has been reduced to 10 keV in order to minimize the amorphous contamination layer formed on the sample during the first polishing step.

3.3.2 Electron energy loss spectroscopy

Electron Energy Loss Spectroscopy (EELS) takes advantage of inelastic scattering of electrons during their pass through the sample. This allows an elemental and chemical analysis of the investigated sample. In the frame of the present study, this technique was used for the determination of the elemental composition of the CN_x films only. For this purpose, an integration over the carbon and nitrogen edges was carried out using the software Digital Micrograph. The nitrogen concentration C_N^{EELS} was calculated according to the following equation 3.3, where I means the integrated intensity over the corresponding edge:

$$C_N^{EELS} = \frac{I_{N-edge}}{I_{C-edge} + I_{N-edge}} \tag{3.3}$$

More information can be found in [46].

3.4 Photoelectron spectroscopy

Photoelectron Spectroscopy (PES) is based on the photoelectric effect [47, 48]. Depending on the energy of the incident photons. Electrons from different energy levels inside the sample are excited to the vacuum level. For example, X-radiation is suitable for the excitation of core-level electrons. Photoelectron spectroscopy based on X-rays is a useful tool for analyses regarding the elemental composition of the sample. In the frame of the basic description, the kinetic energy of the electron leaving the sample is determined by the energy of the incident photon E_{Ph} and the binding energy of the electron E_{B} according to the following equation (Φ — work function) [47, 48]:

$$E_{\mathrm{Kin}} = E_{\mathrm{Ph}} - E_{\mathrm{B}} - \Phi \tag{3.4}$$

The binding energy E_{B} is specific for each element making this method appropriate for the determination of the elemental composition of the sample. Besides, E_{B} is influenced by the chemical environment of the atom the electron is excited from. This so-called *chemical shift* contains information regarding the chemical composition of the sample. Accordingly, X-ray-based PES delivers information regarding both, the elemental *and* chemical composition.

Considerations regarding the PES information depth. A photoelectron excited inside of the sample has to pass through the sample in order to reach and leave the surface. During its movement, the photoelectron may undergo inelastic interactions with the sample material leading to a loss of its energy. However, only electrons which have not suffered any energy loss are of interest for the PES experiment. For the definition of the information depth d the *inelastic mean free path* λ is of fundamental importance. This quantity defines the distance the electron passes between two inelastic interactions with the sample. On the basis of the inelastic mean free path, the probability P that an electron emitted from the depth d reaches the sample surface can be calculated by the following exponential law [49]:

$$P = \mathrm{e}^{-\frac{d}{\lambda}} \tag{3.5}$$

Figure 3.1 illustrates this dependence schematically. Integration over the shown curve delivers the fraction of electrons that are considered for the definition of the information depth. For example, when the information depth is defined as 3λ and the integration is performed from 0 to 3λ, 95% of the electrons are considered. Accordingly, the determination of the inelastic mean free path λ in a given material is crucial for the determination of the information depth. Commonly, the TPP2M formula developed by Tamuma, Powell and Penn is used for this purpose [50]. Figure 3.2 shows the information depth in a carbon material for electrons originating from C 1s and N 1s levels, respectively, for photon energies relevant for the present work when considering 3λ.

The photoionization cross-section. If a photon strikes the surface of the sample, a photoelectron is emitted with a certain probability. For this reason, a quantity called *photoionization cross-section* labled σ is introduced. The photoelectron cross-section depends (i) on the energy of the incident photon and (ii) on

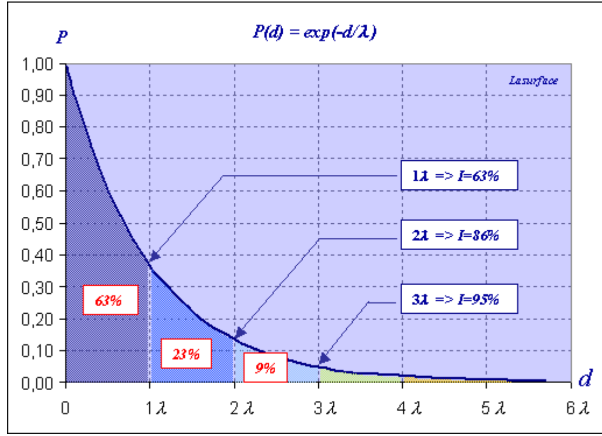

Figure 3.1: Dependence of the probability P that an electron excited at the distance d below the surface reaches the surface of the sample. The quantity d is given in units of the inelastic mean free path of the exited electron (figure taken from [49]).

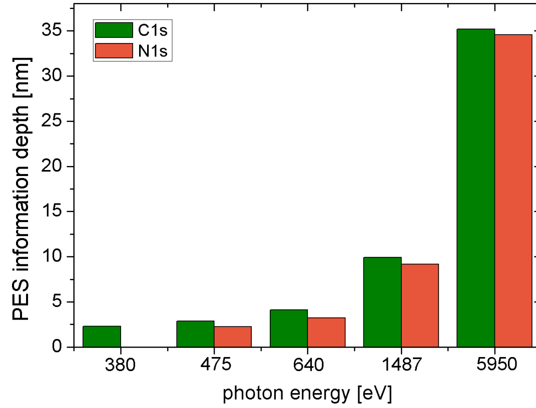

Figure 3.2: Dependence of the PES information depth on the incident photon energy for 3λ.

the atom the photoelectron is emitted from. Accordingly, different elements are commonly not equally sensitive regarding the emission of photoelectrons. This fact has to be taken into account when determining the element concentration in the studied sample quantitatively. The concentration C_1 of an element 1 in the sample may be calculated according to the following equation, where σ_i labels the photoionization cross-section for each individual element i with n denoting the number of elements present in the sample and I_i being the intensity of the peak corresponding to element i:

$$C_1 = \frac{I_1/\sigma_1}{\sum_{i=1}^{n} I_\mathrm{i}/\sigma_\mathrm{i}} \tag{3.6}$$

The photoionization cross-sections for the elements relevant for the present work are given in tab. 3.1 for the considered photon energies. The three PES techniques used in the present work are shortly discussed below.

peak	1487 eV	640 eV	475 eV	380 eV
C1s	0.0137	0.1419	0.3066	0.5254
N1s	0.02451	0.2357	0.4865	—
O1s	0.04005	0.3521	—	—
Ce3d	0.7116	—	—	—
Pt4f	0.227	—	—	—

Table 3.1: Summary of the photoionization cross-sections for the used photon energies taken from the ELETTRA homepage [51].

Synchrotron radiation photoelectron spectroscopy (SRPES). SYNCHROTRON RADIATION PHOTOELECTRON SPECTROSCOPY (SRPES) utilizes synchrotron radiation, which allows the use of radiation with tunable energy. For this reason, the information depth of the detected signal can be likewise tuned.

The SRPES analysis was carried out at the MATERIALS SCIENCE BEAMLINE at the synchrotrone ELETTRA in TRIESTE, Italy. The bending magnet source provides synchrotron light in th energy range of 21 — 1000 eV. The instrumental resolution was ca. 0.3 eV at 380 eV and 0.6 eV at 640 eV. The used photon energies were 640, 475 and 380 eV. The UHV station (base pressure $2 \cdot 10^{-8}$ Pa) is equipped with a SPECS Phoibos 150 electron energy analyzer and a dual Mg/Al X-ray source. The Al Kα anode was used for XPS measurements. The core level N 1s and C 1s spectra were taken at photon energies 380, 475 and 640 eV, respectively, under normal photoemission angle.

X-ray photoelectron spectroscopy (XPS). This technique is widely used due to its relative simplicity regarding the experimental setup. The surface sensitivity of this method is usually in the range of a few nm.

In the frame of the present work, XPS measurements were carried out at two XPS facilities:

1. *Elettra:* These measurements were carried out in the same vacuum chamber as the SRPES analysis, which is described in the previous paragraph. The XPS photoelectron emission angle was 20°.

2. *Prague:* The used system is equipped with an UHV experimental chamber operating at base pressures $< 1 \cdot 10^{8}$ Pa and with a SPECS Phoibos 150 electron energy analyzer as well as a dual Mg/Al X-ray source. The photoelectron emission angle was 0° in this case.

However, for the XPS measurements only the Al Kα anode was chosen (1486.6 eV, total energy resolution $\Delta E = 1$ eV) because the lower photon energy of the Mg Kα X-ray source (1253.6 eV) would lead to higher and more inclined non-linear Ce 3d spectrum background and consequently to lower peak fitting precision

The sensitivity factors used for the determination of the elemental composition are summarized in tab. 3.1, p. 29 for the elements relevant for the present study valid for the used geometry of the experimental setup.

Hard X-ray photoelectron spectroscopy (HAXPES). In this case, hard X-radiation with energies in the range of several keV is used. Photons with such high energies cannot be generated with laboratory X-ray lamps; instead, a synchrotron is necessary as the radiation source.

The HAXPES analysis was carried out at the BL15XU beamline of the NIMS branch at the SPring-8 synchrotoron facility in Japan. X-radiation with photon energy monochromatized to 5950.2 eV using a Si 111 double monochromator and a Si 333 channel-cut post-monochromator was used in the frame of the present work. The measurement was carried out in an experimental ultra high vacuum (UHV) chamber with a base pressure around $2 \cdot 10^{-7}$ Pa equipped with a VG SCIENTA R4000 10 kV hemispherical analyzer. The spectra were taken at the grazing photon incidence and normal emission geometry with total resolution of about 250 meV.

3.4.1 Fitting of the PES spectra

Fitting of the spectra Ce 3d

The spectra Ce 3d were measured by means of XPS. Fitting of the spectra was carried out using the software KolXPD [52]. The fitting procedure described by Skala et al. [53] was used. First of all, charge shift was corrected by setting the peak appearing at the highest binding energy to 916.5 eV. For background modelling, a ranged Shirley-type background was used. In this regard, the whole spectrum was divided into three regions: (1) 877 — 874 eV; (2) 894 — 912 eV; (3) 913 — 928 eV. According to [53], the spectra Ce 3d can be fitted with five doublets of the Voigt-type, three of them related with Ce^{4+} and two related to Ce^{3+}. The doublet located at 882 eV exhibits an asymmetry, which can be modelled with a second Voigt doublet shifted by ≈ 1.3 eV to higher binding energies.

Fitting of the spectra C 1s and N 1s

The spectra C 1s and N 1s were measured by means of SRPES, XPS and HAXPES. These spectra were fitted using the software KoLXPD [52] as well. After charge-shift correction, background modelling of the Shirley-type was performed. Subsequently, the spectra were fitted with four peaks of Gaussian shape and, additionally in case of the C 1s spectra, with one asymetric peak (Doniach Sunjic function).

3.5 Near-edge X-ray absorption fine structure spectroscopy

Near-edge X-ray Absorption Fine Structure Spectroscopy (NEXAFS) is one type of absorption spectroscopy based on X-radiation. In this type of spectroscopy, the sample is irradiated with X-radiation at various energies. During passing the various photon energies from the lowest to the highest, an absorption edge appears at a certain photon energy, which represents the energy

treshold necessary for exciting core-level electrons. In the absorption, typically three regions can be distinguished [54]:

- *Absorption edge:* This term refers to the absorption jump, where the first core-level transitions are energetically allowed.
- *NEXAFS/XANES region:* This region typically extends over some tens of eV above the absorption edge. The kinetic energy of the excited electrons is quite low making multiple scattering effects highly probable, which occur at the nearest-neighbour atoms surrounding the central atom where the excitation occured. The NEXAFS spectra of simple molecules can be interpreted to be the result of electron excitations to unoccuppied valence orbitals and so-called *shape resonances* induced by the multiple scattering process.
- *EXAFS region:* Thie region extends in the energy range from $\approx 40\,\text{eV}$ to $\approx 800\,\text{eV}$. The kinetic energy of the excited electron is sufficiently high so that the electron is only weakly scattered by the neighbour atoms leading to slight modulations of the absorption coefficient.

NEXAFS is usually used for the investigation of molecules adsorbed on surfaces [54, 55]. In molecules, electron excitations to unoccupied molecular orbitals occur during the NEXAFS experiment. These molecular orbitals are labeled σ^* or π^* according to the symmetry of the orbital; the asterisk emphasises that these states are unoccupied. These transitions are commonly called *resonances*.

A large amount of publications regarding the NEXAFS analysis of (nitrogenated) amorphous carbon films can be found indicating that this method is suitable for the identification of the bonding configurations of carbon and nitrogen in these films [37, 56, 57].

3.5.1 Experimetal details

The NEXAFS study was carried out at the Materials Science Beamline of the synchrotrone Elettra in Trieste, Italy as well. The C K-edges (energy range of 275 — 320 eV) as well as the N K-edges (energy range of 390 — 425 eV) of the various carbonaceous films were recorded. The amount of absorbed X-radiation was measured by determining the intensity of generated Auger-electrons for each photon energy making this method a *surface sensitive* one.

For the recording of the absorption spectra it is necessary that the intensity of the incident X-radiation remains constant during passing through the desired energy window. However, this is a requirement which is not fulfilled in real experimental setups used for NEXAFS experiments. The X-radiation undergoes various energy-dependent modulations, e. g. due to the energy-dependence of the transmission function of the monochromator. For this reason, the raw NEXAFS spectra were normalized to the incident photon flux. The energy resolution for the C and N K-edge NEXAFS spectra was estimated to be 0.23 and 0.38 eV, respectively. The polarisation of light from the beamline has not been measured, but it is assumed to be 90% linear, as the source is a bending magnet.

Part III

Preparation and morphological properties of carbonaceous films and cerium oxide/carbon bilayers

Chapter 4

Preparation and morphological properties of the carbonaceous films on silicon

The first part of this chapter focuses on the preparation of carbonaceous films in the form of a-C and CN_x films on silicon substrates. It is described that delamination was observed for most of the thick single layers and how this delamination problem was solved. The second part of the chapter deals with the morphological properties of the carbonaceous films on silicon investigated by means of SEM and AFM.

4.1 Preparation of various carbonaceous films on silicon

4.1.1 Deposition of carbonaceous single layers

During the first step of film preparation, carbonaceous single layers with a film thickness of ≈ 200 nm were deposited in various argon/nitrogen gas mixtures on silicon substrates. However, delamination was observed in some cases. Table 4.1 summarizes the prepared films and whether film delamination was observed or not. It is obvious that only the a-C and the CN_x film deposited in 100% nitrogen

concentration of N_2 in process gas	total gas pressure [Pa]	delamination
0%	0.8	no
5%	0.8	yes
25%	0.8	yes
50%	0.8	yes
75%	0.8	yes
100%	0.8	yes
100%	4	no

Table 4.1: List of the deposited thick CN_x films.

at the higher process gas pressure of 4 Pa exhibit perfect adhesion to the silicon substrate.

There are two possible reasons for the observed delamination:

1. Unsufficient adhesion of the film to the substrate
2. High intrinsic stress

It is very likely that a combination of both reasons is responsible for the delamination. Accordingly, it was necessary to improve the adhesion of the carbonaceous films to the silicon substrate.

4.1.2 Adhesion improvement of the deposited films on silicon substrates

According to the previous section, there are the following possibilities to solve the observed delamination problem:

1. *Improvement of the film adhesion:* This could be achieved via the use of adhesive interlayers. Due to the fact that pure a-C films exhibit an excellent adhesion to the silicon substrate it would be the easiest way to achieve this with an a-C layer. The deposition of such a a-C/CN_x multilayer is possible in-situ without any target exchange.
2. *Deposition of thinner films:* The preparation of thinner films reduces the forces at the interface between the film and the substrate. Accordingly, no delamination should occur if the film thickness is sufficiently low.
3. *Reduction of the intrinsic stress:* The reduction of intrinsic stresses in carbonaceous films is possible via incorporation of hydrogen [58] or the use of multilayers.

However, the last point requires a modification of the sputtering system used for the deposition of the carbonaceous films. Likewise, the preparation of multilayers is connected with considerable efforts regarding the film preparation. Accordingly, it was decided to focus on the first two points in order to prevent delamination of the carbonaceous films.

This section gives a short overview about how this delamination problem was solved. The used layer systems are schematically shown in fig. 4.1. Table 4.2 summarizes the layer systems prepared in the frame of this study.

Deposition of single layers with a significantly reduced film thickness. In order to keep the deposition process as simple as possible single CN_x layers with a reduced film thickness of ≈ 100 nm were deposited. It can be seen from tab. 4.2 that film delamination occured for almost all of the deposited films, which was observed with a delay of appproximately 2 weeks after the film deposition. Therefore, further improvement is required.

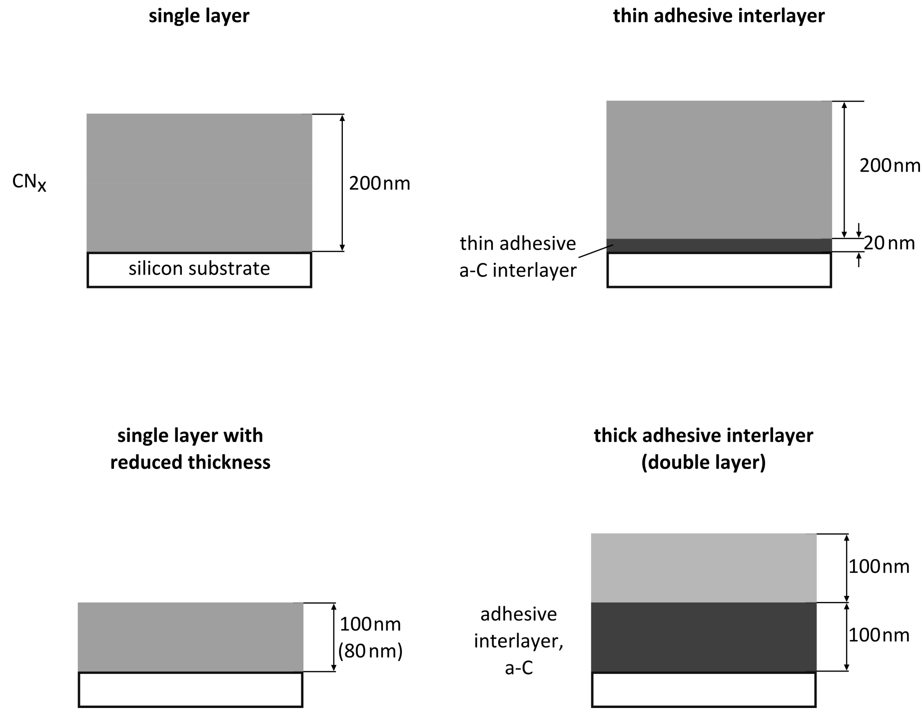

Figure 4.1: Schematic view of the layer systems prepared for the study regarding the adhesion improvement of carbonaceous films on siicon substrates.

Deposition of single layers with a further reduced film thickness. In order to prevent film delamination without adding an adhesive interlayer, the film thickness of the CN_x films was further reduced to a thickness of $\approx$ 80 nm. No film delamination was observed according to tab. 4.2 for all of the prepared CN_x films. Obviously, a reduction of the film thickness to 80 nm offers one possibility to prevent film delamination.

Use of a thin adhesive interlayer in the form of an a-C film. In order to achieve a better adhesion, a thin a-C film was used as an adhesive interlayer (film thickness $\approx$ 20 nm). This type of film was used because it exhibits perfect adhesion according to tab. 4.1. The film thickness of the CN_x film was again $\approx$ 200 nm. The results given in tab. 4.2 show that in some cases delamination occurs even with the adhesive interlayer. Accordingly, further improvement was necessary.

Use of a thick adhesive a-C interlayer. Another possible solution for the delamination problem is the deposition of CN_x films on a thick a-C support. The total thickness of the resulting bilayer was 200 nm and the thickness of the a-C adhesion layer was 100 nm. The deposited bilayers exhibit perfect adhesion to the silicon substrate; no delamination was observed (tab. 4.2).

4.1.3 Concluding remarks

According to the observations described in the previous section, there are two possibilities to deposit CN_x films on conventional silicon substrates without film

description	nitrogen concentration in process gas						
	0%	5%	25%	50%	75%	100%	100%
total gas pressure [Pa]	0.8	0.8	0.8	0.8	0.8	0.8	4.0
CN_x single layer, thickness 200 nm	no	yes	yes	yes	yes	yes	no
CN_x layer, thickness 200 nm; a-C adhesive interlayer, thickness 20 nm	—	yes	yes	yes	yes	no	—
CN_x single layer, thickness 100 nm	—	no	yes	yes	yes	no	—
CN_x single layer, thickness 80 nm	—	no	no	no	no	no	—
CN_x layer, thickness 100 nm; a-C adhesive interlayer, thickness 100 nm	—	no	no	no	no	no	—

Table 4.2: List of the prepared films regarding the solution of the delamination problem. Additionally, it is given whether delamination was observed or not (yes/no). A — means that the corresponding type of the carbonaceous film was not considered.

delamination:

1. *Deposition of a sufficiently thin single layer:* For CN_x films with a film thickness of ≈ 80 nm no delamination was observed on silicon substrates.

2. *Use of a thick adhesive a-C interlayer:* Double layers a-C/CN_x, where a-C with a thickness of ≈ 100 nm serves as an adhesive interlayer, can be deposited without delamination on silicon substrates. The thickness of the CN_x top layer is ≈ 100 nm leading to a total film thickness of the double layer of ≈ 200 nm.

The use of a carbonaceous film as an interlayer between a cerium oxide film and the silicon substrate requires a sufficient film thickness of the carbonaceous interlayer in order to have enough material available to be etched away during the cerium oxide deposition in the presence of oxygen [17]. For this reason, the use of the double layers with a total thickness of 200 nm was preferred over the single layers with a thickness of only 80 nm. Nevertheless, the thin single layers are more appropriate than the double layers for investigations regrading the elemental/chemical composition of the CN_x films with bulk methods, such as HAXPES, because the a-C interlayer may influence the result of the measurement.

For the present study, carbonaceous double layers were deposited on conventional silicon substrates; these layers serve as interlayers for the cerium oxide-based films. In addition, an a-C and a CN_x film deposited in pure nitrogen at the increased process gas pressure were deposited. Table 4.3 summarizes the various types of carbonaceous films and their nomenclature used in the present work.

label	layer type	thickness of the CN_x film [nm]	concentration of nitrogen in the process gas [%]	total gas pressure [Pa]
a-C	single	200	0	0.8
CN_x-5%	double	100	5	0.8
CN_x-25%	double	100	25	0.8
CN_x-50%	double	100	50	0.8
CN_x-75%	double	100	75	0.8
CN_x-100%	double	100	100	0.8
CN_x-100%, h.p. (double)	double	100	100	4.0
CN_x-100%, h.p.	single	200	100	4.0

Table 4.3: Overview about the carbonaceous films prepared for the present work. The labels are used in the whole thesis. The total gas pressure refers to the deposition of the top layer in case of the double layers.

4.2 Investigation of the morphological properties

4.2.1 Information about the used samples

For this study, a series of a-C/CN_x double layers with a total film thickness of 200 nm was prepared on silicon substrates (tab. 4.3, p. 37). In addition to these double layers, an a-C and a CN_x-100%, h.p. single layer were deposited on silicon with a total film thickness of 200 nm in each case.

4.2.2 Morphological properties investigated with SEM and AFM

The surface morphology of the various as-prepared CN_x films was determined by means of SEM and AFM. The corresponding SEM micrographs are given in fig. 4.2; the AFM images are shown in fig 4.3. All of the investigated CN_x films exhibit a compact surface morphology; no signs of any porosity are observable with the used microscopic techniques. The surface is very flat, which is confirmed by the R_a values determined from the AFM images in case of the a-C and the CN_x-100%, h.p. film: The roughness does not exceed 2.5 nm. In comparison with the CN_x-100%, h.p. film, the a-C film is even flatter with a surface roughness $R_a = 1.5$ nm. However, a certain nanostructure is visible on the surface in some cases: whereas only signs of a slight hillock-like structure are observable for the a-C, CN_x-5%, CN_x-25% and CN_x-100%, h.p. film, it becomes slightly more pronounced for the remaining CN_x films.

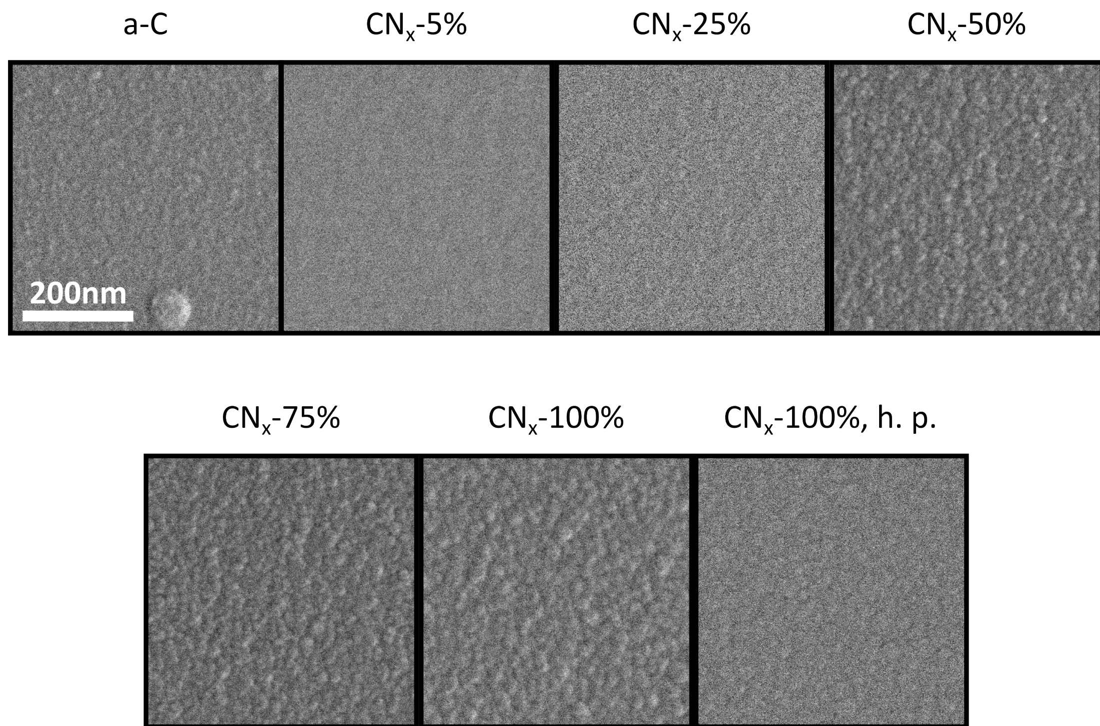

Figure 4.2: SEM micrographs of the various as-prepared CN_x films.

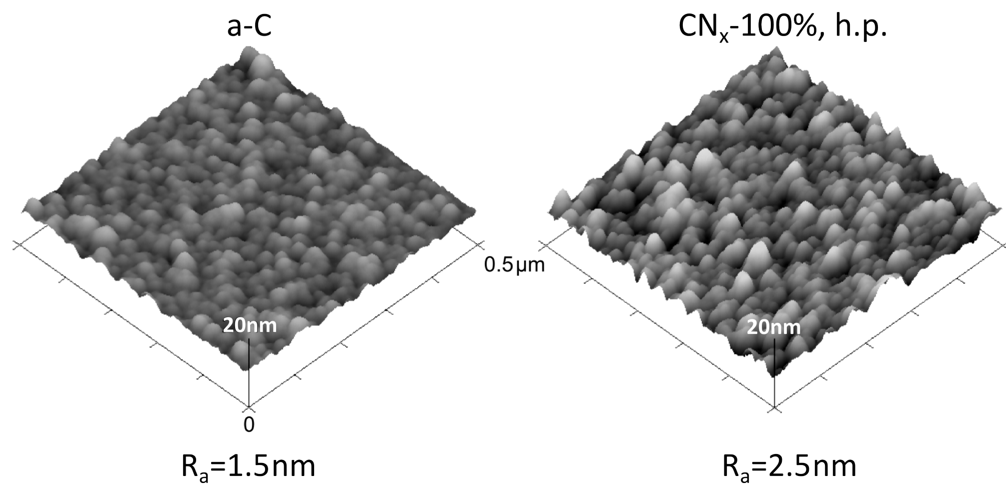

Figure 4.3: AFM images of the as-prepared a-C and CN_x-100%, h.p. film. The determined roughness values R_a are given below.

Chapter 5

Oxygen plasma treatment of the carbonaceous films

This chapter deals with the morphological modifications of the various carbonaceous materials induced by the impact of oxygen plasma. The changes of the morphology were investigated by means of various microscopic techniques, including SEM, AFM and TEM. The first part covers the carbonaceous films deposited on silicon; the second part focuses on the bulk materials graphite foil and nanoGDL.

5.1 Information about the prepared samples

A series of a-C/CN_x double layers according to tab. 4.3, p. 37 as well as the a-C and CN_x-100%, h.p. single layers (film thickness 200 nm) were prepared on silicon substrates. The as-deposited films were subsequently etched in oxygen plasma for various durations of oxygen plasma treatment at a discharge current of 2 mA. In addition to the carbonaceous films, bulk substrates in the form of the nanoGDL and the graphite foil were treated in oxygen plasma for 40 minutes.

5.2 Oxygen plasma treatment of the carbonaceous films on silicon

5.2.1 Determination of the etching rate

The etching rates were determined via step height measurements with AFM. For this purpose, the as-deposited carbonaceous films were partially masked with felt-tip prior to oxygen plasma treatment (see fig. 5.1, left). After the etching process, the mask was removed with acetone and isopropylalcohole. The duration of the etching was chosen in such a way that the maximum film thickness etched away during the etching process did not exceed 60 nm in order to exclude any influence of the a-C adhesion interlayer in case of the carbonaceous bilayers. The etching rate was normalized to the etching rate $v_{\mathrm{etch,a-C}}$ obtained for the a-C film and calculated using eq. 5.1, where h denotes the step height and t_{etch} stands for the duration of plasma treatment:

$$v_{\mathrm{etch}} = \frac{\frac{h}{t_{\mathrm{etch}}}}{v_{\mathrm{etch,a-C}}} \tag{5.1}$$

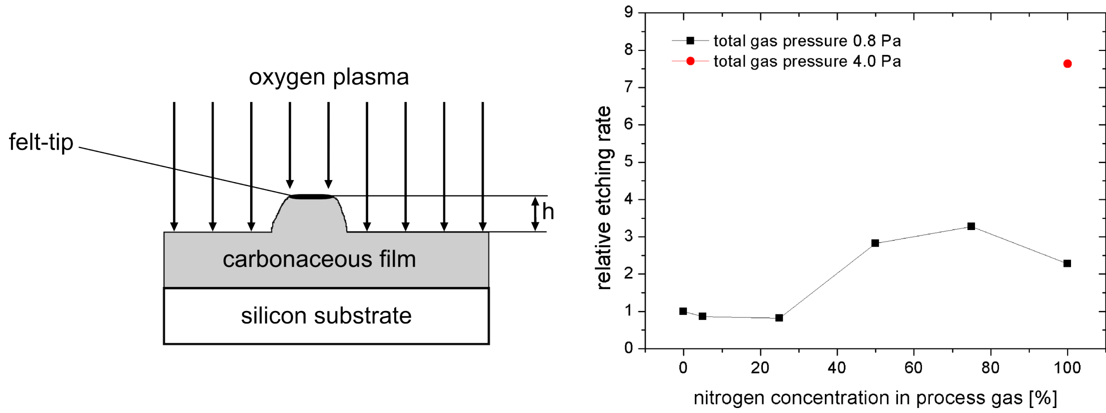

Figure 5.1: Determination of the etching rate of carbonaceous films on silicon substrates in oxygen plasma. Left: Schematic view of the sample used for the step-height measurement for the determination of the thickness of the layer etched off; right: Relative etching rate depending on the nitrogen concentration in the process gas.

The results regarding the determination of the etching rate are shown in fig. 5.1 (right). It is obvious that the relative etching rate slightly decreases for the CN_x-5% and CN_x-25% film in comparison with the a-C film. A considerable increase of the relative etching rate is observable for the CN_x-50% and CN_x-75% film; in case of the CN_x-100% film, a slight decrease of the etching rate occurs. The highest relative etching rate appears for the CN_x-100%, h.p. film.

5.2.2 Morphological modifications

Oxygen plasma treatment of the various CN_x films. The SEM micrographs of the CN_x films treated in oxygen plasma for 20 minutes are shown in fig. 5.2. The formation of a grainy surface structure can be observed in most cases, except CN_x-5% and CN_x-25%. These two films seem to remain nearly unchanged in comparison with the as-prepared films in fig. 4.2, p. 38.

Influence of the duration of oxygen plasma treatment. The influence of the duration of oxygen plasma treatment on the film morphology was investigated for the single layers a-C and CN_x-100%, h.p. by means of SEM, TEM and AFM. The corresponding SEM micrographs and TEM images as well as the AFM images and roughness values obtained for different durations of oxygen plasma treatment are shown in figs. 5.6 — 5.5.

For both types of carbonaceous films, a continual and uniform material erosion is visible in the TEM images. However, in case of the a-C film the oxygen plasma treatment does not change the surface roughness significantly within the first 30 minutes. Nevertheless, a certain nanostructurazition is visible in the SEM micrographs: The formation of a grainy surface structure can be observed. The oxygen plasma treatment for 40 minutes leads to the formation of deeper hollows compared to the untreated a-C film, which is visible in the corresponding AFM image. This results in a higher R_a value. The enhanced surface roughness even finds its expression in the TEM cross-sectional view.

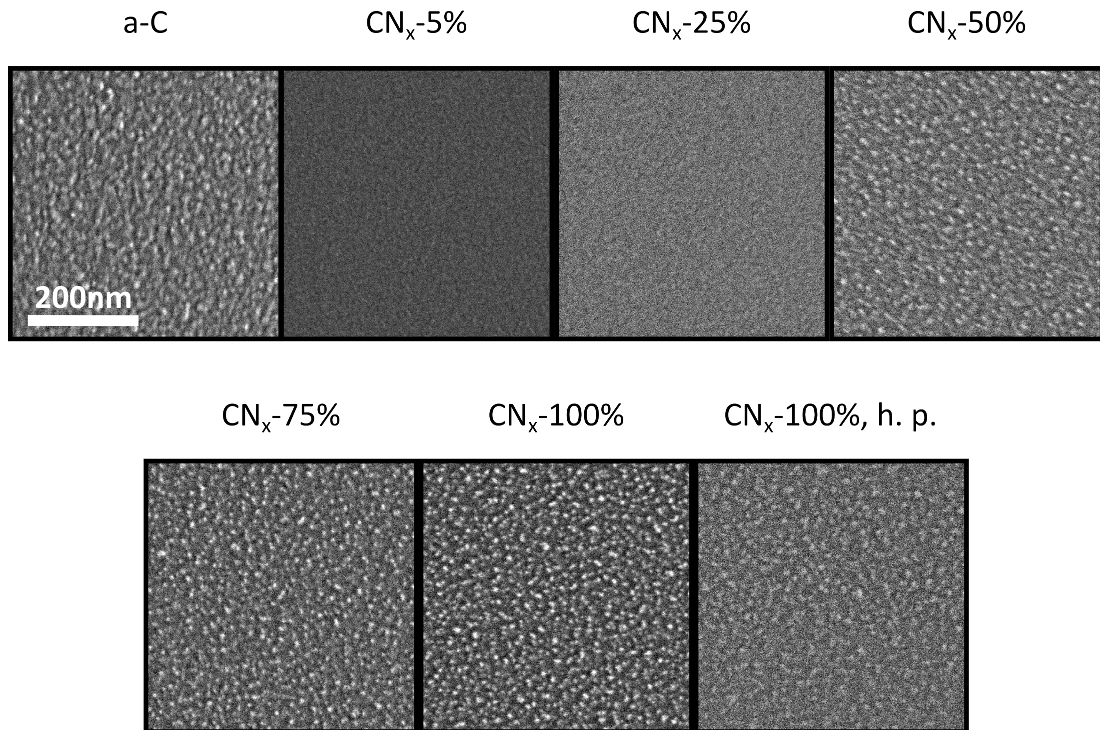

Figure 5.2: Overview about the SEM micrographs of the various CN_x films treated in oxygen plasma for 20 minutes.

In case of the CN_x-100%, h.p. film no significant change of the R_a value could be observed after 30 minutes of plasma impact, although a considerable decrease occured after 10 and 20 minutes of plasma treatment. For 40 minutes of plasma etching, a considerable flattening of the surface can be observed accompanied by an anew decrease of the R_a value. This flattening is correlated with the formation of a fine grainy structure visible in the SEM image in fig. 5.6. This effect is correlated with a nearly complete removal of the CN_x-100%, h.p. film as it can be seen in the TEM image.

5.3 Oxygen plasma treatment of the bulk substrates

The SEM micrographs of the graphite foil and the nanoGDL are shown in fig. 5.6 prior to and after 40 minutes of oxygen plasma treatment. In case of the graphite foil, AFM images were recorded in addition.

It is obvious that a nanostructurization of the surface appears as a result of oxygen plasma impact in case of all of the investigated substrates. Whereas the surface of the graphite foil is completely flat prior to the oxygen plasma treatment, the formation of a grainy surface morphology is visible after the oxygen plasma impact. The AFM image of the oxygen plasma treated graphite foil shows a considerably roughened surface in comparison with the atomically flat surface of the untreated graphite foil.

The same effect of surface modification induced by oxygen plasma impact is

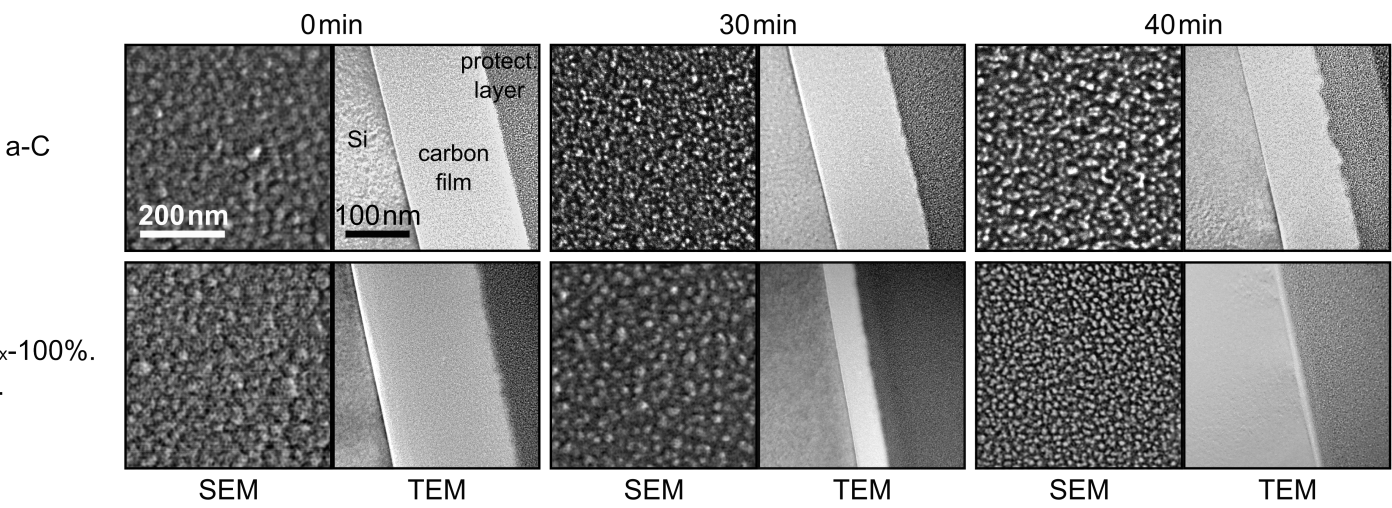

Figure 5.3: SEM micrographs amd TEM images of the oxygen plasma treated a-C and CN_x-100%, h.p. film for two different durations of plasma treatment.

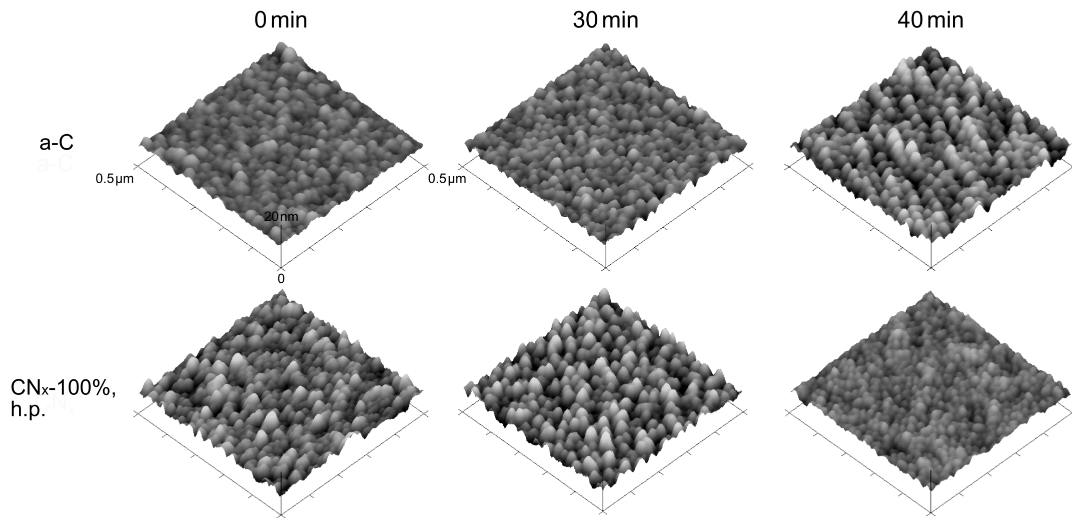

Figure 5.4: AFM images of oxygen plasma treated a-C and CN_x-100%, h.p. film for two different durations of plasma treatment.

likewise observable in case of the nanoGDL substrate. Whereas the surface of the carbon nanoparticles on the as-received nanoGDL substrate is rather flat, it appears considerably roughened after oxygen plasma impact.

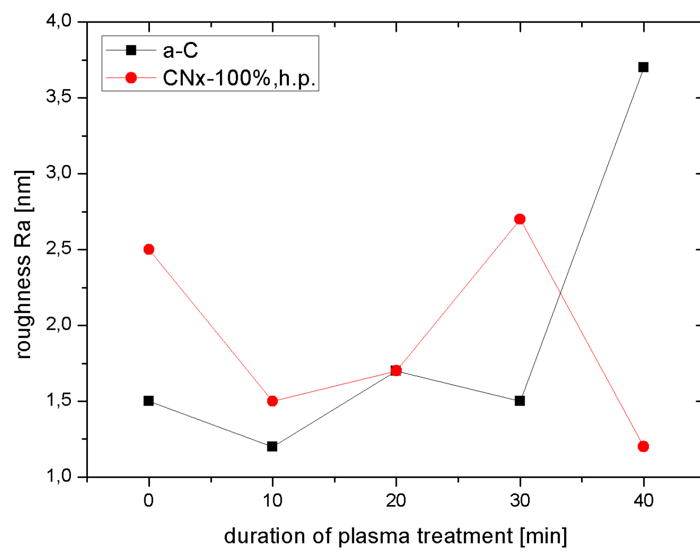

Figure 5.5: Roughnes values obtained from the AFM images for the a-C and CN_x-100%, h.p. film depending on the duration of oxygen plasma treatment.

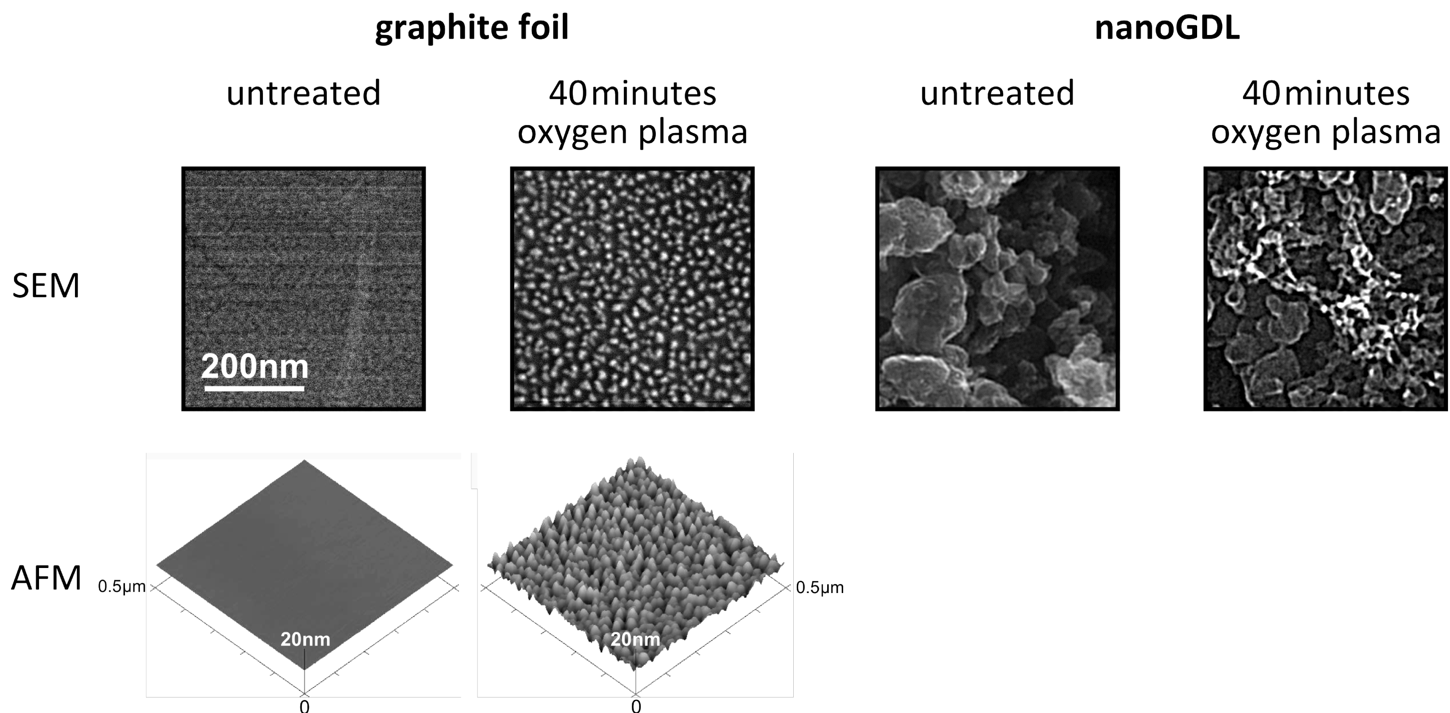

Figure 5.6: SEM micrographs of untreated and oxygen plasma treated bulk substrates, namely the graphite foil and the nanoGDL. In case of the graphite foil, the corresponding AFM images are likewise given.

Chapter 6

Morphology of cerium oxide/carbon bilayers on silicon

This chapter is focused on the investigation of the morphology of cerium oxide films with a maximum thickness of 40 nm on the various carbonaceous films supported by silicon. The influence of several parameters of the cerium oxide deposition on the cerium oxide film morphology was studied.

6.1 Deposition of cerium oxide films in argon/-oxygen gas mixtures

6.1.1 Influence of the oxygen concentration in the process gas

Determination of the cerium oxide deposition rate

The cerium oxide deposition rate was determined for various argon/oxygen gas mixtures via step-height measurements. For this purpose, conventional silicon substrates (*without* any carbonaceous film) partially masked with felt-tip were used. The mask was removed after the cerium oxide film deposition by means of acetone and isopropylalcohole. The oxygen partial pressure p_{O_2} was varied, whereas all of the other parameters of the cerium oxide deposition process were not changed including the RF discharge power ($P = 17\,\mathrm{W}$), total gas pressure ($p_{\mathrm{total}} = 0.4\,\mathrm{Pa}$) and target-to-substrate distance 90 mm. The deposition rate was determined according to eq. 6.1 via dividing the cerium oxide film thickness a with the duration of the cerium oxide deposition t_{Dep}. Subsequently, the deposition rate was normalized to the deposition rate in pure argon v_{Dep}^{Ar}; this quantity will be denoted by *relative deposition rate*:

$$v_{\mathrm{Dep}} = \frac{\frac{a}{t_{\mathrm{Dep}}}}{v_{\mathrm{Dep}}^{Ar}} \tag{6.1}$$

From fig. 6.1 it is obvious that the cerium oxide deposition rate reacts extremely sensitively to changes in the concentration of oxygen in the process gas. The addition of 1 mPa oxygen delivers a deposition rate, which is only one third

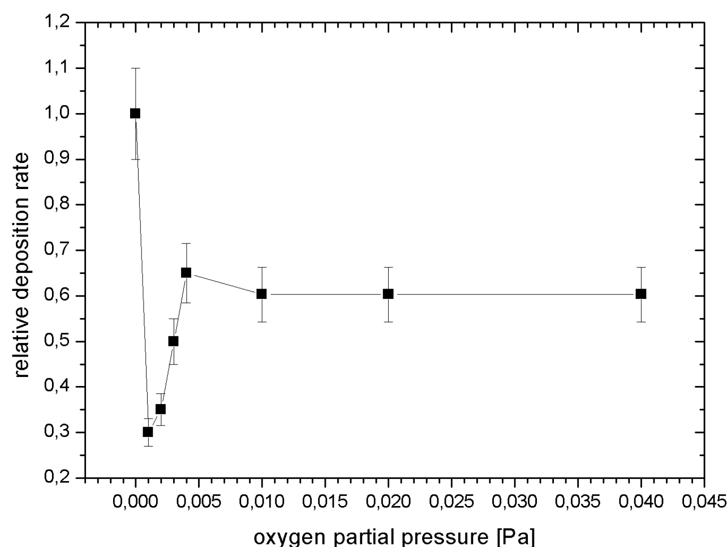

Figure 6.1: Relative deposition rate of cerium oxide depending on the oxygen partial pressure in the used process gas (total gas pressure 0.4 Pa).

of the deposition rate in pure argon. If more oxygen is added to the process gas, the cerium oxide deposition rate increases linearly with the oxygen partial pressure. For oxygen partial pressures above 4 mPa, a saturation value of the cerium oxide deposition rate is reached, which is approximately 0.6 of the deposition rate in pure argon.

Investigation of the film morphology on carbonaceous substrates

Information about the prepared samples. A series of samples with cerium oxide films with 20 nm thickness was deposited on a-C and CN_x-100%, h.p. layers (thickness $\approx$ 200 nm) on silicon substrates at various oxygen partial pressures. The RF discharge power was adjusted in order to keep the cerium oxide deposition rate constant at 0.2 nm/min for all depositions.

Film morphology. Figure 6.2 shows the SEM micrographs of the cerium oxide/a-C (CN_x-100%, h.p., respectively) bilayers deposited on silicon depending on the oxygen partial pressure used during the cerium oxide film deposition. For the cerium oxide/CN_x-100%, h.p. bilayer, the TEM cross-sectional view is additionally given.

It can be clearly seen that the bilayers deposited in pure argon are compact with a fine grainy surface morphology in case of the cerium oxide/a-C bilayer. Likewise, the cerium oxide/CN_x-100%, h.p. bilayer is nearly compact. However, the formation of holes can be observed occasionally. This observation is confirmed by the TEM image showing holes, which are etched into the CN_x-100%, h.p. film. These holes, however, do not reach down to the silicon substrate.

In contrast, the cerium oxide deposition in argon/oxygen at p_{O_2} = 0.4 mPa delivers bilayers with a porous surface morphology. The growth of islands with

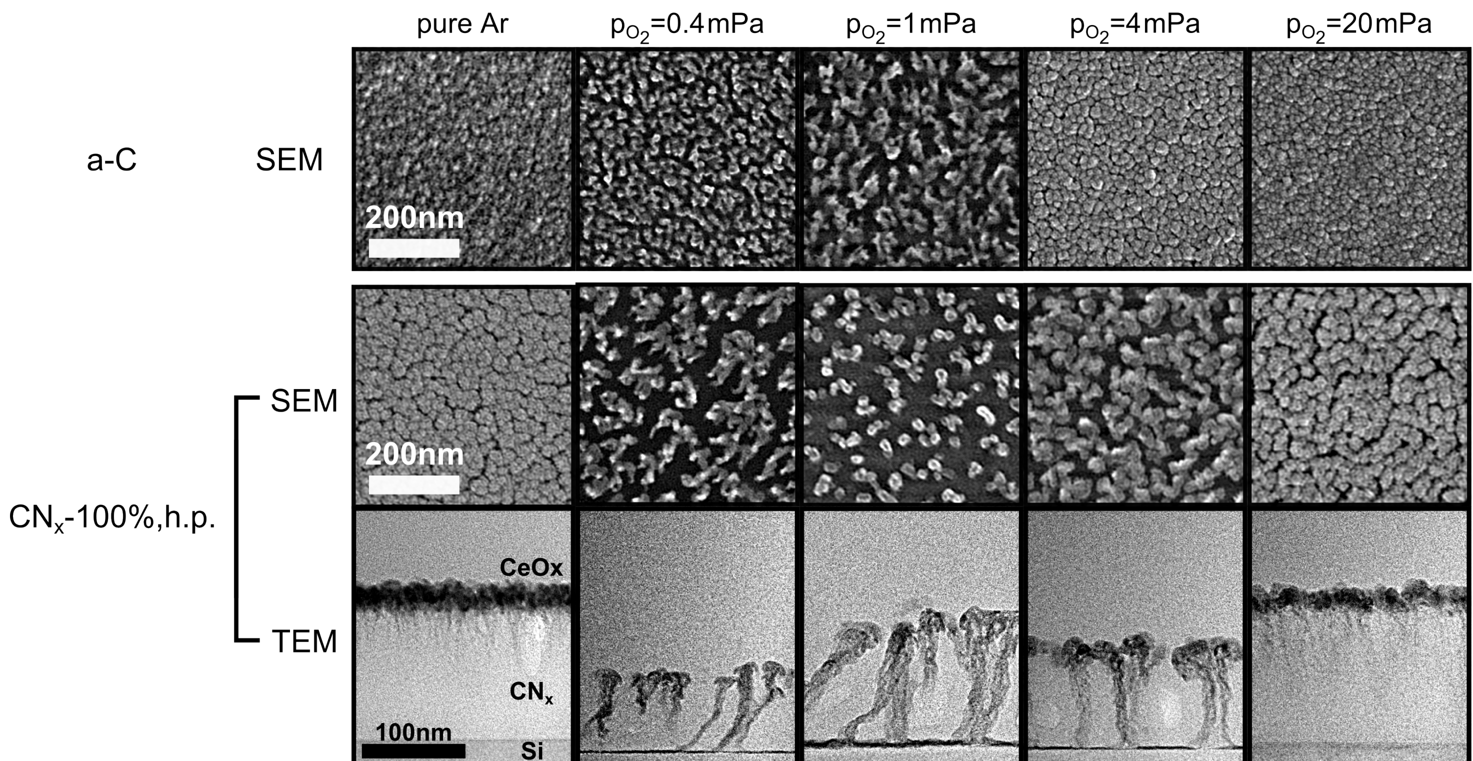

Figure 6.2: SEM micrographs of 20 nm cerium oxide films on silicon substrates with either an a-C or CN_x-100%, h.p. interlayer deposited at various oxygen partial pressures in the process gas used for the cerium oxide deposition. For selected cerium oxide/CN_x-100%, h.p. bilayers, the corresponding TEM images are additionally shown. The cerium oxide deposition rate was 0.2 nm/min in all cases.

a complicated shape separated by gaps is visible. This porous structure appears finer in case of the cerium oxide/a-C bilayer. The TEM cross-sectional view shows the formation of a noodle-like cross-sectional structure in case of the cerium oxide/CN_x-100%, h.p. bilayer. In the TEM micrograph, the noodle-like objects do not exhibit any material contrast between top and bottom parts indicating that not only the top but also the sides of these objects are covered with cerium oxide. The SEM micrograph delivers only a top-view of the noodle-like objects. The same statements are valid for the cerium oxide film deposited at $p_{O_2} = 1\,\mathrm{mPa}$. However, the SEM micrographs reveal that the holes between the islands are larger for both bilayers in comparison with the lower oxygen partial pressure.

Further increase of the oxygen partial pressure to $p_{O_2} = 4\,\mathrm{mPa}$ leads to the formation of a cerium oxide/CN_x-100%, h.p. bilayer with a tree-like cross-sectional structure visible in the TEM micrograph. The darker color of the top of the tree-like objects indicates that cerium oxide is preferentially deposited at the caps of these objects, which are partially interconnected via the cerium oxide film. In the SEM micrograph, the cerium oxide film appears more compact in comparison with the films deposited at the lower oxygen partial pressures. In case of the cerium oxide/a-C bilayer, this effect is even more pronounced with a nearly completely compact surface exhibiting almost no holes. The surface morphology shows a grainy structure.

Both bilayers prepared at $p_{O_2} = 20\,\mathrm{mPa}$ exhibit a similar surface morphology as that ones deposited in pure argon. For the cerium oxide/CN_x-100%, h.p. bilayer, the cross-sectional view confirms the formation of a nearly compact bilayer.

Discussion. The SEM micrographs and TEM images of the cerium oxide/carbon bilayers clearly show that the oxygen concentration in the process is a crucial parameter determining the morphology of the final bilayer. For oxygen partial pressures around 1 mPa, the formation of highly porous bilayers is visible; in case of the CN_x-100%, h.p. support, a noodle-like bilayer is formed. The origin of such structures can be explained with an etching process of the carbonaceous interlayer in the presence of some kind of reactive oxygen species originating from the plasma. However, oxygen partial pressures exceeding 4 mPa lead to the formation of almost compact cerium oxide/carbon bilayers comparable to cerium oxide films prepared in pure argon without any additionally introduced oxygen. Obviously, a too high oxygen concentration in the process gas suppresses the etching of the carbon support during cerium oxide deposition. Two possible explanations can be found for this behaviour:

- *Fast masking of the carbon support:* The higher concentration of oxygen in the process gas may influence the structure of the growing cerium oxide films. Likewise, the nucleation rate of cerium oxide nuclei during the first stage of cerium oxide film growth as well as their mobility might be affected by the oxygen concentration in the process gas. An oxygen concentration exceeding a certain critical value might lead to a fast masking of the carbon support and, as a consequence, suppressed etching.

- *Lower fraction of reactive oxygen species:* It is not known exactly, which kind of oxygen species is responsible for the etching of the carbon support during cerium oxide deposition. Atomic oxygen, radicals as well as oxygen

ions may be the driving force for this process. An increased oxygen concentration in the process gas may influence the composition of the plasma in such a way that a depletion of oxygen species responsible for the etching of the carbonaceous films occurs in comparison with lower oxygen concentrations. This might in turn lead to a suppressed etching of the carbon support.

It is interesting to notice that the most intense etching of the carbon support appears for $p_{O_2} = 1\,\mathrm{mPa}$. This is exactly the oxygen partial pressure which is connected with the most ineffective cerium oxide film deposition on silicon. This finds expression in the low relative deposition rate in comparison with other oxygen concentrations (fig. 6.1, p. 47).

6.1.2 Influence of the cerium oxide film thickness

Information about the used samples. A series of cerium oxide films with various film thicknesses reaching from 0.5 to 40 nm was deposited on the a-C and CN_x-100%, h.p. single layers with 200 nm thickness on silicon substrates. The cerium oxide film was deposited in argon/oxygen with $p_{O_2} = 1\,\mathrm{mPa}$ and $v_{\mathrm{Dep}} = 0.2\,\mathrm{nm/min}$. The cerium oxide film thickness was estimated from the known cerium oxide deposition rate and the duration of the cerium oxide deposition.

Morphological properties. The SEM micrographs of the prepared films are shown in fig. 6.3. In case of the a-C support, the formation of a very fine grainy surface structure is observable for cerium oxide film thicknesses below 1 nm. For higher film thicknesses, the formation of islands separated by gaps is visible. With increasing cerium oxide film thickness, the island size seems to increase accompanied by an increase of the extension of the gaps in horizontal direction. This process continues until the cerium oxide film thickness of 20 nm is reached. In case of the 40 nm cerium oxide film, a compact surface morphology with a grainy structure is observable.

In case of the CN_x-100%, h.p. support, similar statements as in case of the a-C support can be made. However, the growth of the island size proceeds considerably faster in comparison with the a-C support. Already for the 0.5 nm cerium oxide film the formation of islands separated by gaps is visible. For higher cerium oxide film thicknesses, the island size as well as the horizontal extension of the separating gaps increases. The space between the islands is significantly larger in case of the CN_x-100%, h.p. than for the a-C support. However, also for the CN_x-100%, h.p. support the cerium oxide film with 40 nm thickness exhibits a compact surface morphology.

Discussion. The SEM micrographs indicate that well-dispersed small cerium oxide islands separated by small gaps are formed during the first stage of cerium oxide film growth on carbonaceous substrates. With increasing duration of cerium oxide deposition, the size of the islands grows. Simultaneously, the space between the islands becomes larger. The increased size of the gaps is very likely the result of the proceeding etching process of the carbonaceous support. It seems that with increasing duration of the cerium oxide deposition an agglomeration of the islands occurs.

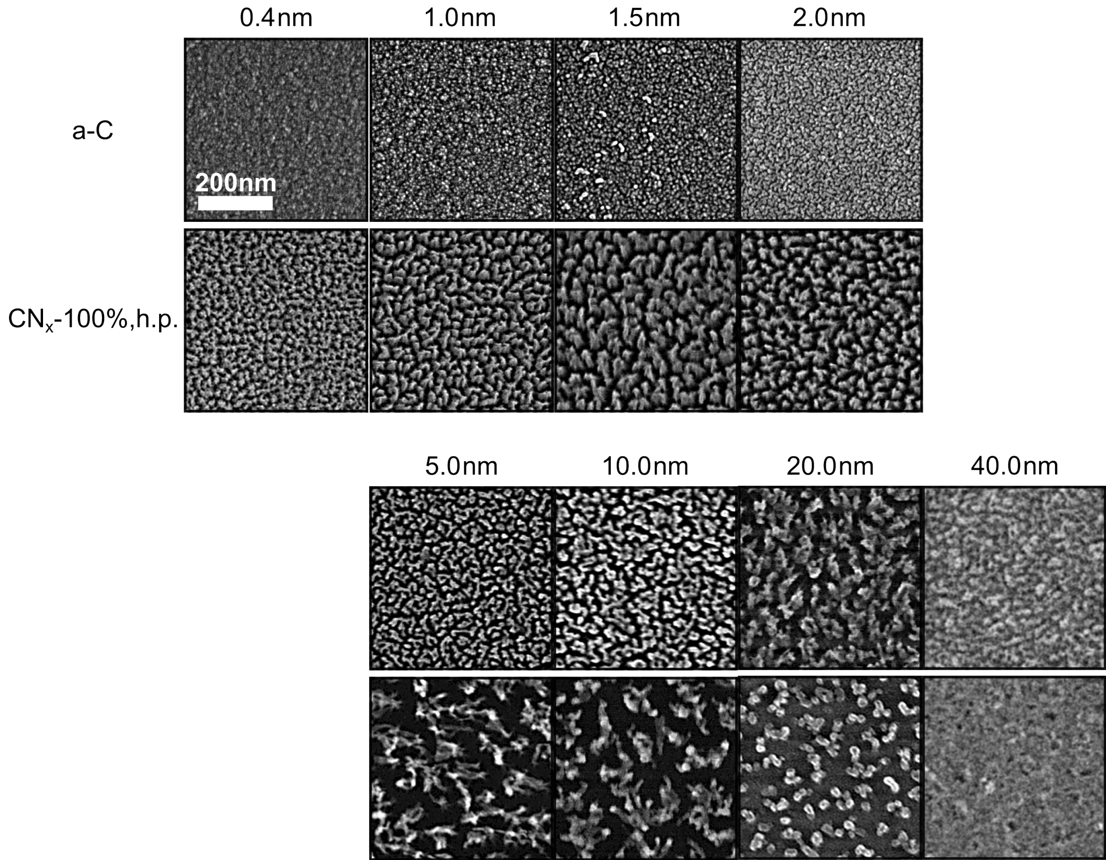

Figure 6.3: SEM micrographs of cerium oxide films deposited on silicon substrates with either the a-C or CN_x-100%, h.p. interlayer in dependence on the cerium oxide film thickness. The cerium oxide film was deposited in argon/oxygen with $p_{O_2} = 1\,\mathrm{mPa}$ at the deposition rate of 0.2 nm/min.

The faster formation of the porous bilayer structure in case of the CN_x-100%, h.p. suppport indicates that this type of carbon film is eroded faster during the cerium oxide deposition in the presence of oxygen in comparison with the a-C support. This effect can be very likely explained by means of the low oxygen plasma resistance of the CN_x-100%, h.p. film in comparison with the a-C film (fig.5.1, p. 40).

The observed formation of a compact cerium oxide film in case of the thickest film investigated in the frame of this work is in accordance with the growth model proposed by Haviar et al. [17] and can be explained with a coalescence of the cerium oxide islands.

6.1.3 Influence of the cerium oxide deposition rate

Information about the used samples. A series of cerium oxide films with 20 nm film thickness was deposited on the a-C and CN_x-100%, h.p. single layers with ≈ 200 nm thickness in each case on silicon substrates. The used process gas was argon/oxygen with $p_{O_2} = 0.4\,\mathrm{mPa}$ at the total gas pressure of 0.4 Pa. The RF discharge power was varied in order to change the cerium oxide deposition rate.

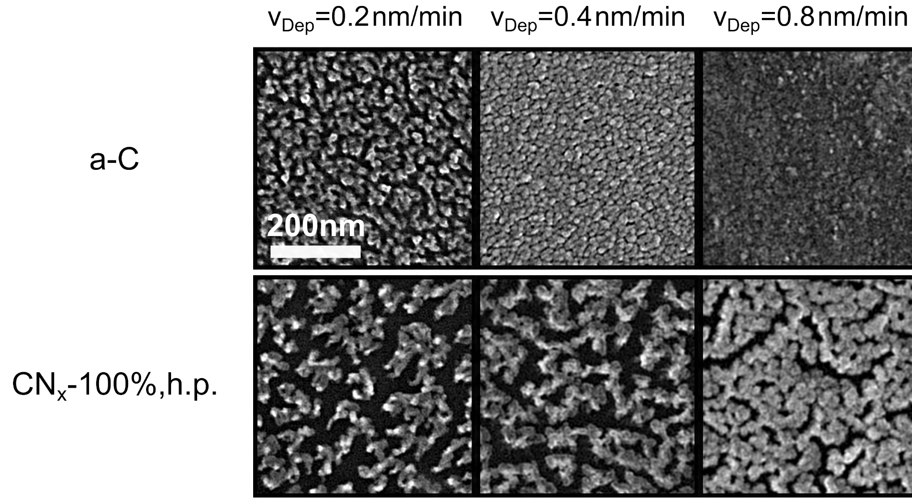

Figure 6.4: SEM micrographs of 20 nm cerium oxide films deposited on silicon substrates with either an a-C or CN_x-100%, h.p. interlayer for various cerium oxide depositon rates. The used process gas was argon/oxygen with $p_{O_2} = 0.4\,\mathrm{mPa}$.

Morphological properties. The SEM micrographs of the cerium oxide films investigated in this part of the study are shown in fig. 6.4. One can see that a more porous structure appears for 0.2 nm/min cerium oxide deposition rate. For higher deposition rates, the surface morphology of the cerium oxide/a-C bilayer becomes compact with a grainy structure. In case of the CN_x-100%, h.p. support, a porous structure appears for all of the three investigated cerium oxide deposition rates. However, with increasing deposition rate, a more compact bilayer is formed also in this case.

Discussion. The SEM micrographs clearly indicate that the cerium oxide deposition rate is another key parameter determining the morphology of the final cerium oxide/carbon bilayer. It is obvious that an increase in the cerium oxide deposition rate delivers more compact bilayers in case of the a-C as well as the CN_x-100%, h.p. film. This effect can be explained with a fast masking of the carbon support at higher cerium oxide deposition rates due to a higher particle flux in the direction of the substrate. Likewise, the higher cerium oxide deposition rate leads to shorter durations of the cerium oxide deposition. Therefore, the carbonaceous support is in contact with the plasma for a shorter time period.

6.1.4 Influence of the type of the used carbonaceous interlayer

Information about the used samples. A complete series of CN_x films was prepared in the various argon/nitrogen gas mixtures (double and single layers according to tab. 4.3, p. 37) on silicon substrates. A 10 nm cerium oxide film was deposited on these substrates in argon/oxygen with $p_{O_2} = 1\,\mathrm{mPa}$ (total pressure 0.4 Pa) and two different deposition rates, namely $v_{Dep} = 0.2\,\mathrm{nm/min}$ and 3.7 nm/min.

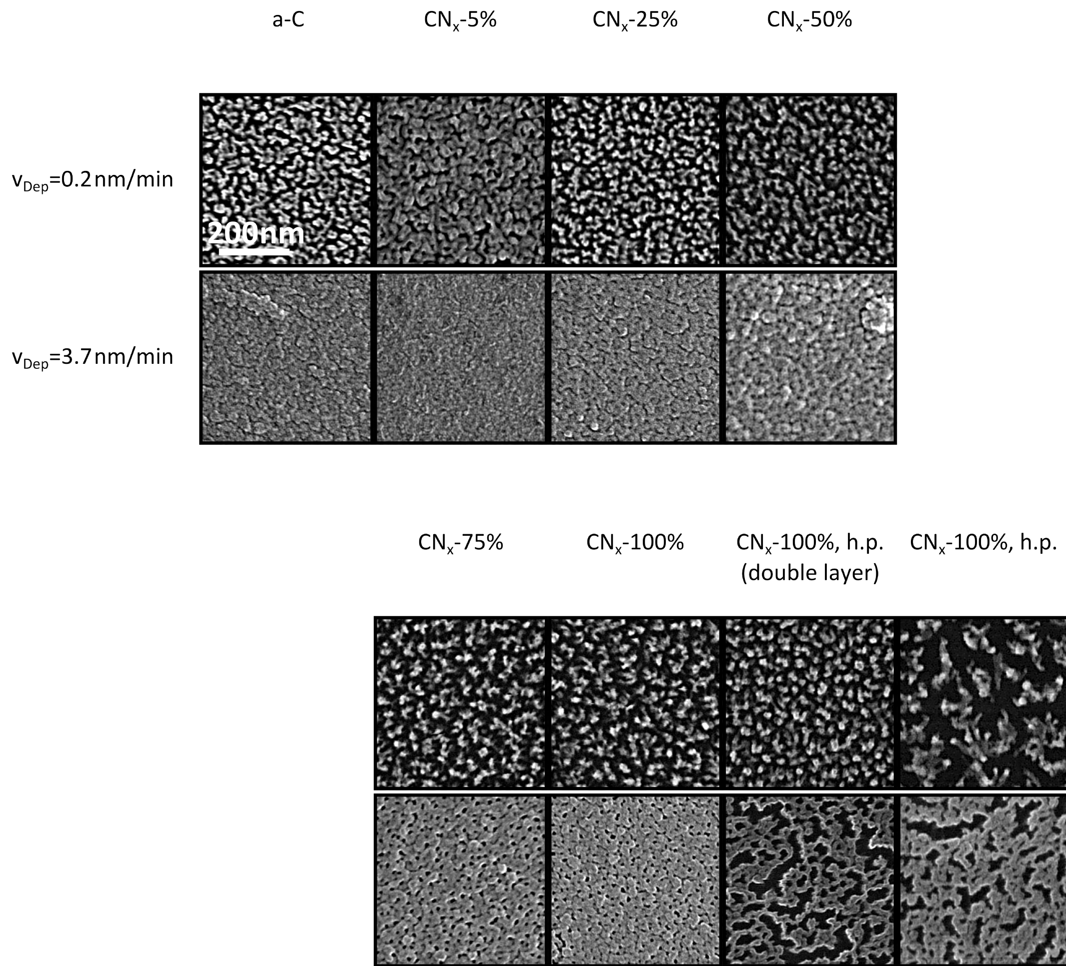

Figure 6.5: SEM micrographs of 10 nm cerium oxide films deposited on silicon substrates at $p_{O_2} = 1\,\text{mPa}$ with various carbonaceous interlayers at two different cerium oxide deposition rates.

Morphological properties. The SEM micrographs of the investigated samples are given in fig. 6.5.

- *Deposition at the high deposition rate:* A compact cerium oxide film grows on the a-C support. The surface exhibits a grainy surface structure. With increasing nitrogen concentration in the process gas used for the CN_x deposition, the formation of small holes inside the cerium oxide films is observable. The largest holes appear in case of the CN_x-100%, h.p. support (single and double layer).

- *Deposition at the low deposition rate:* The formation of a highly porous structure can be observed in case of all cerium oxide films independently on the carbon/CN_x support. The formation of small islands separated by gaps is visible. However, the cerium oxide film structure is slightly more compact in case of the a-C support. The size of the gaps between the islands increases slightly with increasing nitrogen concentration in the process gas used for the CN_x film deposition. A significantly different structure can be observed for the cerium oxide film deposited on the CN_x-100%, h.p. single

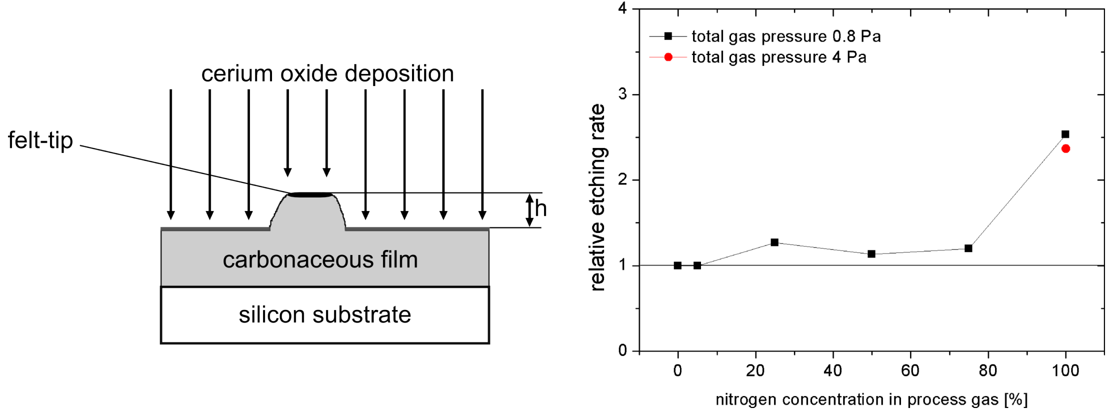

Figure 6.6: Determination of the etching rate of carbonaceous films on silicon substrates during cerium oxide deposition for the various CN_x supports. Left: schematic view of the sample used for the step-height measurement; right: relative etching rate depending on the nitrogen concentration in the process gas used for the CN_x film preparation.

layer. The formation of larger gaps between the islands compared to the other carbon supports is visible.

6.1.5 Determination of the CN_x material erosion during cerium oxide deposition

The main goal of this study was the determination of the degree of material erosion of the various CN_x films during cerium oxide deposition. For this purpose, a series of CN_x double layers as well as the a-C and CN_x-100%, h.p. single layer was prepared (tab. tab. 4.3, p. 37). Part of each as-deposited CN_x film was masked with pen prior to the cerium oxide film deposition. After the deposition of a 2 nm cerium oxide film, the mask was removed by means of acetone and isopropylalcohole. The etching rate of each CN_x film was determined from eq. 6.2 by measuring the height of the step h between the masked and unmasked areas of the sample, subsequent subtraction of the cerium oxide film thickness a_{CeOx} ($\approx$ 2 nm in this case) and division of the corrected step height with the duration of the cerium oxide film deposition t_{Dep}. Afterwards, the obtained etching rate was normalized to that one obtained for the a-C film $v^{\mathrm{CeOx}}_{\mathrm{etch,\,a-C}}$.

$$v^{\mathrm{CeOx}}_{\mathrm{etch}} = \left[\frac{h - (a_{\mathrm{CeOx}} = 2\,\mathrm{nm})}{t_{\mathrm{Dep}}}\right] / v^{\mathrm{CeOx}}_{\mathrm{etch,\,a-C}} \tag{6.2}$$

The parameters of the cerium oxide deposition were: $p_{O_2} = 1\,\mathrm{mPa}$ at the total-pressure of 0.4 Pa; $v_{\mathrm{Dep}} = 0.2\,\mathrm{nm/min}$.

The relative etching rate of the various CN_x supports is shown in fig. 6.6. For the CN_x-5% film, the etching rate is comparable to that one obtained for the a-C film. The etching rates determined for the CN_x-25%, CN_x-50% and CN_x-75% films are nearly equal and slightly higher in comparison with the a-C film. A considerable increase of the etching rate can be observed for both films deposited in pure nitrogen.

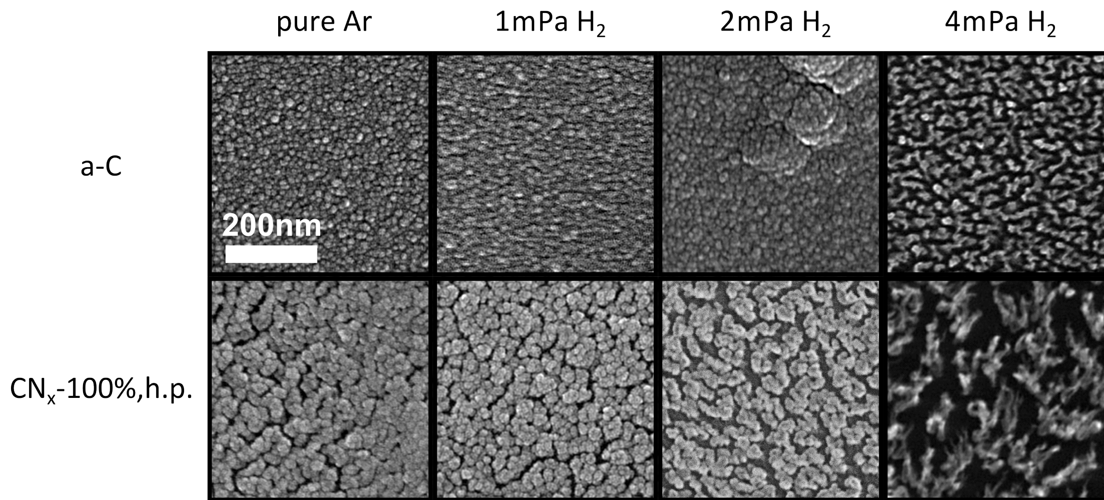

Figure 6.7: SEM micrographs of cerium oxide films with 10 nm thickness deposited in various argon/hydrogen gas mixtures. The cerium oxide deposition rate was ≈ 0.2 nm/min.

6.2 Deposition of cerium oxide films in mixtures argon/hydrogen

Information about the used samples. A series of cerium oxide films with 10 nm thickness was deposited on a-C and CN_x-100%, h.p. single layers (thickness 200 nm) on silicon substrates. The hydrogen partial pressure was varied keeping the total pressure at 0.4 Pa. The RF power was adjusted in such a way that the cerium oxide deposition rate was ≈ 0.2 nm/min.

Morphological properties. The SEM micrographs of the cerium oxide films are given in fig. 6.7. It is evident that a highly porous structure appears for $p_{H_2} = 4$ mPa. For lower hydrogen partial pressures, the cerium oxide/carbon bilayers exhibit a more compact structure.

Discussion. The obtained result shows that porous cerium oxide/carbon bilayers can be prepared in the presence hydrogen in the process gas instead of oxygen. It is very likely that hydrogen reacts chemically with the carbon support. As a result, gaseous products such as CH_x or NH_x are formed. However, in comparison with oxygen (fig. 6.2, p. 48) a higher partial pressure of hydrogen is required in order to achieve a similar etching effect as in case of oxygen.

6.3 Deposition of cerium oxide films in mixtures argon/water vapour

Information about the used samples. A series of cerium oxide films with 20 nm film thickness was deposited on silicon substrates with either the a-C or a CN_x-100%, h.p. single interlayer with 200 nm thickness. The used process

gas were argon/water vapour mixtures with various H_2O partial pressures keeping the total pressure at 0.4 Pa. The cerium oxide deposition rate was again ≈ 0.2 nm/min.

Morphological properties. The SEM micrographs of the prepared cerium oxide films are shown in fig. 6.8; the cross-sectional TEM images of the cerium oxide/CN_x bilayers are given additionally. The deposition of the cerium oxide film in pure argon delivers bilayers with a nearly compact surface morphology with a grainy structure as in the former cases; the TEM image shows a nearly compact cerium oxide/CN_x bilayer. The addition of 1 mPa of water vapour leads to the formation of a highly porous cerium oxide/CN_x-100%, h.p. bilayer with islands separated by gaps. The TEM image reveals that most of the CN_x film vanished during the cerium oxide deposition indicating the occurence of an intense etching process. In contrast, the cerium oxide/a-C bilayer is still compact with a grainy surface structure. The bilayers deposited at $p_{H_2O} = 2$ mPa and $p_{H_2O} = 4$ mPa, respectively, look very similar to each other on both substrates. A highly porous structure is visible in case of the a-C support with rather large gaps between island-like objects. In case of the CN_x-100%, h.p supported cerium oxide film, the growth of quite small islands separated by large gaps is observable comparable to the result obtained for the cerium oxide film deposited in argon/oxygen with $p_{O_2} = 1$ mPa. The TEM images clearly show that most of the CN_x film was etched away during the cerium oxide film deposition; only small piles remained. As a consequence, most of the cerium oxide covers the silicon surface.

Further increase of the partial pressure of water vapour leads to a cerium oxide/a-C bilayer with a compact surface morphology. Likewise, the cerium oxide/CN_x-100%, h.p. bilayer exhibits a more compact surface morphology in comparison with the previously described bilayers prepared at lower p_{H_2O}. The TEM image shows less material erosion in comparison with the previously described bilayers. The cerium oxide/CN_x, h.p. bilayer exhibits a more columnar-like structure.

Discussion. The results clearly show that also the addition of water vapour during cerium oxide film growth leads to the formation of porous cerium oxide/carbon bilayers. It is very likely that water molecules are decomposed in the plasma into oxygen, hydrogen and, possibly, OH groups. These species may react chemically with the carbonaceous support and form gaseous products. Similarly as in case of hydrogen, the partial pressure leading to the most intense etching of the carbonaceous support is shifted to higher values for the water vapour in comparison with oxygen (fig. 6.2, p. 48).

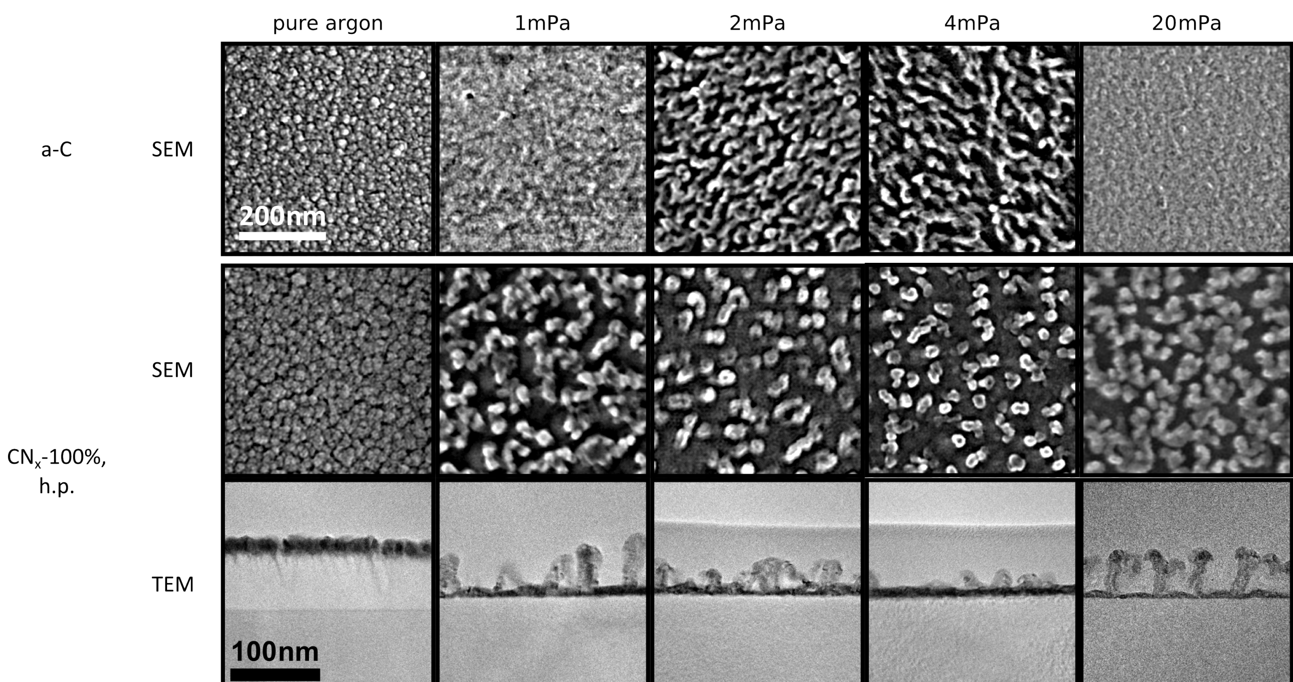

Figure 6.8: SEM micrographs of 20 nm cerium oxide films deposited on silicon substrates with either the a-C or CN_x-100%, h.p. interlayer in gas mixtures argon/water vapour with various partial pressures p_{H_2O}. For the cerium oxide/CN_x-100%, h.p. bilayers, the corresponding TEM images are additionally shown. The cerium oxide deposition rate was 0.2 nm/min.

Chapter 7

Preparation and morphology of platinum-doped cerium oxide films on various substrates

Cerium oxide films doped with platinum are promissing catalysts e. g. for fuel cell applications (sec. 1.1). For this reason, this chapter deals with the question to what extend the doping of the cerium oxide film with platinum influences the formation of the porous bilayers investigated in detail in chap. 6. The first part of the chapter is mainly focused on the preparation of CeO_x-Pt films on the carbonaceous films supported by silicon, whereas the second part covers the preparation of these films on a substrate with practical relevance for fuel cell applications, namely *nanoGDL*.

7.1 Information about the prepared samples

For this study, cerium oxide films doped with different amounts of platinum were prepared on various substrates. The CeO_x-Pt film thickness was 20 nm in all cases. The deposition conditions were chosen in such a way that porous cerium oxide film growth is enabled according to chap 6. In particular, this means: $p_{O_2} = 1\,\mathrm{mPa}$; $v_{Dep} = 0.2\,\mathrm{nm/min}$. The final film thickness was controlled by means of step height measurements on partially masked silicon substrates.

For the first part of the study, single layers of a-C and CN_x-100%, h.p. (thickness 200 nm) as well as the CN_x-50% double layers on silicon were used as substrates. The graphite foil and bare silicon were used as reference substrates. In the second part of the study nanoGDL substrates were used. The CeO_x-Pt film was deposited either directly on the nanoGDL substrate or with the use of interlayers CN_x-100%, h.p. (single layers, 200 nm) or CN_x-50% (double layers).

number of Pt wires	Pt concentration [%]
1	6
2	16
3	28

Table 7.1: Summary of the Pt concentrations depending on the number of the used Pt wires determined with XPS.

7.2 Deposition of CeO_x-Pt films on silicon

7.2.1 Determination of the platinum concentration by means of XPS

The calculated platinum concentration in the prepared CeO_x-Pt films was determined by means of XPS. For this purpose, the spectra Ce 3d and Pt 4f of the films deposited on silicon were considered. The platinum concentration was calculated using the following equation, where I means the peak area and S the sensitivity factor [1]:

$$C_{\mathrm{Pt}} = \frac{I_{\mathrm{Pt}}/(S_{\mathrm{Pt}} = 5.575)}{I_{\mathrm{Ce}}/(S_{\mathrm{Ce}} = 8.808)} \tag{7.1}$$

The platinum concentration depending on the number of the used platinum wires is given in tab. 7.1. As expected the platinum concentration in the deposited films increases with increasing number of the used platinum wires.

7.2.2 Morphological investigations

The SEM micrographs of the undoped as well as of the Pt-doped cerium oxide films with the three different platinum concentrations are shown in fig. 7.1.

The morphology of the four different cerium oxide-based films does not change considerably for the same type of substrate in most cases. A porous structure is visible for the carbonaceous films and bulk carbon substrate, whereas a compact film grows on the bare silicon substrate. Regarding the influence of platinum-doping, the cerium oxide films with the highest platinum concentration exhibit a more porous morphology on the carbonaceous substrates in comparison with the three other cerium oxide-based films. This result might indicate that a high concentration of platinum supports the growth of porous cerium oxide-based films on carbonaceous substrates. However, it cannot be excluded that this effect is caused by the uncertainty regarding the adjustment of the oxygen partial pressure, which can be guaranteed only in the range of ±10% and might lead to slight differences regarding the etching of the carbonaceous substrate.

[1] The values for the sensitivity factors have been taken from: Chastain, J.; *Handbook of X-ray Photoelectron Spectroscopy*; Perkin-Elmer Corporation, Physical Electronics Division (1992)

7.3 Deposition of CeO_x-Pt films on nanoGDL

The SEM micrographs of two different CeO_x-Pt films on the bare nanoGDL, the nanoGDL with the CN_x-100%, h.p. single interlayer or CN_x-50% double interlayer, respectively, are shown in fig. 7.2.

It is obvious that the as-received nanoGDL consists of carbon nanoparticles with a rather flat surface. Likewise, the CeO_x-Pt films deposited on the bare nanoGDL are quite smooth. In contrast, the CeO_x-Pt films deposited on the nanoGDL covered with the carbonaceous films show a highly porous surface morphology for both types of carbonaceous interlayers. However, whereas the platinum concentration does not influence the surface morphology considerably, certain morphological differences are observable between the two types of carbonaceous interlayers. In case of the CN_x-100%, h.p. interlayer, a nearly complete removal of the cabonaceous film is observable, which finds expression in a significant reduction of the size of the carbon nanoparticles. Only noodle-like objects, very likely consisting of cerium oxide and residuals of the CN_x-100%, h.p. film, can be observed.

In case of the nanoGDL substrate covered with the CN_x-50% double layer, the material erosion during the cerium oxide deposition is considerably smaller; the reduction of the size of the carbon nanoparticles is less pronounced as in case of the CN_x-100%, h.p. interlayer. The morphology can be described as a broccoli-like one.

The observed morphological differences between the cerium oxide-based films deposited on the nanoGDL substrates can be very likely explained by means of the type of the used carbonaceous interlayer. According to fig. 6.6, p. 54, the CN_x-100%, h.p. film exhibits a low etching resistance during cerium oxide deposition at the presence of oxygen leading to a high degree of material erosion. In contrast, the CN_x-50% film is etched with a lower etching rate. In addition, the used a-C interlayer very likely serves as an additional etching barrier.

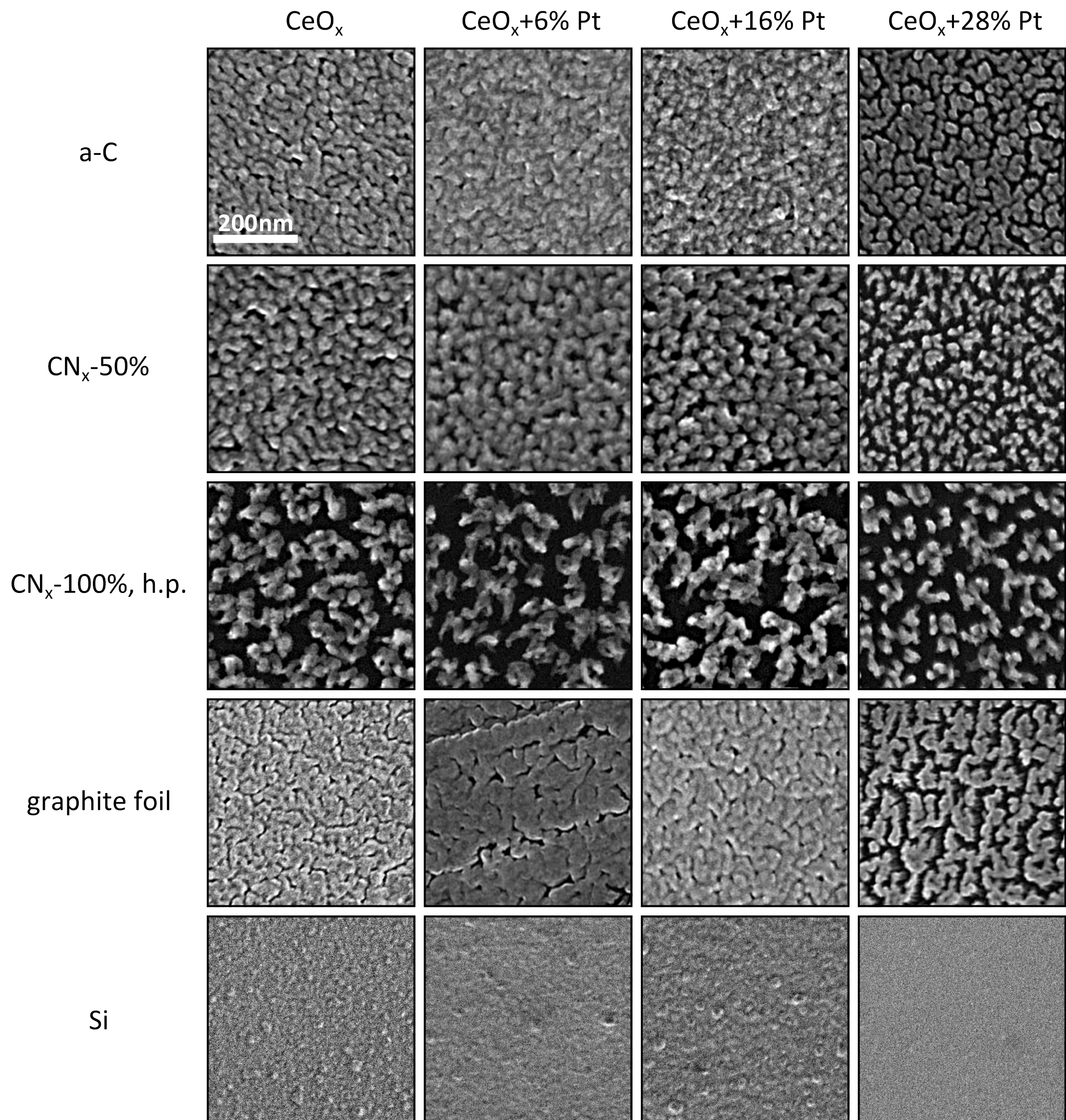

Figure 7.1: SEM micrographs of 20 nm thick cerium oxide films doped with three different concentrations of platinum on various substrates. The micrographs corresponding to undoped cerium oxide are given for comparison. All films were deposited at 1 mPa oxygen partial pressure in the process gas and 0.2 nm/min deposition rate.

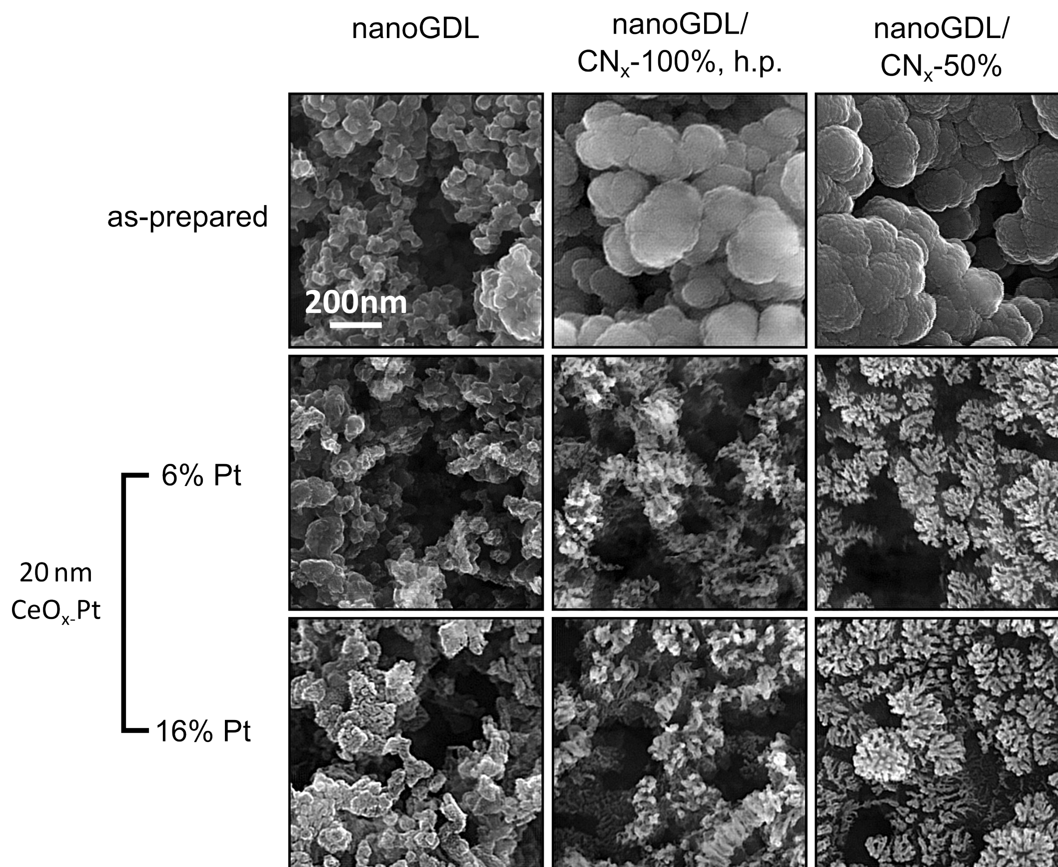

Figure 7.2: SEM micrographs of 20 nm cerium oxide films doped with two different concentrations of platinum on nanoGDL substrates (bare nanoGDL, nanoGDL with 200 nm CN_x-50% (double layer) or 200 nm CN_x-100%, h.p. (single layer), respectively). The cerium oxide films were deposited in argon/oxygen with $p =$ 1 mPa; the deposition rate was 0.2 nm/min.

Part IV

Elemental and chemical composition of the carbonaceous films

Chapter 8

Determination of the element composition of the carbonaceous films on silicon

This chapter focuses on the determination of the element composition of the as-prepared, oxygen plasma treated and cerium oxide covered carbonaceous films on silicon with various techniques. The first part of the chapter deals with the nitrogen concentration in the as-prepared carbonaceous films, whereas the second part is focused on the oxygen concentration at the surface of the carbonaceous films determined by means of the surface-sensitive technique XPS.

8.1 Composition of the as-prepared films

8.1.1 Information about the used methods and samples

The nitrogen concentration in the carbonaceous films was determined by means of XPS, EELS and EDX. The following series of samples were used:

- *XPS:* The surface sensitivity of the XPS technique allowed the use of CN_x/a-C double layers without any distortion of the result originating from the a-C interlayer. In addition to these double layers, single layers a-C and CN_x-100%, h.p. with a film thickness of 200 nm were used for this measurement (see tab. 4.3, p. 37). The substrate was silicon.

- *EELS:* The EELS analysis was performed in the TEM on lamellas cut from carbonaceous single layers with a film thickness of $\approx$ 80 nm prepared on silicon substrates.

- *EDX:* Due to the large information depth of EDX (several hundreds of nanometers), the use of the carbonaceous double layers was not possible. Likewise, the use of the single layers with 80 nm thickness on silicon was connected with problems due to a strong signal originating from the silicon substrate leading to difficulties with the correct interpretation of the EDX spectra. For this reason, 0.5 μm thick carbonaceous single layers were deposited on *graphite foil substrates covered with a 5 nm platinum film*, which was possible without any delamination of the carbonaceous film at these

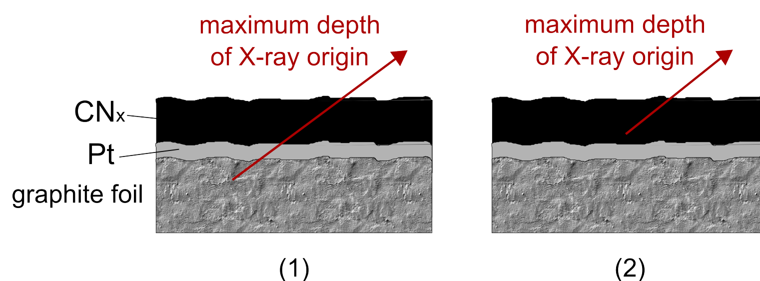

Figure 8.1: Schematic view of the EDX measurement on the CN_x films deposited on the graphite foil with a Pt interlayer. The first situation (1) is valid when Pt peaks are visible in the EDX spectrum. In case (2) the EDX signal originates only from the CN_x film and Pt is not visible in the spectrum.

conditions. The platinum interlayer served as an indicator for whether the EDX signal originates exclusively from the carbonaceous film or not according to this legend (see also fig. 8.1):

- *Platinum peaks visible in the EDX spectrum:* The X-rays are not only originating from the carbonaceous film, but may also come from the substrate making a reliable quantification of the nitrogen concentration difficult.
- *Platinum peaks not visible in the EDX spectrum:* The X-rays originate only from the carbonaceous film making a reliable determination of the nitrogen concentration possible.

The energy of the incident electrons was 3 keV, which is sufficient for the excitation of X-rays from carbon, nitrogen and platinum and simultaneously low enough to limit the information depth of EDX. At these conditions, no platinum peak was detected for all of the investigated samples. As an example, the EDX spectra for the CN_x-50% film at two different primary electron energies are shown in fig. 8.2.

8.1.2 Determination of the nitrogen concentration

The nitrogen concentration in the various CN_x films derived on the basis of the results obtained from the three methods is shown in fig. 8.3.

EDX analysis. The nitrogen concentration in the CN_x film increases continuously with increasing nitrogen concentration in the process gas. The highest nitrogen concentration appears in case of the CN_x-100%, h.p. film with $C_N^{EDX} \approx 44\%$.

XPS analysis. One can see that the nitrogen concentration increases rapidly with increasing concentration of nitrogen in the process gas used for the film deposition. For nitrogen concentrations in the process gas of 25% and higher the nitrogen concentration in the prepared films reaches its saturation value at approximately 30%. The CN_x-100%, h.p. film deposited at the higher process gas pressure again exhibits the highest nitrogen concentration, which is slightly below 40%.

EELS analysis. In agreement with the previous two methods, a considerable increase of the nitrogen concentration to 16% is detectable for the CN_x-5% film in comparison with the a-C film. For the CN_x-25% film, a decrease to 11% can be observed, which is not confirmed with XPS and EDX. For all of the remaining CN_x films, the nitrogen concentration fluctuates around 30%.

8.1.3 Discussion

In general, a relatively good agreement can be observed between the three methods. A considerable increase of the nitrogen concentration in the film is observable for nitrogen concentrations in the process gas below 25%. For higher nitrogen concentrations in the process gas, a slight gradual increase of the nitrogen concentration in the film is visible (EDX) or the nitrogen concentration remains more or less constant (XPS, EELS). The highest nitrogen concentration in the CN_x films could be achieved for the film deposited in pure nitrogen at the high process gas pressure according to the three methods. The differences between the results obtained by EDX and XPS can be very likely explained with the considerably different information depth of the methods: whereas XPS delivers information from the surface region of the film (information depth $\approx 5\,\text{nm}$), EDX is a bulk method delivering information from the whole film. For this reason, the EDX results can be considered as more reliable, because the XPS results may be affected by surface effects, e. g. surface contaminations. In case of the EELS analysis, influences on the element composition induced by the lamella preparation cannot be excluded. Czigany et al. investigated the influence of the bombardment of magnetron sputtered CN_x films with Ar-ions with energies in the keV-range on the structural properties of these films [59]. In the frame of this work, a decrease of the nitrogen concentration with respect to carbon was observed.

Correlations between the nitrogen concentration and the etching behaviour of the various CN_x films during oxygen plasma treatment/cerium oxide deposition. The evolution of the nitrogen concentration in the various CN_x films exhibits a rather good agreement with the evolution of the etching rate of these films during cerium oxide deposition in the presence of oxygen (fig. 6.6, p. 54). The two films deposited in pure nitrogen containing the highest amount of nitrogen according to EDX likewise show the highest etching rate during cerium oxide deposition. In contrast, the CN_x-5% film exhibiting the lowest amount of incorporated nitrogen shows the highest resistance against material erosion during the cerium oxide deposition of all investigated CN_x films. The CN_x films with medium nitrogen concentrations exhibit an etching rate lying between that ones obtained for the previously discussed films.

However, these statements cannot be taken over to the oxygen plasma treated films (fig. 5.1, p. 40). In this case, the CN_x-25% film exhibits a similar etching rate as the CN_x-5% film, although the nitrogen concentration is considerably different. Likewise, the two CN_x films prepared in 100% nitrogen exhibit considerably different etching rates in oxygen plasma, although the nitrogen concentration is nearly equal according to EDX and EELS. It is likely, that structural differences between the various CN_x films play a more important role for the oxygen plasma treatment than the nitrogen concentration in the film.

The obtained result indicates that the etching mechanisms taking place during oxygen plasma treatment and cerium oxide deposition in the presence of oxygen are not exactly the same in case of the CN_x films.

8.2 Composition of the oxygen plasma treated and cerium oxide covered carbonaceous films

8.2.1 Information about the used samples

This part of the study was carried out on the double layers CN_x-5% and CN_x-50% as well as the a-C and CN_x-100%, h.p. single layers with 200 nm thickness according to tab. 4.3, p. 37 with the use of silicon substrates. The films were either treated in oxygen plasma for 10 minutes or covered with a cerium oxide film with 2 nm thickness. The process gas used for the cerium oxide deposition was argon/oxygen with the total as pressure $p_{Ar+O_2} = 0.4\,Pa$ and the oxygen partial $p_{O_2} = 1\,mPa$; the deposition rate was 0.2 nm/min.

8.2.2 Determination of the nitrogen concentration in the CN_x films

The nitrogen concentrations in the CN_x-5% and CN_x-50% double layers as well as the CN_x-100%, h.p. single layer determined by means of XPS are shown in fig. 8.4 after oxygen plasma treatment and cerium oxide deposition, respectively. The oxygen plasma treated films exhibit a slightly lower nitrogen concentration in comparison with the corresponding as-prepared films. However, this decrease is very small and could be likely explained within the uncertainty of measurement.

In contrast, the nitrogen concentration of the CN_x films covered with the thin cerium oxide film decreases considerably in comparison with the corresponding as-prepared films. For all of the investigated films a decrease below $\approx 50\%$ of the initial nitrogen concentration in the corresponding as-prepared film was detected.

Discussion. The removal of nitrogen via chemical etching with oxygen is the most likely explanation for the observed nitrogen depletion in the cerium oxide covered carbonaceous films. In this regard it is very likely that the cerium oxide acts as a catalyst for the reaction between oxygen and nitrogen leading to the intense removal of nitrogen. This could also explain why the films with the highest nitrogen concentration (CN_x-100% and CN_x-100%, h.p.) exhibit the highest material erosion during the cerium oxide deposition. Cerium oxide is nowadays used as a catalyst in automobiles for the treatment of toxic exhaust gases [60]. One important reaction is the transformation of NO into N_2. This is one possible reaction, which could take place on the surface of the CN_x films during cerium oxide deposition in the presence of oxygen.

8.2.3 Determination of the oxygen concentration

Figure 8.5 shows exemplarily the survey spectra of the as-prepared and oxygen plasma treated CN_x-100%, h.p. film. Beside carbon and nitrogen, a consider-

able portion of oxygen was detected in case of the as-prepared and the oxygen plasma treated film. The oxygen contamination very likely originates from water adsorbed on the surface of the carbonaceous film; besides, oxygen may be chemically bound to carbon or nitrogen, respectively. In this regard, it has to be noted that the XPS analysis was carried out ex-situ for all of the studied carbonaceous films. In addition, a small contribution identified with aluminium was detected for the oxygen plasma treated film. This contamination with aluminium is in the range of 1 — 2% for all of the investigated oxygen plasma treated carbonaceous films. It originates very likely from the etching device, which is slightly sputtered during the etching process.

The oxygen concentration prior to and after 10 minutes of oxygen plasma treatment is shown in fig. 8.6. It is evident that the oxygen concentration is approximately 10% in case of the as-prepared films. The lowest oxygen contamination can be found for the CN_x-5% film. After oxygen plasma treatment, the oxygen concentration increases considerably for all of the investigated films reaching up to 20%. This indicates that oxygen interacts chemically with the surface of the carbonaceous films during the oxygen plasma treatment and is bound to the surface. Also for the plasma treated samples, the lowest oxygen concentration was determined for the CN_x-5% film.

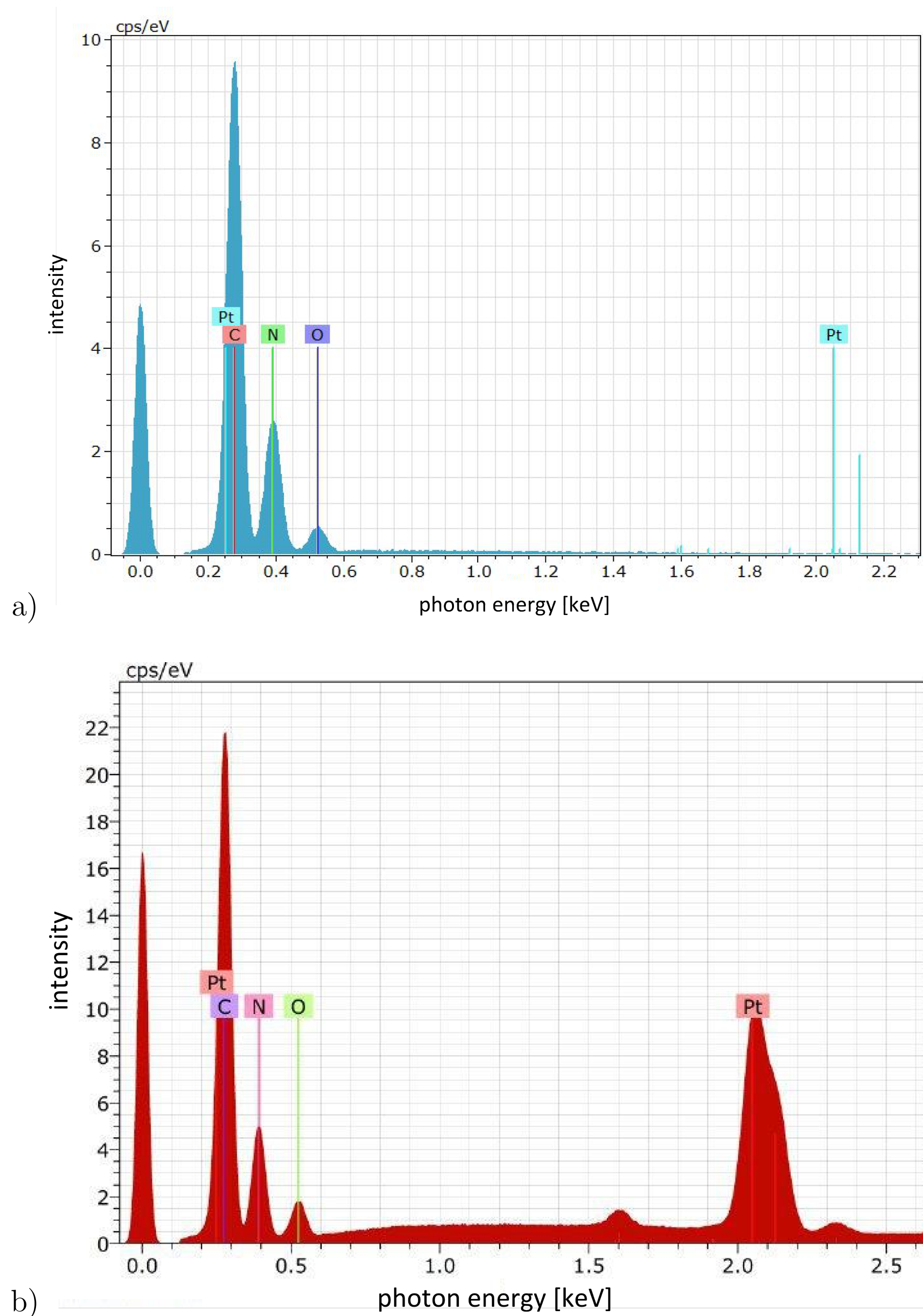

Figure 8.2: EDX spectra of the CN_x-50% film deposited on the graphite foil with a 50 nm platinum interlayer for two different primary electron energies: a) Electron energy 3 keV — no platinum peaks are visible in the spectrum indicating that the signal originates exclusively from the CN_x film; b) Electron energy 10 keV — a strong platinum peak is visible indicating that part of the EDX signal originates from areas below the CN_x film.

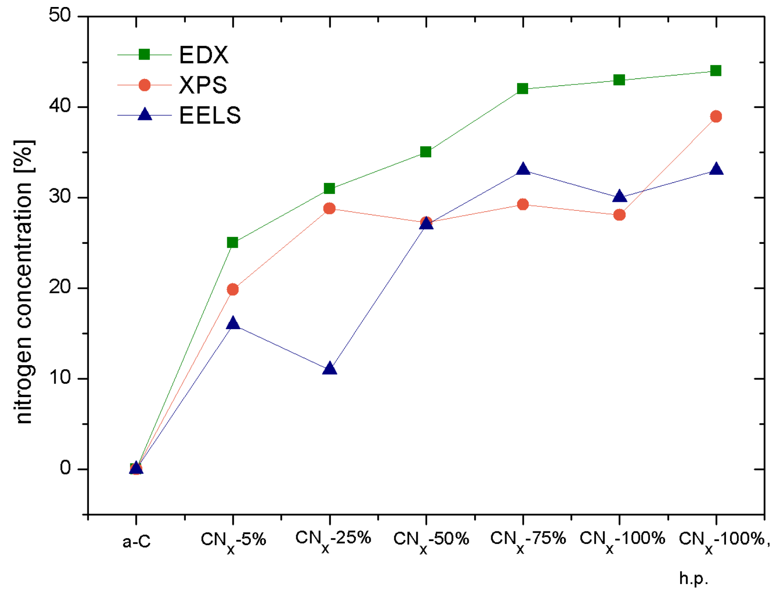

Figure 8.3: Nitrogen concentration in the CN_x films depending on the nitrogen concentration in the process gas during film deposition determined from EDX, XPS and EELS.

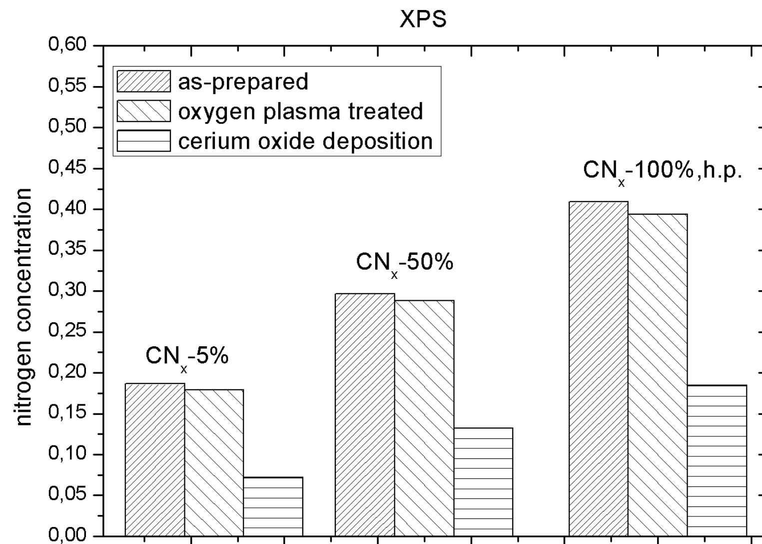

Figure 8.4: Nitrogen concentration in the CN_x films either after 10 minutes of oxygen plasma treatment or the deposition of the cerium oxide film with 2 nm thickness in comparison with the corresponding as-prepared films determined from XPS.

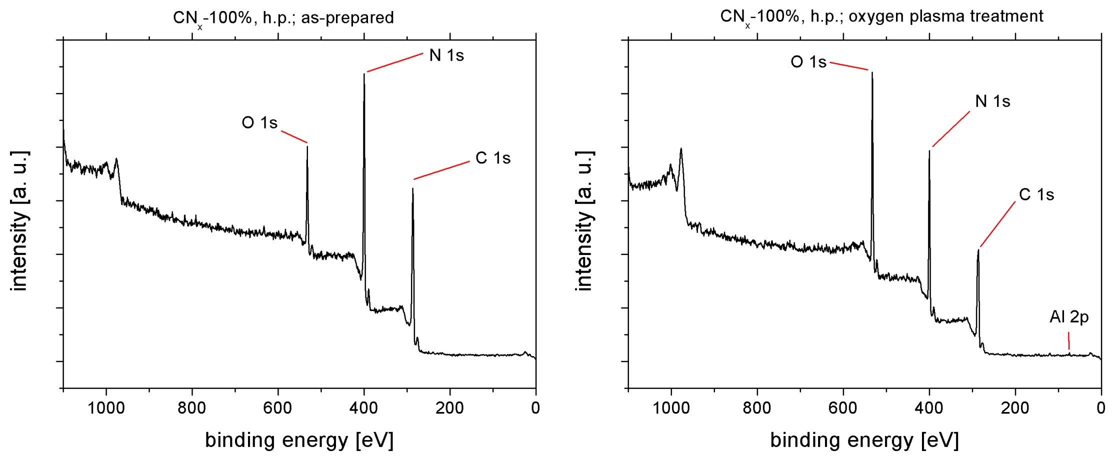

Figure 8.5: Survey spectra of the CN_x100%, h.p. film. Left: as-prepared; right: after 10 minutes of oxygen plasma treatment.

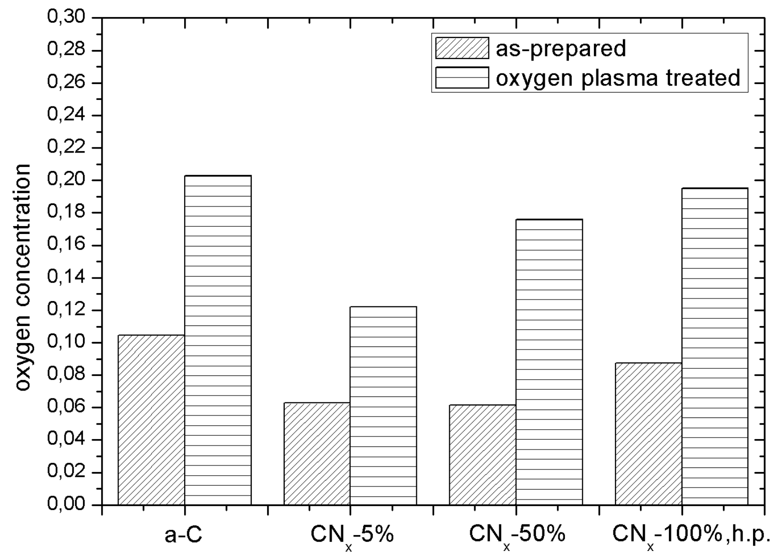

Figure 8.6: Oxygen concentration prior to and after 10 minutes of oxygen plasma treatment determined from XPS.

Chapter 9

Investigation of the stoichiometry of the cerium oxide films depending on the deposition conditions

This chapter deals with the analysis of the XPS spectra Ce 3d of cerium oxide films prepared at various deposition conditions. The main aim of this study was to obtain qualitative information about the stoichiometry of the cerium oxide films depending on the deposition conditions. This includes the influence of: (i) the partial pressure of oxygen in in the working gas used for the cerium oxide film deposition, (ii) the deposition time (i. e. the cerium oxide film thickness) and (iii) the type of the reactive gas component.

9.1 Information about the used samples

For this study, three series of samples have been prepared:

- *Investigation of the influence of the oxygen partial pressure:* Cerium oxide films with 2 nm thickness have been deposited at 0.2 nm/min deposition rate on a-C and CN_x-100%, h.p. single layers with 200 nm thickness on silicon. The process gas used for the cerium oxide deposition was argon/oxygen with oxygen partial pressures reaching from 0 to 10 mPa.

- *Influence of the cerium oxide film thickness:* Cerium oxide films with 2, 10 and 20 nm thickness have been prepared on a-C and CN_x-100%, h.p. single layers with 200 nm thickness on silicon. The process gas was an argon/oxygen gas mixture with $p_{O_2} = 1$ mPa and the cerium oxide deposition rate was 0.2 nm/min.

- *Deposition of cerium oxide in argon/water vapour:* A 2 nm cerium oxide film was deposited on a-C and CN_x-100%, h.p. single layers with 200 nm thickness on silicon in argon/water vapour with $p_{H_2O} = 10$ mPa; the cerium oxide deposition rate was again 0.2 nm/min.

9.2 Influence of the oxygen partial pressure

Figure 9.1 shows the Ce 3d spectra of the 2 nm cerium oxide films prepared at various oxygen partial pressures. The spectra obtained for the cerium oxide films prepared in pure argon give a clear indication that the 4+ oxidation state of cerium is the dominating one; only a small contribution of Ce^{3+} could be detected. This statement is valid for the a-C and the CN_x-100%, h.p. support similarly. The addition of a small amount of oxygen, namely 0.4 and 1 mPa, leads to the growth of cerium oxide films with a significantly increased contribution of Ce^{3+}. This effect is slightly more pronounced in case of the CN_x-100%, h.p. support. This increase of the presence of Ce^{3+} coincides well with the formation of porous cerium oxide/carbon bilayers according to fig. 6.2, p. 48. For the explanation of the increased intensity of the doublets associated with cerium in the 3+ oxidation state two aspects should be taken into account:

1. *Grain size influence:* WU et al investigated the structure of ceria nanoparticles prepared via thermal evaporation in helium by means of EELS [61]. They detected a larger fraction of Ce^{3+} at the surface of the ceria nanoparticles in comparison with the bulk of these particles, which exhibited a stronger signal originating from stoichiometric cerium dioxide. Furthermore, the authors found a correlation between the cerium oxidation state and the CeO_x particle size. In particular, small particles with particle diameters below 4 nm were nearly fully reduced, whereas larger particles with diameters > 10 nm were nearly completely oxidized. Therefore, an increased contribution of Ce^{3+} in the XPS Ce 3d spectrum might be an indication for the presence of small cerium oxide crystallites.

2. *Formation of cerium carbides:* LAVKOVA et al. found clear indications for the presence of cerium carbides at the interface between sputtered cerium oxide films and graphite foil substrates [16, 62]. The removal of the cerium oxide film by means of H_2SO_4 and subsequent XPS analysis delivered a weak Ce 3d signal originating solely from cerium in the 3+ oxidation state. This result was interpreted as an indication that residuals of the cerium oxide film in the form of cerium carbides are responsible for the Ce 3d signal delivering peaks at similar binding energies as in case of non-stiochiometric cerium oxide. In the work [62] it was shown that carbides of cerium are likewise present in case of cerium oxide films deposited on carbonaceous films (a-C or CN_x, respectively) and, therefore, contribute to the doublets associated with Ce^{3+}.

Further increase of the oxygen partial pressure to 4 and 10 mPa leads to the growth of cerium oxide films with cerium mostly in the 4+ oxidation state. Whereas a small contribution of Ce^{3+} could be detected for the CN_x-100%, h.p. supported cerium oxide film, the a-C supported one is nearly completely oxidized. This effect can be likewise correlated with the morphology of the bilayers: For the cerium oxide films deposited at oxygen partial pressures above 4 mPa, the resulting cerium oxide/carbon bilayer bilayers grow more compact according to fig. 6.2, p. 48.

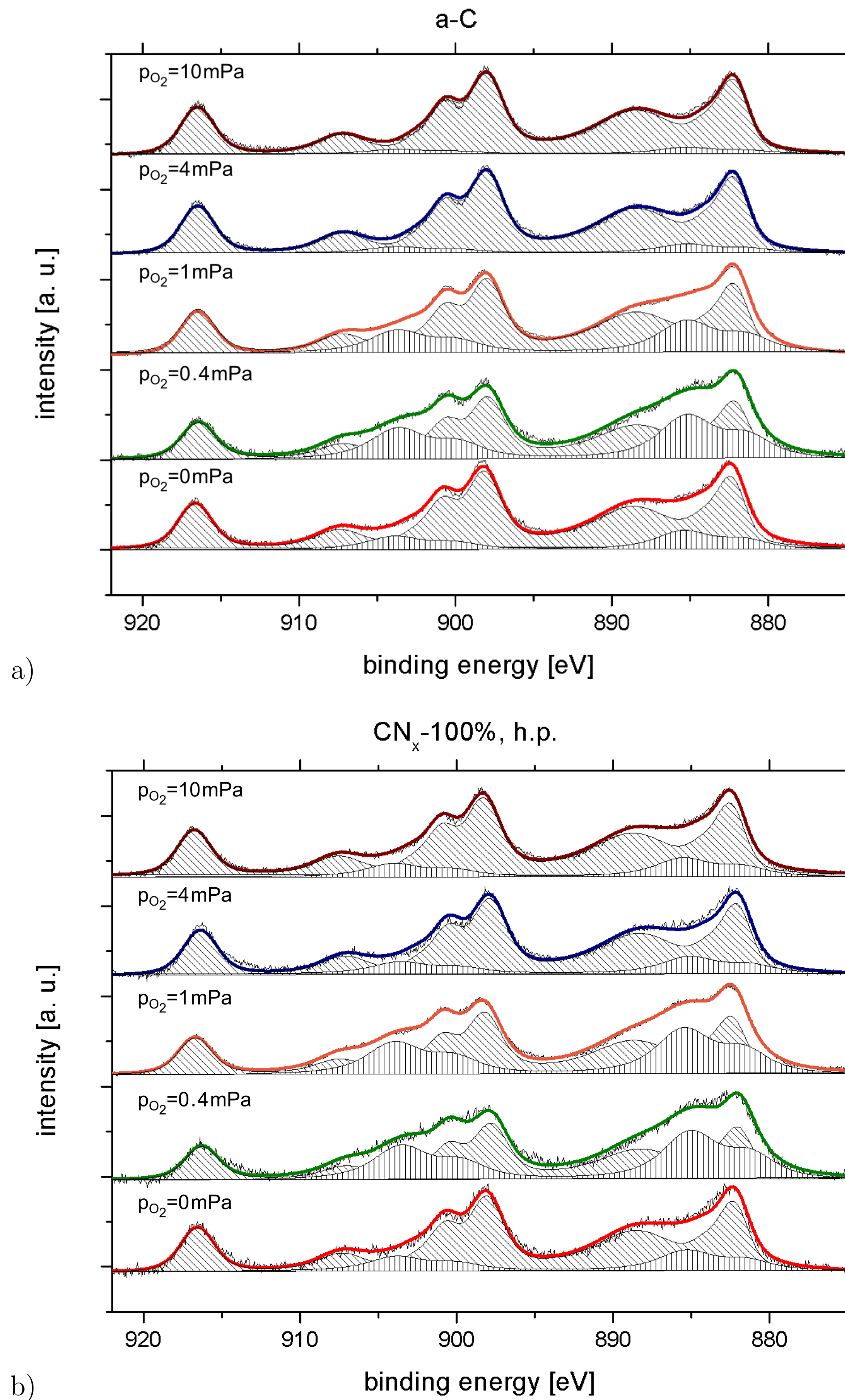

Figure 9.1: Spectra Ce 3d of the 2 nm cerium oxide films deposited on a) a-C and b) CN_x-100%, h.p. in argon/oxygen at various oxygen partial pressures. The spectra have been normalized to the same height.

9.3 Influence of the cerium oxide film thickness

Figure 9.2 shows the Ce 3d spectra of cerium oxide films with 2, 10 and 20 nm thickness prepared in argon/oxygen with $p_{O_2} = 1\,\mathrm{mPa}$. It is evident that the contribution of Ce^{3+} is considerably lower for the thicker films in comparison with the 2 nm films. It can be concluded that a large contribution of Ce^{3+} appears in the vicinity of the cerium oxide/carbon interface. The decrease of the Ce^{3+} contribution for the thicker cerium oxide films can be found in case of both carbon supports similarly. However, whereas the 20 nm cerium oxide film deposited on a-C is nearly completely oxidized, the CN_x-100%, h.p. supported one shows a small contribution of the Ce^{3+}-related doublets.

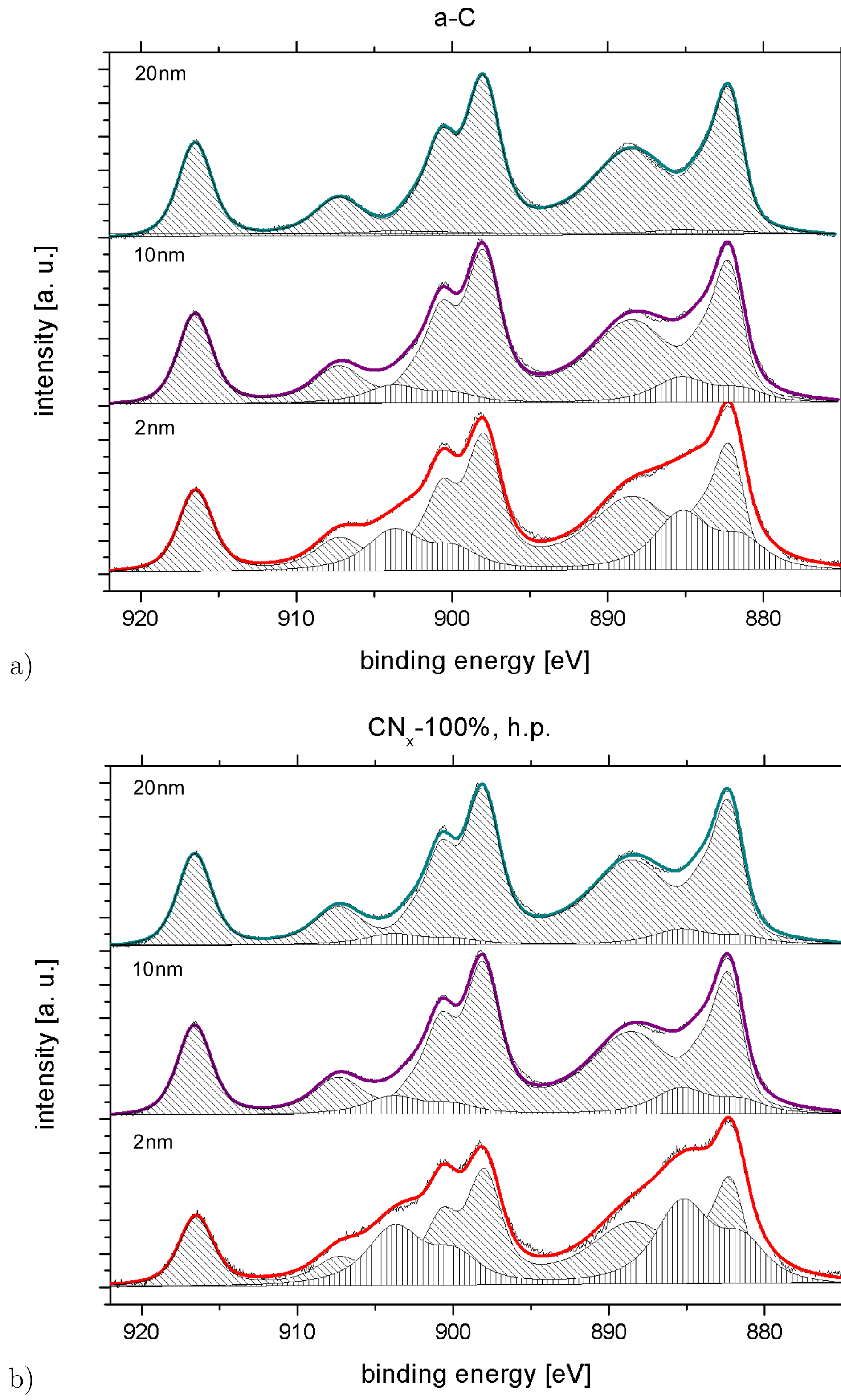

Figure 9.2: Spectra Ce 3d of cerium oxide films deposited on a) a-C and b) CN_x-100%, h.p. in argon/oxygen at $p_{O_2} = 1\,\mathrm{mPa}$ and 0.2 nm/min deposition rate. The cerium oxide film thickness is 2, 10 and 20 nm. The spectra have been normalized to the same height.

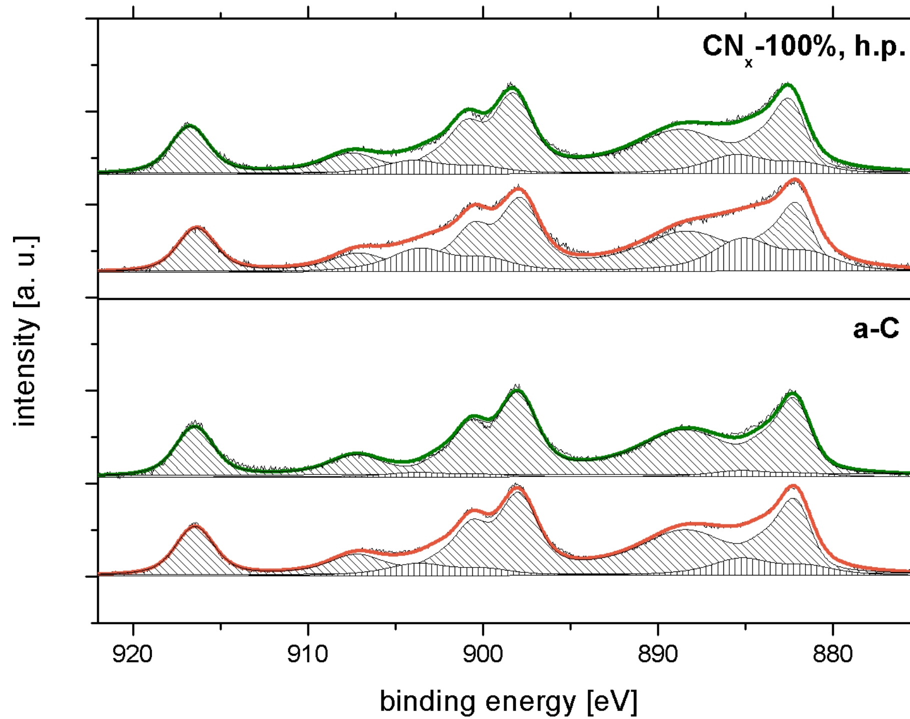

Figure 9.3: Spectra Ce 3d of a 2 nm cerium oxide films deposited on CN_x-100%, h.p. (top) and a-C (bottom), respectively. The spectra of the films deposited in argon/water vapour are compared with the spectra of the films prepared in argon/oxygen at the same partial pressure of the reactive gas component, which was 10 mPa. The cerium oxide deposition rate was 0.2 nm/min. The spectra have been normalized to the same height.

9.4 Deposition in argon/oxygen vs. argon/water vapour

Figure 9.3 shows the spectra Ce 3d of cerium oxide films with 2 nm thickness deposited on CN_x-100%, h.p. and a-C, respectively, in argon/water vapour at $p_{H_2O} = 10$ mPa. The corresponding spectra of cerium oxide films prepared in argon/oxygen with $p_{O_2} = 10$ mPa are shown for comparison. Obviously, the contribution of Ce^{3+} is slightly higher for both films prepared in the presence of water vapour. This correlates well with the finding that the water vapour is a more effective etching agent for carbonaceous films leading to the formation of more porous bilayers (compare fig. 6.8, p. 57 and fig. 6.2, p. 48).

Chapter 10

Structural properties of the as-prepared carbonaceous films

The capability of both elements, carbon and nitrogen, to adopt different states of hybridization (sp, sp^2 and sp^3) plays an important role in the formation of the variety of local bonding environments and, consequently, CN_x structures. The proportion and arrangement of the local bonds depend on the N incorporation into the carbon network and is determined by the preparation technique as well as the treatment conditions. For this reason, this chapter concerns investigations related to the chemical composition and local structure of the as-prepared carbonaceous films by means of Photoelectron Spectroscopy (PES). The first part is focused on the bulk properties studied by means of HAXPES; the second part deals with a depth profiling study using the PES technique at various incident photon energies in the range of 380 — 5950 eV.

10.1 Investigation of the bulk properties by means of HAXPES

10.1.1 Information about the used samples

Due to the large information depth of the HAXPES method (30 — 50 nm) a series of carbonaceous single layers was prepared in various argon/nitrogen gas mixtures with nitrogen concentrations reaching from 0% to 100% including the CN_x-100%, h.p. film. The substrate was silicon and the thickness of the deposited carbonaceous films was $\approx$ 80 nm, which was the highest film thickness which could be deposited without delamination. The chemical composition in the bulk of the as-prepared carbonaceous films was investigated by means of HAXPES using the photon energy of 5950 eV.

10.1.2 Results

The corresponding C 1s and N 1s spectra normalized to the same height are shown in fig. 10.1; the C 1s spectrum of the graphite foil as well as the N 1s spectrum for the a-C film are shown for comparative purposes. The N 1s spectrum for the a-C film is multiplied several times because of the negligibly small nitrogen

concentration (≈ 0.3%). All spectra in this figure have been normalized to the same height.

Discussion of the N 1s spectra

In accordance with literature, e. g. [30, 31, 63, 64], the N 1s spectra were fitted with four Gaussian peaks appearing at the following binding energies:

$$\begin{aligned} \text{N1} &\Longleftrightarrow 398.2\,\text{eV} \\ \text{N2} &\Longleftrightarrow 399.2\,\text{eV} \\ \text{N3} &\Longleftrightarrow 400.2...401.1\,\text{eV} \\ \text{N4} &\Longleftrightarrow 402.3\,\text{eV} \end{aligned}$$

Several peak interpretations can be found in the literature:

- *Interpretation of peak N1:* Souto et al. provided calculations of the N 1s binding energy for several C—N bonding configurations [65]. According to this study, peak N1 fits well with the binding energy of **nitrogen bound to sp^3 hybridized carbon**. This interpretation is also used by other authors [31, 64, 66, 67].

  Hellgren et al. performed an XPS and NEXAFS analysis of magnetron sputtered nitrogenated carbon films [30]. Their results give a clear indication that N1 might be correlated with nitrogen in a pyridine-like environment. Gammon et al. performed a comparison of the N 1s binding energies of magnetron sputtered CN_x films with those of organic reference compounds containing carbon and nitrogen in various bonding configurations. They came to the conclusion that peak N1 can be assigned to the sp^3 nitrogen bonded to sp^3 hybridized carbon as well as to the **pyridine-like N bonding configurations at the perimeter of the vacancy defects sites**, i. e. sp^2 N bonded to two sp^2 carbon atoms. This type of bonding along the perimeter of the defect exhibits an energy shift of about 1 eV to lower binding energy in comparison to the state commonly associated with N bonded in pyridine-like configuration [34].

- *Interpretation of peak N2:* This peak is commonly associated with **carbon in pyridine-like environment** and **nitriles** [30, 34, 65, 68].

- *Interpretation of peak N3:* According to the calculations of Hellgren et al., this peak is very likely correlated with **nitrogen in graphite-like environment** [30]. For this type of nitrogen arrangement, an N1-N3 peak separation of > 2.0 eV is typical. This interpretation is widely used by other authors [31, 64, 66, 67]. For higher N concentrations (> 15 at.%), the graphite planes with N atoms in substitutional positions tend to become curved and **fullerenes** are formed. The binding energy of nitrogen in this structure is reported to be 400.7 eV [30, 35].

  Pels et al. performed an XPS analysis of nitrogen functionalities during pyrolysis of coals and model compounds [69]. The authors observed a peak at 400.3 eV in the XPS N 1s spectrum, which they associated with **pyrrolic**

nitrogen. Wang et al. studied the structural properties of nitrogen-doped graphene by means of XPS. They observed a peak at 400.1 eV, which they likewise correlated with pyrrolic nitrogen [70].

- *Interpretation of peak N4:* This peak is commonly associated with **N—O bonds** [30, 31, 64].

One can see from fig. 10.1 a) that the N 1s spectra of the CN_x films deposited in mixtures of argon and nitrogen exhibit a clearly resolved double peak structure, which vanishes for the CN_x films prepared in pure nitrogen. Furthermore, a shift of peak N3 to lower binding energies with increasing nitrogen concentration in the process gas is clearly visible. A similar peak shift has been reported in the literature by other authors [30, 31, 59, 66, 68] and is explained to be the result of changes of the CN_x film microstructure.

Based on the peak interpretations discussed above, two explanations can be found for the observed peak shift:

1. *Change of the microstructure from a fullerene-like to an amorphous one:* The shift to lower binding energies can be correlated with a change of the microstructure from a fullerene-like to an amorphous one. Hellgren et al. investigated the structural properties of magnetron-sputtered CN_x films prepared at various process conditions (process gas composition, substrate temperature) by means of spectroscopic techniques [30] and High-Resolution Transmission Electron Microscopy (HRTEM) [63]. They could correlate a fullerene-like microstructure of the CN_x film observed with HRTEM with a high binding energy difference between their peaks matching the positions of N1 and N3 in the XPS N 1s spectrum. Likewise, a small binding energy difference could be associated with an amorphous structure of the CN_x film. However, according to the authors a fullerene-like microstructure appears only in case of relatively high substrate temperatures during the film deposition ($> 200°C$) and higher amount of incorporated nitrogen ($> 10 — 15$ at.%); in case of a substrate temperature of 100 °C an amorphous CN_x film forms with the N1-N3 peak separation below 2 eV [35]. In case of the present study, the substrate temperature during film deposition did not exceed 100 °C in all cases making the formation of fullerenes unlikely.

2. *Change of the microstructure from a highly-oriented graphitic phase to lower ordered one and/or formation of pyrrols:* Another possible explanation for the observed shift of peak N3 to lower binding energies with increasing nitrogen concentration in the process gas is proposed in the works [31, 68]. Low nitrogen content in deposited films (below 15 at.%) is reported to be connected to the graphitization of the network due to the incorporation of N substituting C in aromatic clusters. An increase in the nitrogen content enhanced the formation of pentagonal rings. For higher N content, most of the network becomes terminated by pyrrole-like, pyridine-like or nitrile-like configurations. Moreover, at low preparation temperatures nitrogen favors the promotion of sixfold rings in highly disordered networks. According to Pels et al., pyrrolic nitrogen has its N 1s binding energy at 400.3 eV [69]. Tamilarasan et al. performed a study on N-doped graphene and fitted

the N 1s spectra among others with a peak appearing at 400.2 eV, which they likewise correlated with pyrrolic nitrogen [71]. In the frame of this explanation, the increasing formation of pyrrolic nitrogen with increasing nitrogen concentration in the process gas at the expense of graphite-like nitrogen would explain the observed N3 peak shift from higher to lower binding energies.

Likewise, it is evident from fig. 10.1 a) that peaks N1 and N2 increase relatively with increasing nitrogen concentration in the process gas indicating the increasing role of N—sp^3 C bonds, pyridine-like N and nitriles at the expense of graphite-like nitrogen. Peak N2 becomes the dominant one for the CN_x-100%, h.p. film deposited at the higher total gas pressure. This result indicates the dominating role of pyridine-like N and nitriles in this type of films. A similar behaviour was observed by Lazar et al. [31]. They related the core level N 1s spectra with the two main peaks N1 and N3 to nitrogenated amorphous carbon films with low H and N content. The increase in the N3 state was attributed to the growth of aromatic domains containing N. Samples with a large amount of incorporated H and N exhibited main contributions N2 and N3 to the N 1s spectra which were correlated with nitrile configurations and the large N—H bond density.

Discussion of the C 1s spectra

Since the C 1s spectra for CN_x films appear broad and rather featureless in comparison to the N 1s ones, there is an asymmetry on the higher binding-energy side indicating the presence of carbon atoms in at least two different binding states related to nitrogen. Accordingly, the C 1s spectra presented in fig. 10.1 were fitted with up to four Gaussian peaks and one asymmetric peak appearing at the following binding energies:

$$\begin{aligned} \text{C1} &\Longleftrightarrow 284.5\,\text{eV} \\ \text{C2} &\Longleftrightarrow 285.2\,\text{eV} \\ \text{C3} &\Longleftrightarrow 286.2\,\text{eV} \\ \text{C4} &\Longleftrightarrow 287.6\,\text{eV} \\ \text{C5} &\Longleftrightarrow 288.9\,\text{eV} \end{aligned}$$

The peaks can be interpreted as follows:

- *Interpretation of peak C1:* This peak can be correlated with **sp^2 C—C bonds** as in graphene [30, 31, 72, 73]. According to Diaz et al., this peak has to be fitted with an asymmetric Doniach Sunjic function as in graphite [73].

- *Interpretation of peak C2:* A common interpretation of this peak are **sp^3 C—C bonds** [30, 31, 72, 73]. Furthermore, the position of peak C2 matches rather well that one observed in polyethylene indicating that **C—H** bonds may likewise contribute to C2 [74].

- *Interpretation of peak C3:* Usual interpretations are **sp^2 C—N bonds** in the sense of **pyridine-like configurations** and/or the **graphite-like structure** [31, 64, 67, 71, 75, 76].

- *Interpretation of peak C4:* Lazar et al. [31] investigated magnetron sputtered CN_x films with various N and H contents by means of various methods including XPS. The intensity of the peak corresponding to peak C4 in the C 1s spectrum of the present study was found to be correlated with the hydrogen concentration in the CN_x film, i. e. **C=N—H groups**. In the structural study of nitrogenated amorphous carbon films published by Majumdar et al. [77] the C 1s peak positioned at 287.6 eV was assigned to the presence of **nitrile** species. Commonly, this peak is correlated with C—N single bonds of the type **sp^3 C—N** [71, 75, 78] or **sp^2 C—N in nonaromatic C_2N_2 configurations** [31, 64, 76, 79].

- *Interpretation of peak C5:* This peak is commonly correlated with **C—O bonds** usually due to surface oxygen contamination [30, 31, 64].

The spectrum of the graphite foil sample in fig. 10.1 b) can be satisfactorily fitted with peak C1 only indicating the exclusive presence of sp^2 C—C bonds. For the a-C film, a second component C2 is necessary, which is a hint for the presence of sp^3 bonds. For the CN_x films, the maximum of the C 1s spectra is shifted to higher binding energies with a simultaneous broadening of the spectrum due to the presence of C—N bonds. The intensity of the peaks C3 and C4 associated with C—N bonds increases with increasing nitrogen concentration in the process gas. Note that peak C4 develops clearly for the CN_x films deposited in pure nitrogen, i. e. for CN_x-100% and CN_x-100%, h.p..This observation can be explained with the increased incorporation of nitrogen into the carbonaceous film according to fig. 8.3, p. 70.

However, a precise fitting the of C 1s spectra in the sense of the number of individual peaks and their positioning is not possible due to the unresolved features of the C 1s spectra. Likewise, a detailed interpretation of the C 1s components is a difficult task [80]. For example, Majumdar et al. positioned the C 1s peak at 287.6 eV and assigned it to the presence of nitrile species [77]. However, the C 1s component correlated with nitrile bonds is sometimes reported to appear at lower binding energies of 286.1 eV [30] or 286.7 eV [81].

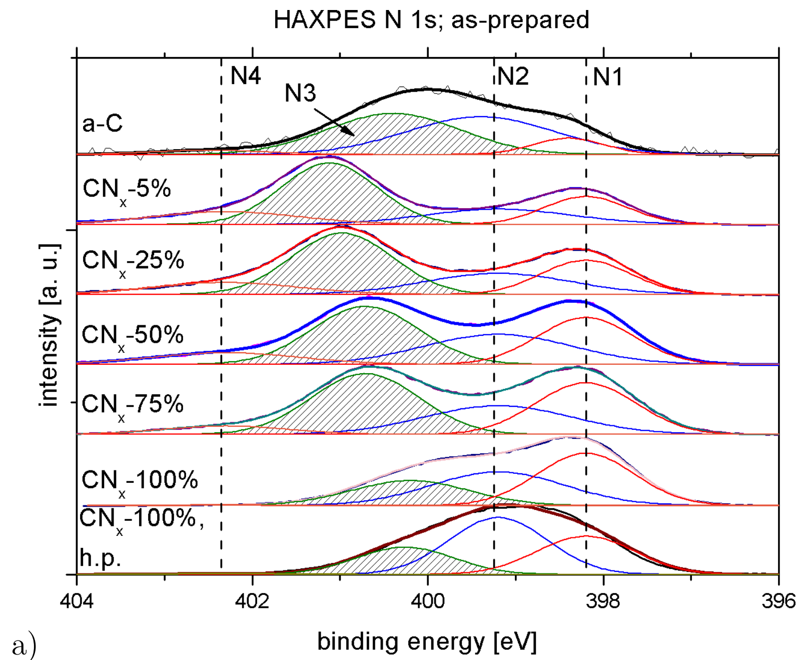

a)

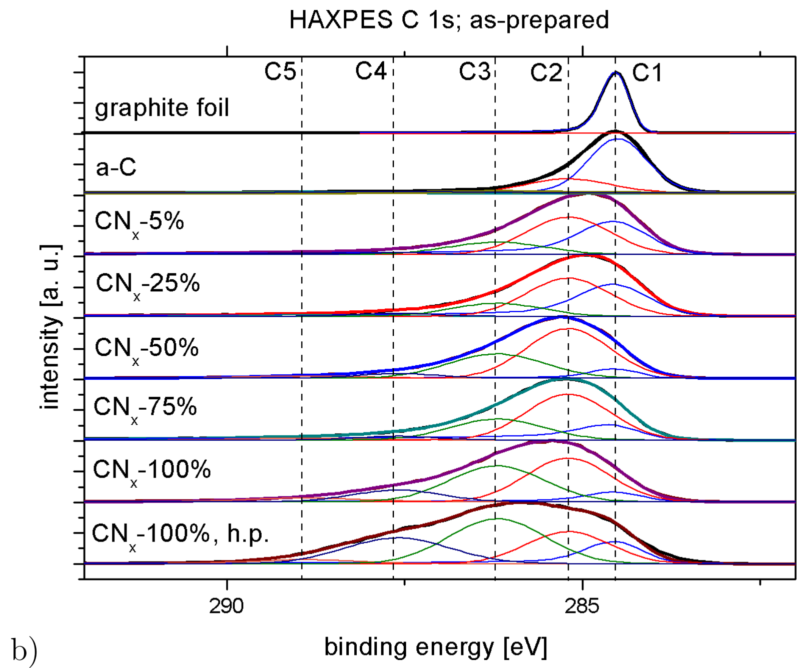

b)

Figure 10.1: HAXPES a) N 1s and b) C 1s spectra of the as-prepared films deposited in various argon/nitrogen gas mixtures with nitrogen concentrations reaching from 0% to 100%. The spectra are normalized to the same height.

type of PES	photon energy [eV]	information depth C 1s [nm]	information depth N 1s [nm]
SRPES	380	2.3 — 3.0	—
SRPES	475	2.9 — 3.8	2.2 — 3.0
SRPES	640	4.1 — 5.5	3.2 — 4.3
XPS	1487	9.9 — 13.2	9.2 — 12.2
HAXPES	5950	35.2 — 46.9	34.6 — 46.1

Table 10.1: List of the types of photoelectron spectroscopies and primary photon energies used for depth profiling of the chemical composition of the CN_x films. The corresponding information depth calculated for the C 1s and N 1s electrons according to [49, 50] is given.

10.2 Depth profiling of the chemical composition

10.2.1 Information about the used samples and experimental techniques

The depth profiling study was performed using the PES technique by means of varying the energy of the incident photons in the range of 380 —- 5950 eV. Table 10.1 summarizes the used primary photon energies and corresponding information depths for photoelectrons originating from carbon or nitrogen atoms. The information depth is determined as triple and quadruple inelastic electron mean free path λ corresponding to 95% and 98% probability that the emitted electron reaches the surface [49]. For the used primary photon energies λ in carbon material was calculated from the Tanuma, Powell, and Penn TPP2M formula [50]. The possibility to use different photon energies allows studying the chemical composition in different subsurface regions of the samples.

For the surface-sensitive methods SRPES and XPS, a series of a-C/CN_x double layers was prepared on silicon substrates including the single layers a-C and CN_x-100%, h.p. (see tab. 4.3, p. 37). The HAXPES data have been taken over from sec. 10.1.2, p. 78.

10.2.2 Results

Figures 10.2 and 10.3 show the C 1s and N 1s core level spectra of the carbonaceous films obtained for five (C 1s) or four (N 1s) various photon energies. The information depth increases with increasing photon energy. That means that for the presented C 1s (N 1s) spectra the information depth increases from bottom to top of each diagram.

As one can see the spectra of all the CN_x films exhibit specific shapes and/or peaks that change with the used photon energy. This observation clearly shows the existence of different chemical environments in the surface regions and in the bulk of these films. First, the N 1s core level spectra are considered. For the CN_x-5% and the CN_x-25% film, peak N3 is the strongest one in the bulk and

decreases in vicinity of the surface of the film. Simultaneously, peak N3 is shifted to lower binding energies. In accordance with sec. 10.1.2, these two explanations are most likely for the peak shift:

1. The peak shift of N3 might be the result of a transition from a well ordered graphite-like phase in the bulk to a lower ordered one in the near-surface region.

2. Increasing formation of pyrrole-like structures at the surface of the carbonaceous film leading to a peak contribution slightly above 400 eV in the N 1s spectrum.

Moreover, there is a hint indicating the formation of pyridine-like structures and/or nitrile groups at the surface of the carbonaceous films — the increase of peak N2 from the bulk to the surface, which is observable for most of the carbonaceous films except the CN_x-100%, h.p. film. In case of the latter one, both peaks N2 and N3 behave opposed in comparison with the films deposited at the lower total gas pressure: N3 increases from the bulk to the surface, whereas N2 decreases. This might be an indication for the increased presence of pyrrolic and/or graphite-like nitrogen at the surface at the expense of pyridine- and nitrile-like N in this film.

The observation of clear trends in the C 1s spectra is more difficult due to the large number of possible bonding configurations and the complex shape of the spectra. However, the following statements can be made:

- In case of the CN_x-5% film, peak C1 associated with graphite-like C—C bonds decreases from the bulk to the surface of the film in contrast to the increasing peaks C2 and C3. This would be in accordance with the observation from the N 1s spectra that the graphite-like structure of the film in the bulk changes into a disordered one at the surface with the enhanced presence of pyrrolic, pyridinic or nitrile-like N.

- For the films with higher concentration of nitrogen, the states C3 and C4 become more pronounced showing the enhanced formation of aromatic species as well as nitride and/or sp^2 C—N bonds. Peak C4 is increasing when moving from the bulk to the surface regions of the CN_x layers for all of the films prepared at the lower total pressure of the process gas, if the HAXPES and XPS spectra are considered mainly. Contrary to the CN_x-5% film, the decrease of the peak C1 is not observed.

- For the CN_x-100%, h.p. film, the appearence of strong peaks C3 and C4 in the bulk indicates the presence of a large contribution of pyridinic nitrogen, nitrile and/or sp^2 C—N species as well as N bound to sp^3 C. The latter one decreases in the near-surface region according to the N 1s spectra.

- The C 1s spectrum of the CN_x-100%, h.p. film exhibits a relatively strong contribution C5 in the surface region indicating a large presence of C—O bonds. This finding is in correlation with the XPS results (see fig. 8.6, p. 71) showing an oxygen concentration of approximately 10%.

The series of the C 1s and N 1s spectra presented in figs. 10.2 and 10.3 allow to check the nitrogen content in different subsurface regions of the CN_x films. The nitrogen concentrations, calculated from the total area of the C 1s and N 1s spectra using the corresponding photoionization cross-sections for given photon energy and element, are summarized in tab. 10.2 for two different information depths.

	Information depth [nm]	
layer type	2 — 3	9 — 13
CN_x-5%	8.1%	15.0%
CN_x-25%	25.6%	27.9%
CN_x-50%	24.9%	26.4%
CN_x-75%	19.3%	29.1%
CN_x-100%	18.8%	27.6%
CN_x-100%, h.p.	36.5%	39.4%

Table 10.2: Nitrogen concentrations in the as-prepared CN_x films for two different PES information depths.

as-prepared

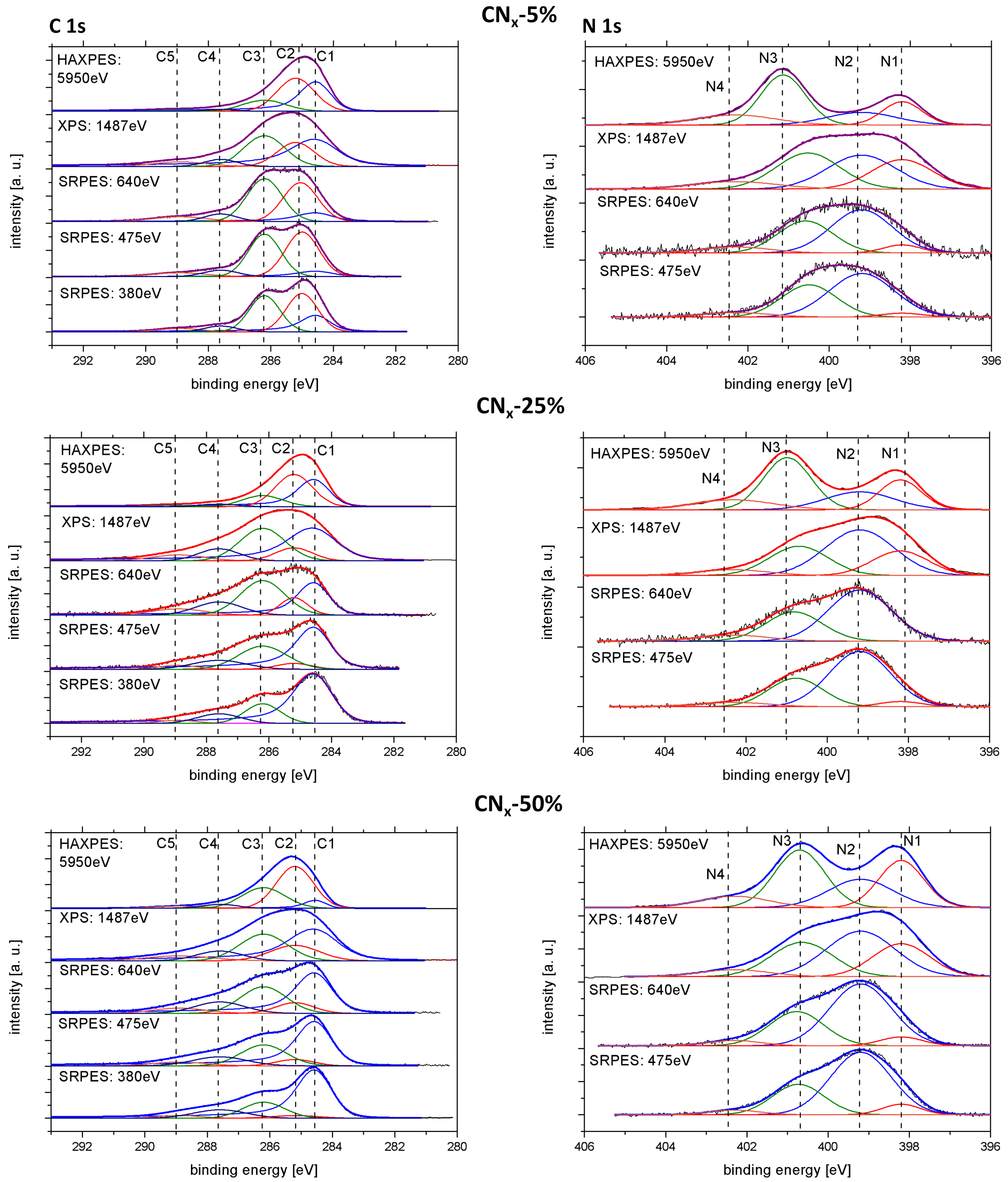

Figure 10.2: Summary of the C 1s (left) and N 1s (right) core-level spectra of the as-prepared carbonaceous films CN_x-5%, CN_x-25% and CN_x-50%. The spectra are normalized to the same height.

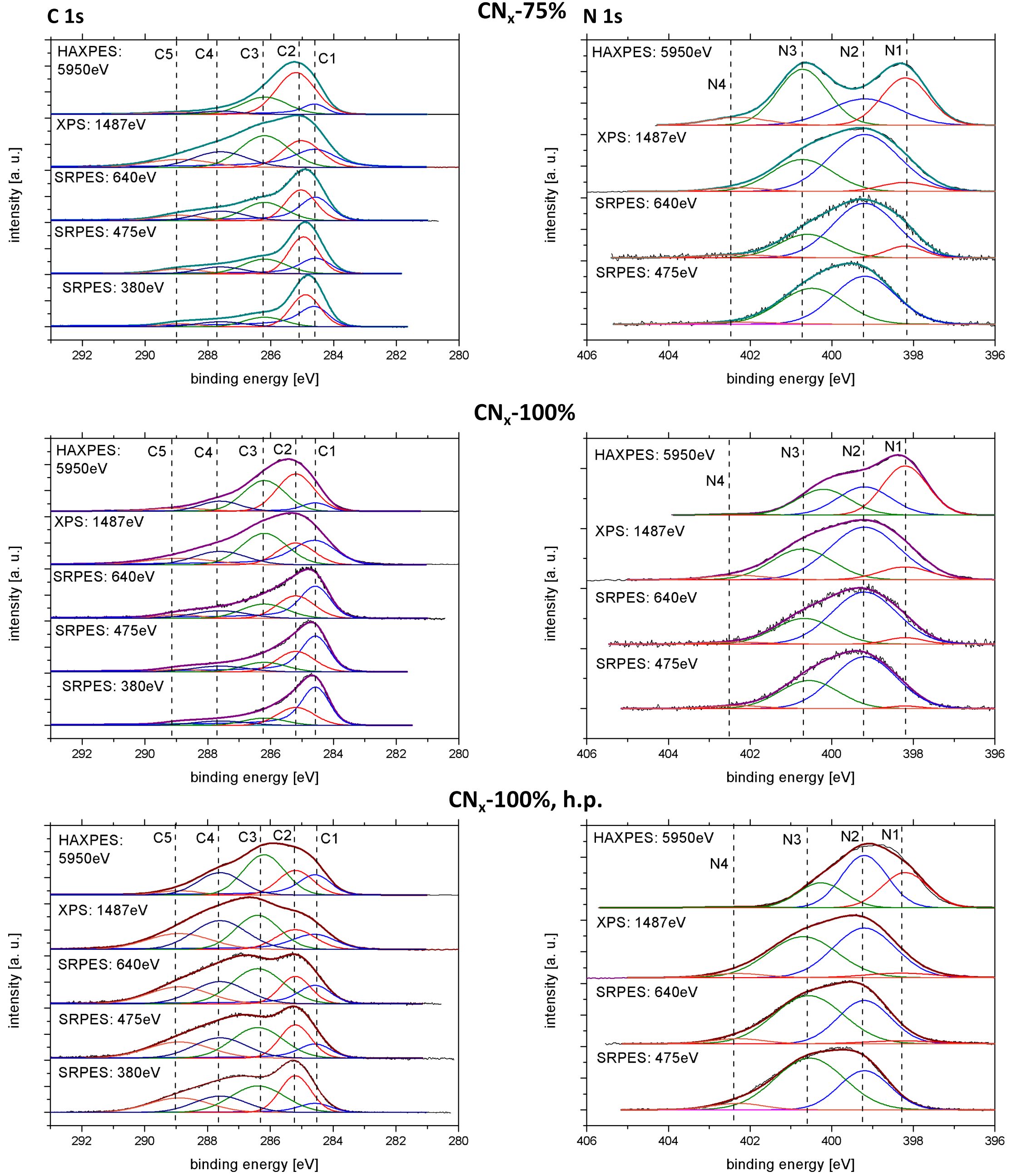

Figure 10.3: Summary of the C 1s (left) and N 1s (right) core-level spectra of the as-prepared carbonaceous films CN_x-75%, CN_x-100% and CN_x-100%, h.p.. The spectra are normalized to the same height.

Chapter 11

Chemical composition of the oxygen plasma treated and cerium oxide covered carbonaceous films

In this chapter, the chemical composition of the carbonaceous films after oxygen plasma treatment and cerium oxide deposition studied by means of PES is presented. The first part of the chapter focusses on the investigation of the bulk properties of the films by means of HAXPES, whereas the second part considers the depth profiling of the chemical composition by means of the various PES techniques using several photon energies in the range of 380 — 5950 eV (see tab. 10.1, p. 84) .

11.1 Investigation of the bulk properties by means of HAXPES

11.1.1 Information about the used samples

For this part of the study, a complete series of carbonaceous single layers with 80 nm thickness deposited on silicon substrates in different gas mixtures of argon and nitrogen with nitrogen concentrations in the process gas reaching from 0% to 100%, including the CN_x-100%, h.p. film prepared at the higher total gas pressure, was used. These films have been either treated in oxygen plasma for 10 minutes or covered with a 2 nm cerium oxide film prepared via magnetron sputtering using an argon/oxygen gas mixture with $p_{O_2} = 1$ mPa at the deposition rate of 0.2 nm/min.

11.1.2 Results

The C 1s and N 1s core level spectra obtained from the HAXPES measurement are shown in fig. 11.1 for the oxygen plasma treated and cerium oxide covered carbonaceus films; the spectra of the as-prepared films are shown for comparative purposes. The N 1s and C 1s spectra are discussed in the following paragraphs separately.

N 1s spectra. The comparison of the N 1s spectra of the oxygen plasma treated and cerium oxide covered CN_x-5% and CN_x-25% with the spectra of the as-prepared films reveals a similar trend as it was observed for the as-prepared films with increasing nitrogen concentration in the process gas (sec. 10.1.2, p. 78): The binding energy difference between peaks N1 and N3 is considerably reduced. This evolution is accompanied by a significant decrease of the peak ratio N3/N1. This trend can be explained similarly as in case of the as-prepared films: (i) with a transition from a well ordered to a less ordered graphitic structure or (ii) with a transition of graphite-like N to pyrrolic N. However, due to the large information depth of the HAXPES method (several tens of nm), the obtained result indicates that the damage of the CN_x films is not only concentrated at the surface region of the film, but occurs likewise in much deeper regions. CZIGANY et al. investigated the influence of argon ion bomardment on the structural properties of magnetron sputtered CN_x films for various ion energies [59]. They observed an amorphization of the CN_x film exhibiting a fullerene-like structure in the as-prepared state for ion energies in the keV-range. The depth of the damaged area increased with the ion energy and reached up to 12 nm. The evolution of the XPS N 1s spectra presented in [59], namely the peak shift as well as the decrease of the peak associated with nitrogen in a graphite-like environment, is in rather good agreement with the evolution of the HAXPES N 1s spectra in the present study. This result indicates that oxygen plasma treatment with oxygen ions exhibiting energies far below 1 keV cause a similar damage as argon ions with energies in the keV-range.

Peak contribution N2 associated with nitriles and nitrogen in a pyridine-like environment remains nearly unchanged for the films prepared at the low total gas pressure except the CN_x-5% layer. In this case, the damage of the graphitic structure with incorporated nitrogen atoms probably let to the formation of nitrile species resulting in a more pronounced peak N2. In case of the CN_x-100%, h.p. film deposited at the higher process gas pressure, peak contribution N2 is the dominating one in the as-prepared film indicating that a considerable fraction of nitrogen is bound in nitrile and pyridine-like bonding configurations. This peak contribution is suppressed slightly by oxygen plasma treatment and much more by cerium oxide deposition. It is neccessary to note that the duration of both of the processes is comparable ($\approx$ 10 min).

C 1s spectra. The C 1s spectra of the a-C and CN_x films reveal no significant changes in the shape when comparing the as-prepared films with the oxygen plasma treated and cerium oxide covered ones except the ones of CN_x-100%. It points to the decomposition of aromatic structures by plasma treatment. This effect is much stronger in case of cerium oxide sputter deposition in the presence of oxygen in the process gas. Not only aromatic structures are affected: peak C4 associated with nitriles and/or sp^2 C—N or sp^3 C—N configurations is likewise diminshed significantly.

Valence band spectra. In order to shed light upon changes in the nitrogen bonding environment due to the plasma treatment, valence band (VB) spectra of the as-prepared CN_x films and the oxygen plasma treated ones are compared in fig. 11.2. The valence bands of the CN_x layers covered with cerium oxide are not

taken into consideration due to superposition effects with the signal originating from cerium oxide in this region.

According to HELLGREN et al. [30], a valence band feature observed for all the CN_x films at 4.5 eV (see fig. 11.2) can be attributed to the presence of nitrogen in pyridine-like and graphite-like bonding environments. A shoulder located at approximately 6.5 eV indicates the formation of nitrile groups. This shape seems to be more pronounced for the as-prepared layers CN_x-75%, CN_x-100% as well as CN_x-100%, h.p.. Its appearance in the VB spectra for all the CN_x films after oxygen plasma treatment points to changes in the local bonding structure of nitrogen in favour of nitrile bonds.

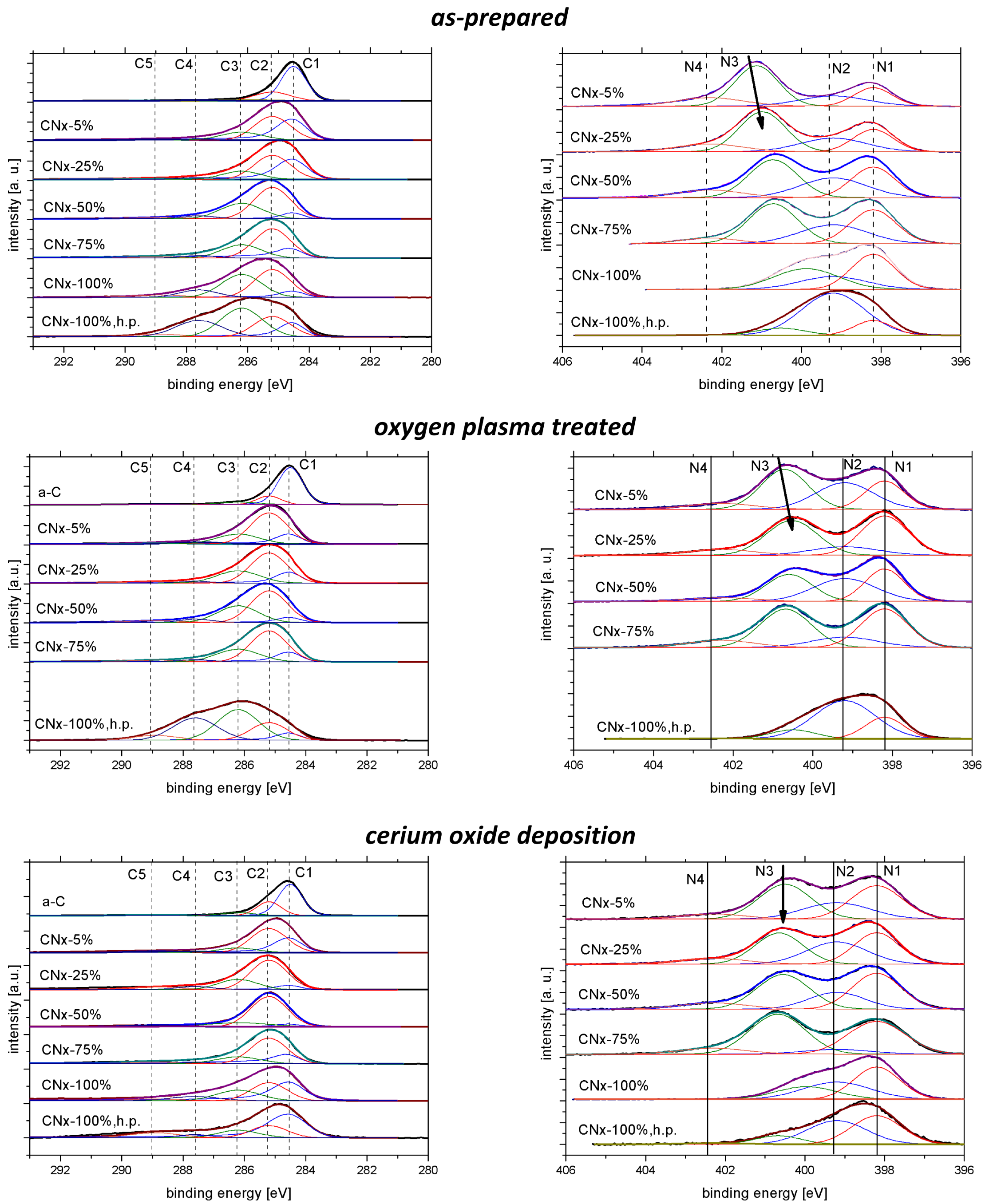

Figure 11.1: Photoelectron spectra of the as-prepared, oxygen plasma treated and cerium oxide covered carbonaceous films obtained from the HAXPES measurement. Left: C 1s spectra; right: N 1s spectra. The spectra are normalized to the same height.

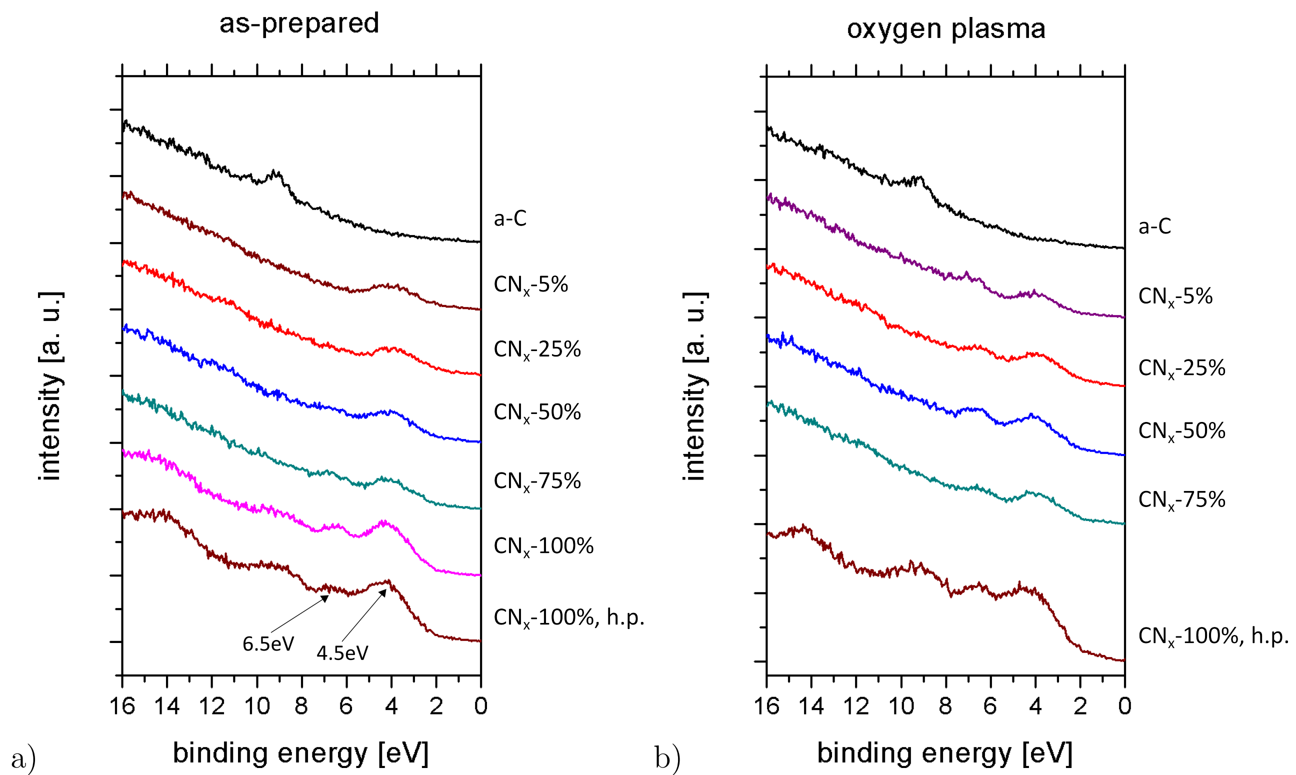

Figure 11.2: HAXPES valence band (VB) spectra of the a) as-prepared and b) oxygen plasma treated carbonaceous films.

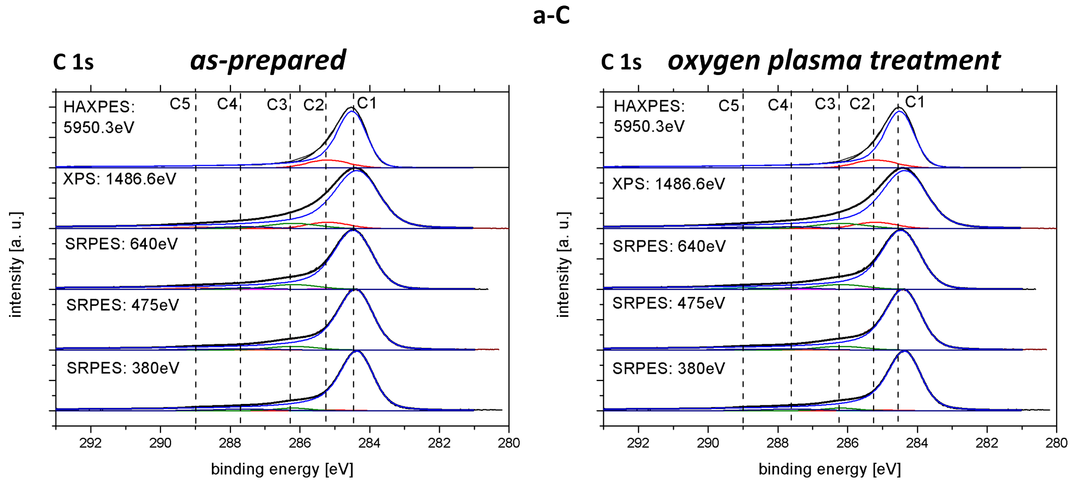

Figure 11.3: Summary of the C 1s core level spectra of the oxygen plasma treated a-C film (right); the spectra of the as-prepared film are shown for comparison (left).

11.2 Depth profiling of the chemical composition

11.2.1 Information about the used samples

For this study performed by the PES techniques using several different photon energies in the range of 380 — 5950 eV (tab. 10.1, p. 84) the following series of samples have been prepared:

- *Oxygen plasma treatment:* Three various carbonaceous films on silicon substrates have been treated in oxygen plasma for 10 minutes, namely the a-C and CN_x-100%, h.p. single layers. In addition, the CN_x-50% film was studied in the form of the double layer according to tab. 4.3, p. 37 for the surface sensitive SRPES and XPS methods; the HAXPES data have been taken over from sec. 11.1.

- *Cerium oxide deposition:* For this study, these four carbonaceous films on silicon substrates have been considered: a-C, CN_x-5%, CN_x-50% and CN_x-100%. The former one was a single layer, wheras the CN_x films were double layers according to tab. 4.3, p. 37 in case of the surface sensitive SRPES and XPS methods; the HAXPES data have been taken over from sec. 11.1. The carbonaceous films were covered with a 2 nm cerium oxide film sputter-deposited in argon/oxygen with $p_{O_2} = 1$ mPa and a deposition rate of 0.2 nm/min.

11.2.2 Results of the oxygen plasma treatment

The PES N 1s and C 1s core level spectra of the carbonaceous films investigated in this study are shown in figs. 11.3 — 11.5 for the a-C, CN_x-50% and CN_x-100%, h.p. films. It is obvious that peak N3 increases with respect to the other two components in case of the surface-sensitive spectra, which is observable for

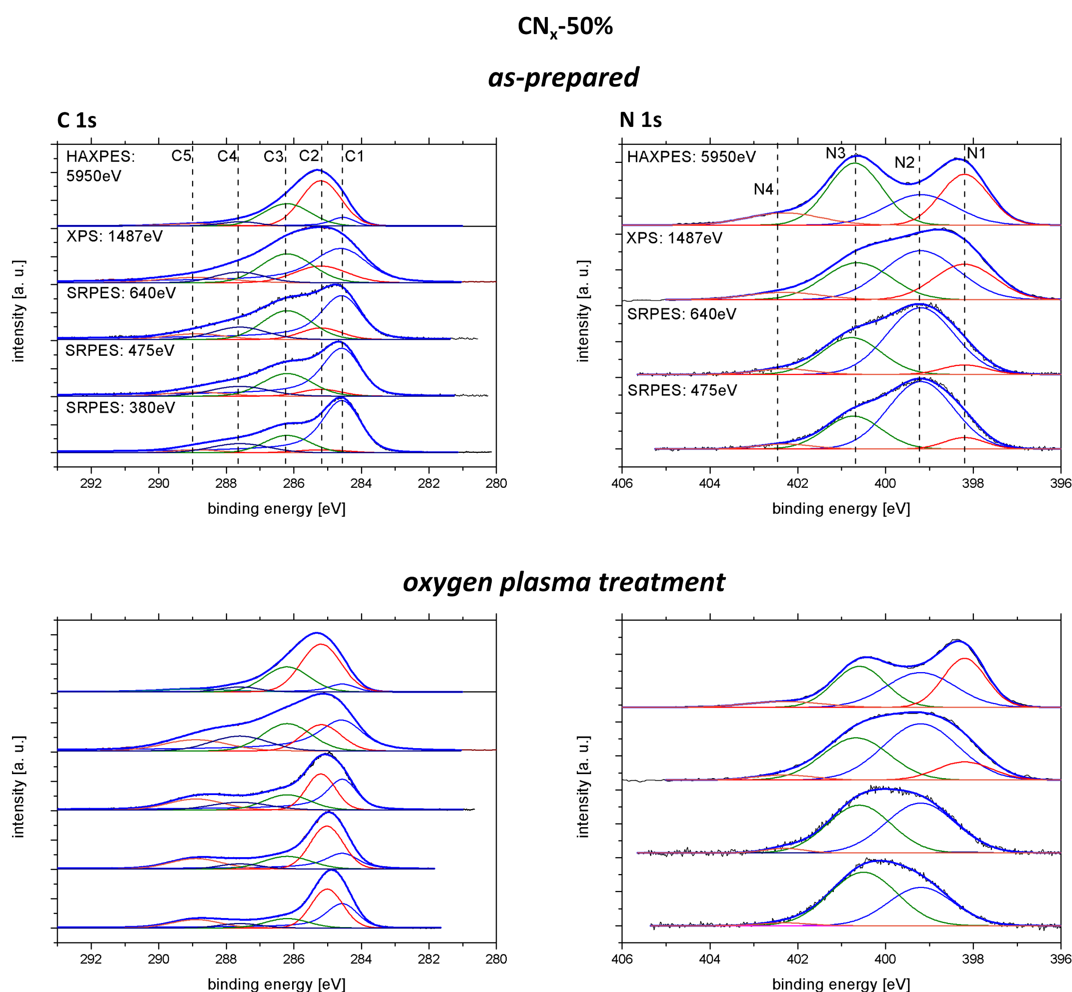

Figure 11.4: Summary of the C 1s and N 1s core level spectra of the oxygen plasma treated CN_x-50% film; the spectra of the as-prepared film are shown for comparison. All spectra are normalized to the same height.

both of the studied CN_x films. This result indicates that nitrogen in a graphite-like environment and pyrrolic N is the most stable C–N bonding configuration in comparison with pyridine-like bonds (N2 and N1 states). Peak N1 vanishes completely for the oxygen plasma treated film indicating that pyridine-like bonds at the perimeter of the defects sites and N bound to sp^3 C are effectively destroyed under the influence of oxygen plasma in the near-surface region.

In the C 1s spectra, the damage of the C—N bonds is observable from diminished states C3 and C4 going from the bulk to surface regions of the CN_x films. In the near-surface regions, peak C4 is missing completely for the CN_x-100%, h.p. film. On the other hand, peak C5 increases for both CN_x films after oxygen plasma treatment indicating an increased formation of C—O bonds. However, for the a-C film no considerable increase of C5 is visible after oxygen plasma treatment.

Strong nitrogen depletion in the near-surface regions is observable after 10 minutes of oxygen plasma treatment (see figs. 11.4 and 11.5), while deeper areas of the CN_x films are affected only slightly. In order to obtain a deeper insight into the time dependence of the oxygen plasma influence on the CN_x layer composition,

CN_x-100%, h.p.

as-prepared

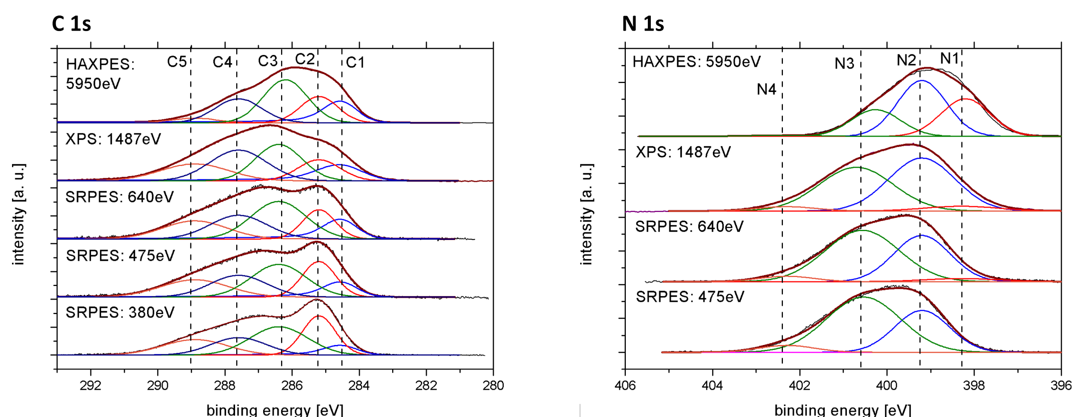

oxygen plasma treatment

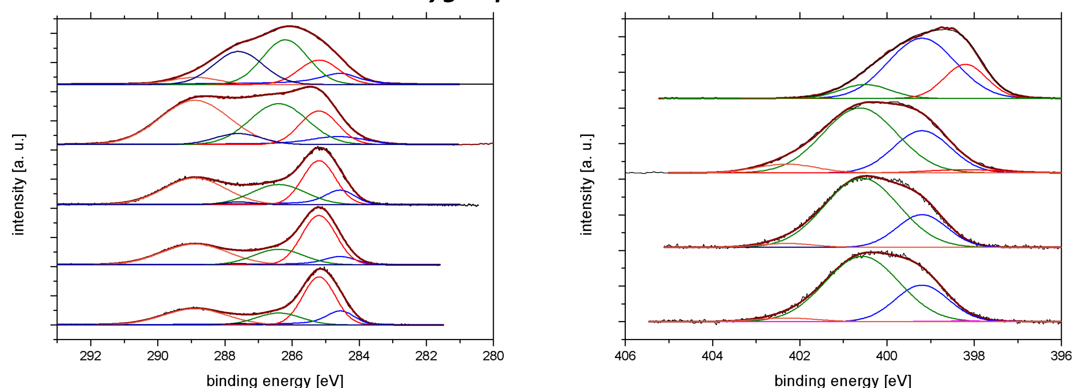

Figure 11.5: Summary of the C 1s and N 1s core level spectra of the oxygen plasma treated CN_x-100%, h.p. film; the spectra of the as-prepared film are shown for comparison. All spectra are normalized to the same height.

an XPS measurement was performed. In fig. 11.6 the evolution of the C 1s and N 1s spectra is presented as a function of the duration of the plasma treatment exemplarily for the CN_x-100%, h.p. film. One can see that peak N2 in the N 1s spectrum related to the pyridine-like bonding structures decreases with increasing duration of the oxygen plasma treatment accompanied by a diminution of the peak C3 and simultaneous increase of the peak C5 in the C 1s spectrum. The damage of the N—C bonds in aromatic environments is followed by carbon oxidation and nitrogen depletion of the surface regions. The nitrogen concentration in the CN_x-100%, h.p. film calculated from the XPS data decreases from 39.7% to 35.7% after 30 min impact of oxygen plasma.

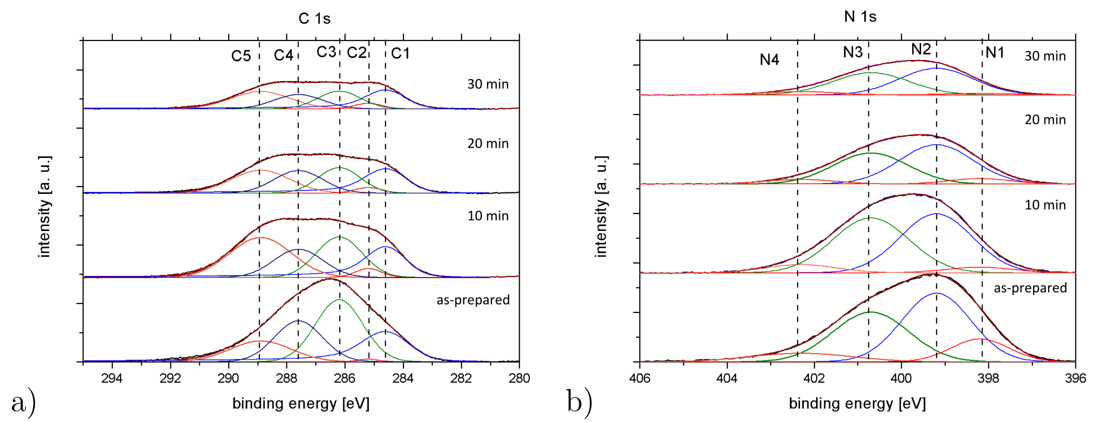

Figure 11.6: Summary of the a) C 1s and b) N 1s core level spectra of the CN_x-100%, h.p. film (as-prepared and after various durations of oxygen plasma treatment).

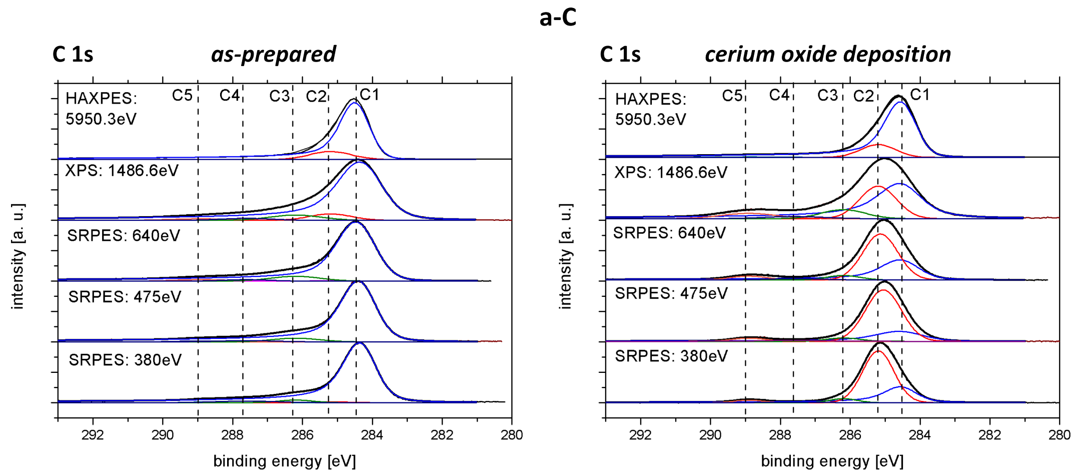

Figure 11.7: Summary of the C 1s spectra of the cerium oxide covered a-C film; the spectra of the as-prepared film are shown for comparison. The spectra are normalized to the same height.

11.2.3 Results of the cerium oxide deposition

The PES spectra of the cerium oxide covered carbonaceous films are shown in figs. 11.7 — 11.10. For the a-C film (fig. 11.7), the performed depth profiling clearly shows changes in the contribution C2 in the near-surface region indicating that cerium oxide sputter deposition leads to the degradation of the graphite-like structures in favour of a large fraction of sp^3 hybridized carbon. A strong peak C2 is likewise present in the C 1s spectra for all the CN_x films covered with cerium oxide (figs. 11.8 — 11.10). Furthermore, an increased contribution C5 is visible in the cerium oxide covered films indicating the formation of C—O bonds. The peaks related to C—N bonds decrease considerably after the cerium oxide deposition indicating a depletion of nitrogen in the carbonaceous film.

From the N 1s spectra of the CN_x films reliable statements regarding the intensity of the individual peak contributions are difficult in the near-surface region due to the weak signal. This evolution is similar to that one observed in case of the oxygen plasma treated films, but the effect is much stronger as it can be seen from fig. 11.11. Here, the XPS C 1s and N 1s core level spectra of the CN_x-100%, h.p. films are presented before and after 40 min oxygen plasma treatment and compared with the ones of the films covered by cerium oxide films with 5 and 20 nm thickness. Note that the intensities of the spectra are not normalized in this case.

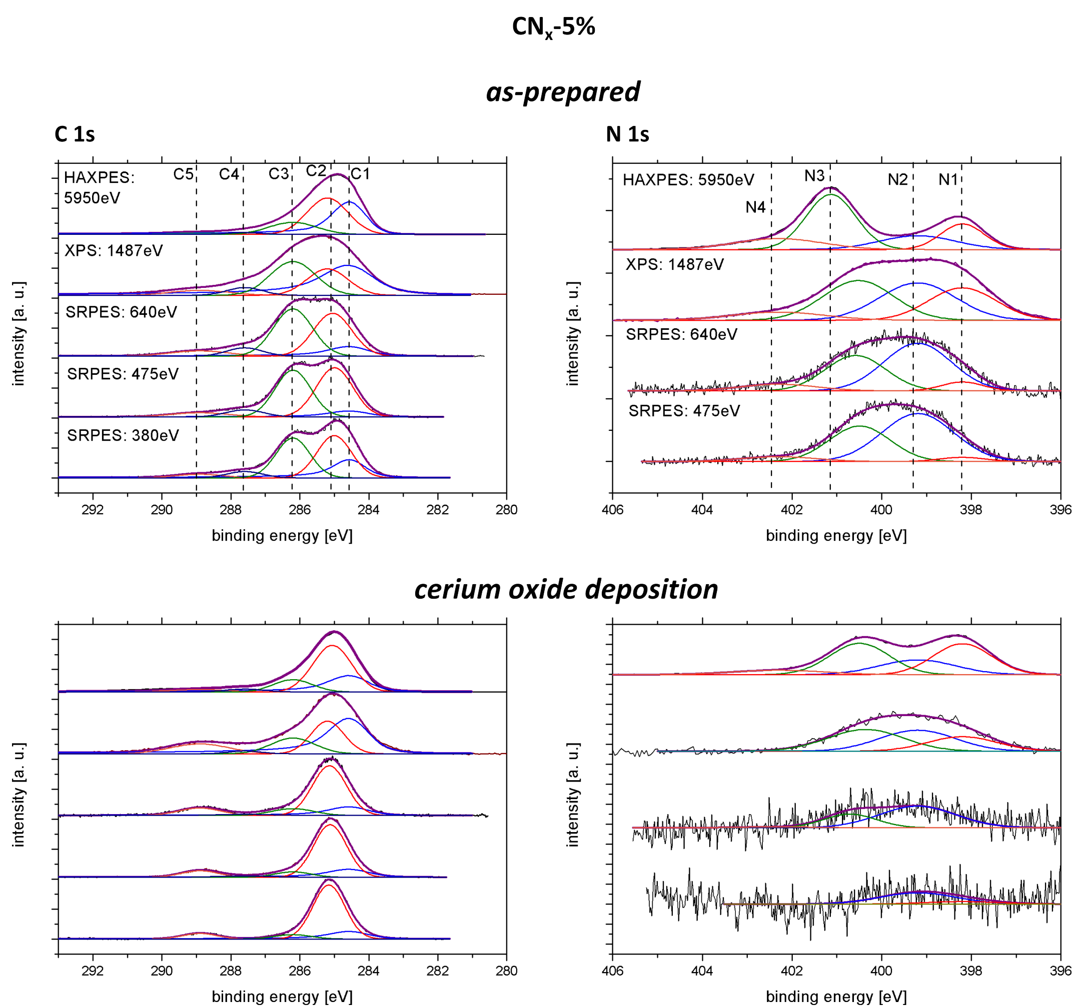

Figure 11.8: Summary of the C 1s and N 1s spectra of the cerium oxide covered CN_x-5% film; the spectra of the as-prepared film are shown for comparison. The spectra are normalized to the same height.

CN_x-50%

as-prepared

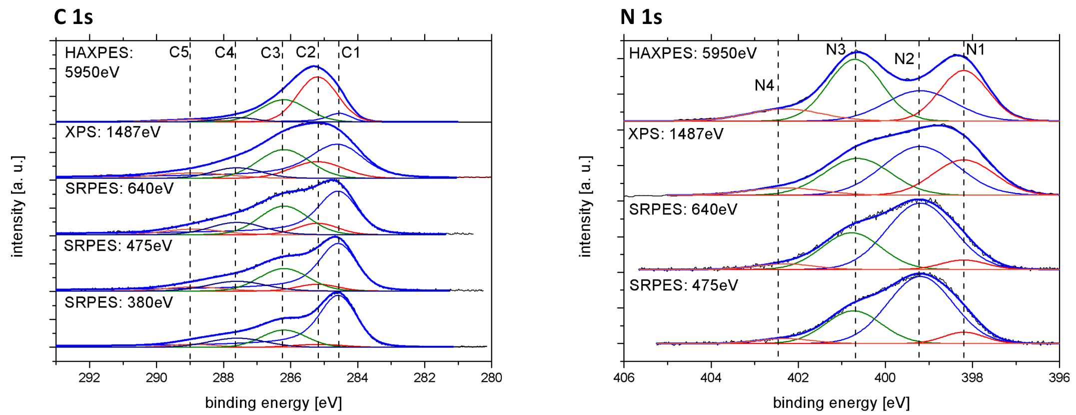

cerium oxide deposition

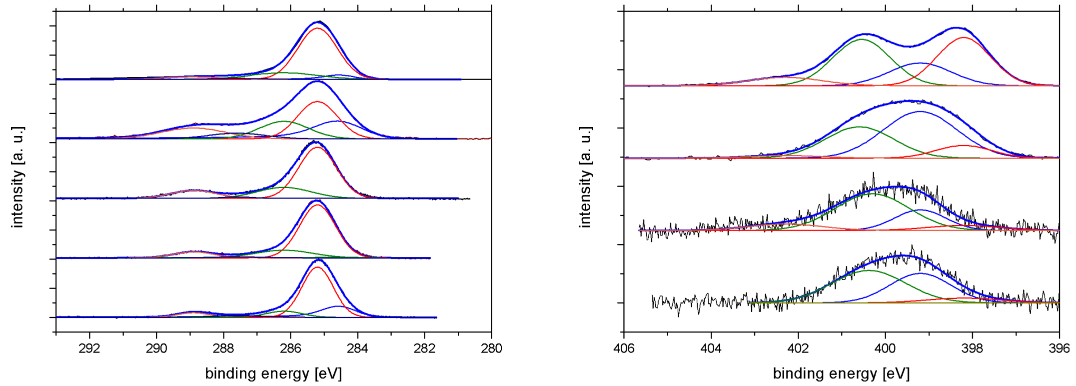

Figure 11.9: Summary of the C 1s and N 1s spectra of the cerium oxide covered CN_x-50% film; the spectra of the as-prepared film are shown for comparison. The spectra are normalized to the same height.

CN_x-100%

as-prepared

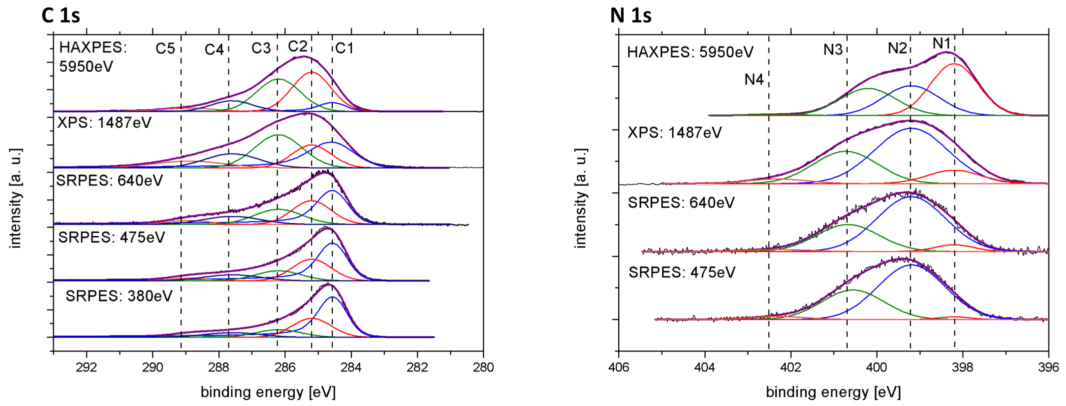

cerium oxide deposition

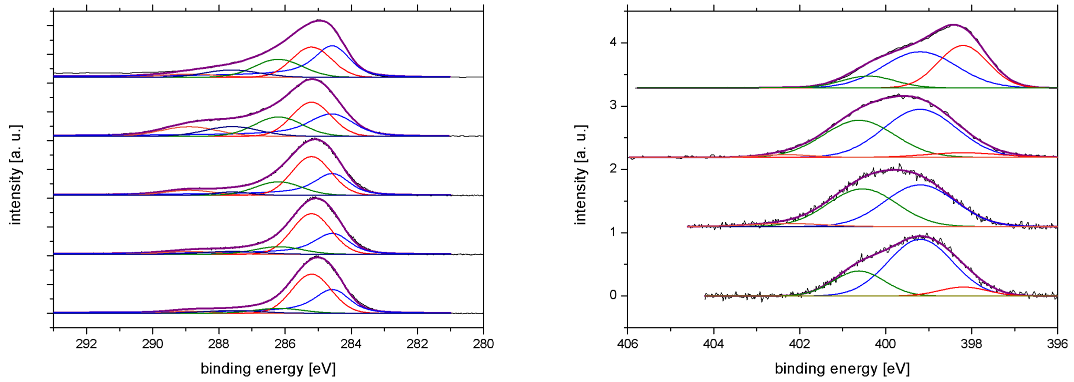

Figure 11.10: Summary of the C 1s and N 1s spectra of the cerium oxide covered CN_x-100% film; the spectra of the as-prepared film are shown for comparison. The spectra are normalized to the same height.

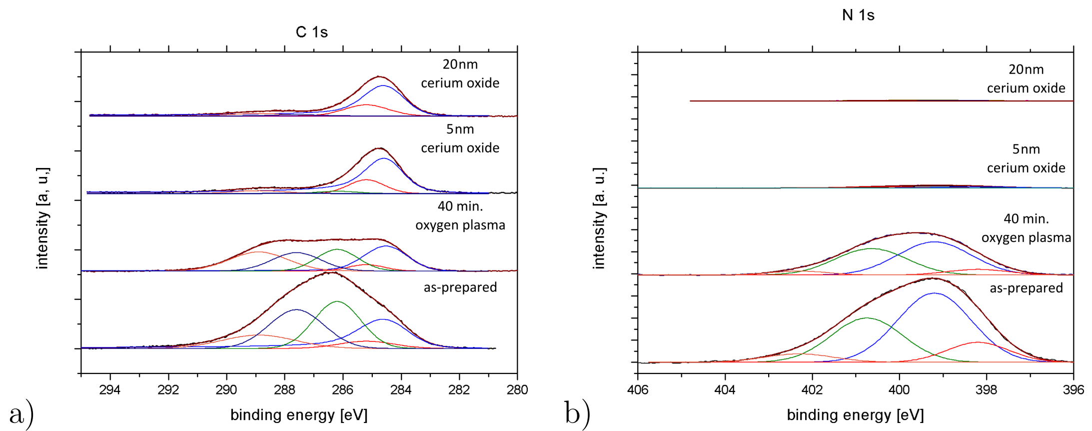

Figure 11.11: Summary of the a) C 1s and b) N 1s core level spectra of the CN_x-100%, h.p. film (as-prepared, after 40 min of oxygen plasma treatment and the deposition of a cerium oxide film with 5 nm and 20 nm thickness, respectively).

Chapter 12

Investigation of the as-prepared, oxygen plasma treated and cerium oxide covered carbonaceous films by means of NEXAFS

12.1 Information about the used samples and experimental techniques

In case of NEXAFS experiments, NEXAFS spectra were obtained by scanning the incident photon energy in the range of 280 — 310 eV and 390 — 420 eV, respectively, over the C K- and N K-absorption edges. Due to the maximum probing depth estimated to be 10 $\approx nm$, a complete series of a-C/CN_x double layers was prepared including the single layers a-C and CN_x-100%, h.p. (see tab. 4.3, p. 37). The NEXAFS C K- and N K- edges were recorded for all of the as-prepared and cerium oxide covered carbonaceous films as well as selected oxygen plasma treated ones. For comparison purposes, the C K-edge spectrum of HOPG[1] sample was added.

12.2 Results

The NEXAFS spectra of the C K- and N K- edges are shown in fig. 12.1 for as-prepared carbonaceus films (upper part of the figure), for the films after 10 min oxygen plasma treatment (middle part) and for the films after 2 nm cerium oxide deposition (bottom part).

Main features of the nitrogen edge. In the nitrogen-related spectra presented in fig. 12.1 on the right side, one can see that the general shape of the N K-edge does not change considerably with nitrogen concentration in the layers nor after the films treatment in plasma. In the π-region, three main peaks

[1] **H**ighly **O**riented **P**yrotlitic **G**raphite

labeled N1 (appearing at 398.7 eV), N2 (appearing at 399.5 eV) and N3 (appearing at 400.8 eV) are visible. Peaks at comparable energies can be found in the NEXAFS spectra presented in the literature by other authors for magnetron sputtered CN_x films [30, 63, 82]. These peaks can be assigned to the following bonding configurations:

$$\begin{aligned} \text{N1 (398.7)} &\iff \text{pyridine-like environment} \\ \text{N2 (399.5)} &\iff \text{nitrogen in nitrile group} \\ \text{N3 (400.8)} &\iff \text{graphite-like environment} \end{aligned}$$

Furthermore, peak N1 is correlated with the incorporation of hydrogen into the magnetron sputtered CN_x film according to [83] indicating a contribution of C=N–H bonds to this peak. The assignment of peak N3 as nitrogen in a graphitic environment is additionally supported by Shimoyama et al. [84], who performed a NEXAFS analysis on nitrogen-doped HOPG.

From the N K-spectra of the as-prepared films in the present study it can be deduced that a considerable fraction of nitrogen bound in a graphite-like environment (peak N3) appears only for the CN_x-5% film. In case of CN_x-25% and CN_x-50%, only a shoulder is visible at this N3 position, which even vanishes completely for the films deposited at higher nitrogen concentrations in the process gas indicating that a decreasing fraction of nitrogen is bound in this bonding configuration with increasing nitrogen concentration in the process gas. The same statement can be done for the oxygen plasma treated films. In this case, the peak N3 attributed to nitrogen in a graphite-like environment becomes stronger with respect to the other two peaks N1 and N2 in case of the CN_x-5% film indicating that this bonding configuration is more stable against the oxygen plasma. For the cerium oxide covered carbonaceous films, the N K- edges do not exhibit any peak/shoulder at the position of N3, except the films with low nitrogen content. On the other hand, these two spectra corresponding to the cerium oxide covered CN_x-5% and CN_x-25% films are noisy because of low signal intensity of the nitrogen edge, and thus it is difficult to make any accurate conclusions trom the spectra.

When focusing on the contribution N1, the N K-edge spectra of the as-prepared films show that peak N1 seems to increase with respect to peak N2 with increasing nitrogen concentration in the process gas. This observation indicates that the fraction of nitrogen bound in a pyridine-like environment increases with respect to nitrogen bound in nitrile groups. Another possible explanation is an increased hydrogen incorporation into the carbonaceous film. For the oxygen plasma treated films and for the cerium oxide covered carbonaceous films the pyridine-like environment seems to be suppressed due to the treatments.

The state N2 assigned to the nitrile bonds is dominating one in the most of the measured NEXAFS N K-edge spectra presented in fig. 12.1. It is surprising namely in case of the as-prepared films CN_x 5% or the films covered by cerium oxide, where according to the PES measurements a graphite-like environment prevails. The sharp strong peak assigned to nitrile structures was referred also by other authors on the samples containing only a small amount of nitrile bonds [68]. The sharpness of the peak N2 suggesting that it originated from a well-defined structure was confirmed by NEXAFS calculations [30]. It is probably

that this peak appears as strong in the π^* region although only a small fraction of N bonded as nitriles because the nitrile bond predominantly has π character with a large oscillator strengh [30].

Main features of the carbon edge. Contrary to the N K-edge spectra, the carbon edges of the carbonaceous films are very complex and require a fitting procedure in order to make detailed statements and conclusions. Nevertheless, up to six peak contributions are visible in the spectra. Peaks P1 and P3 can be attributed to π^* and σ^* resonances, respectively, of C—C bonds of carbon in a graphitic environment [55, 85]. The position of the π^* peak corresponding to the graphitic structure of the nitrogenated samples is found to be shifted to about 284.6 eV in agreement with BHATTACHARYYA et al. [36]. This shift can be explained in correlation with defects in the graphitic network and/or disordered graphite-like environments [82].

Peak P2 located at 288.4 eV can be very likely attributed to COOH and C=O bonds according to studies performed on SWCNTs [86] and graphene oxide [87]. The peak located at $\approx$ 286.6 eV (P4) can be very likely correlated with peak N2 in the NEXAFS N K-edge according to the literature [30, 82] and can be therefore attributed to triple bonds between carbon and nitrogen. In addition, peak P4 matches quite well the position of the peak observed in the C K-edge of commercially available acetonitrile presented by HITCHCOCK et al. [88] appearing at 286.9 eV. The peak appearing at 289.3 eV (P6) matches rather well a transition observed in pyridine [36, 89].

The observation of trends is difficult due to the large number of overlapping peaks. Nevertheless, it can be concluded that oxygen chemically reacts with the carbon atoms at the surface forming C—O bonds during oxygen plasma treatment and cerium oxide deposition, respectively. This effect seems to be much stronger for the CN_x films treated by the sputter deposition of cerium oxide, partially due to vanishing of the state P6 assigned to the pyridine-like structures.

Regarding peak P5 appearing at $\approx$ 287.8 eV, a peak at a similar position ($\approx$ 288 eV) appears in the CN_x-related study of JIMENEZ et al. [37]. The authors interpreted the peak as originating from metastable carbon nitride or a textbfcarbon oxynitride phase based on a carbon **sp^2 hybrid**.

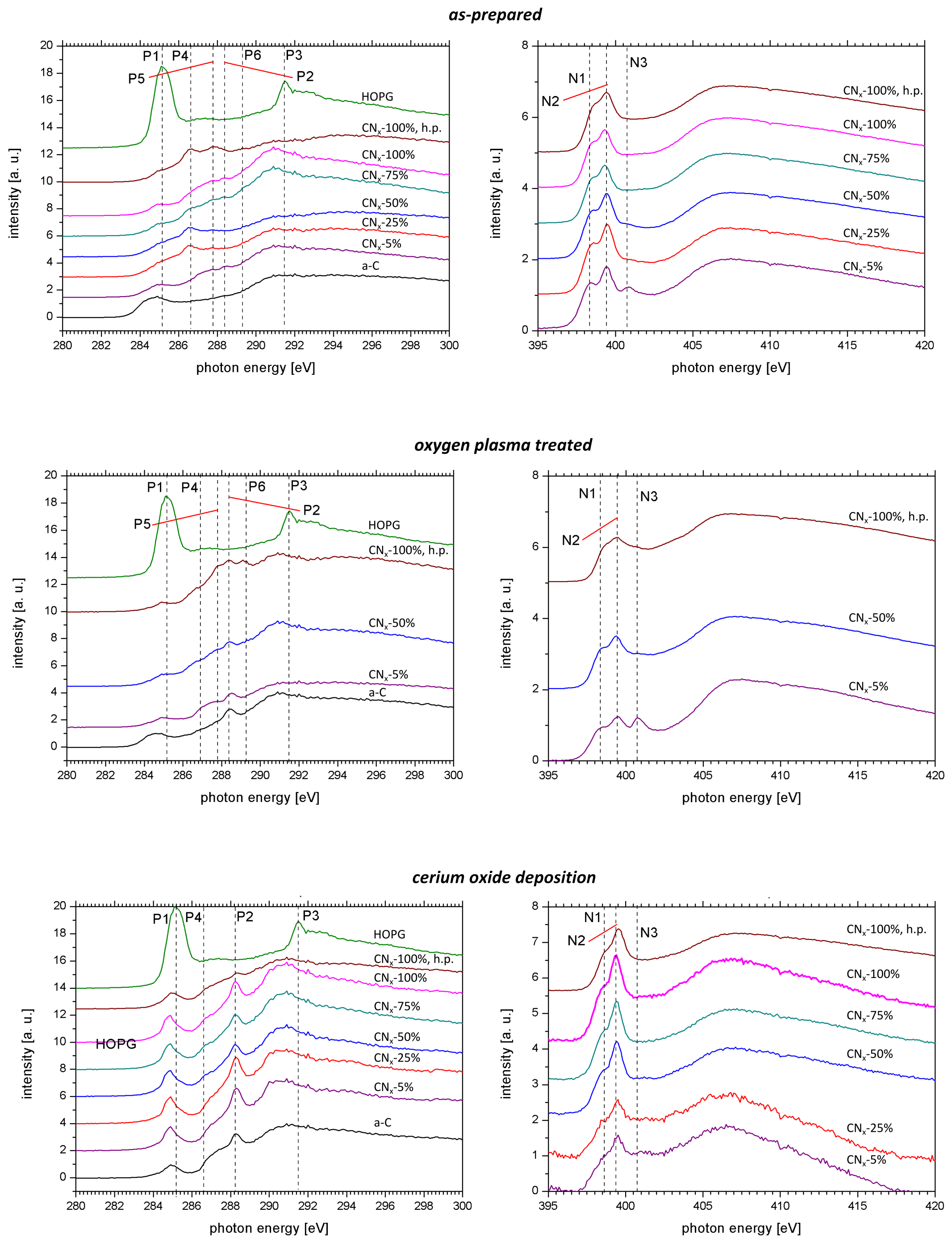

Figure 12.1: Absorption spectra of the as-prepared, oxygen plasma treated and cerium oxide covered carbonaceous films obtained from NEXAFS. Left: C K-edge; left: N K-edge.

Chapter 13

Summary of the main results obtained from the spectroscopic techniques

This chapter summarizes the most important observations obtained from the various spectroscopies and correlates the information obtained from NEXAFS with that ones delivered by the PES methods. Furthermore, a correlation between the chemical composition and the etching behaviour of the CN_x films in oxygen plasma is suggested.

13.1 Correlations between the PES and NEXAFS

Due to the surface sensitivity of the NEXAFS method (maximum information depth $\approx 10\,nm$), only the comparison between NEXAFS and the surface sensitive PES methods XPS and SRPES is usefull. The most important results obtained from the spectroscpic analysis can be summarized as follows:

- The a-C film consists mainly of sp^2 carbon. A smaller contribution of sp^3 carbon and/or C—H bonds could be found in the various spectra fig 10.1, p. 83. The bulk properties of the a-C film are not considerably influenced by oxygen plasma treatment or cerium oxide deposition in the presence of oxygen, respectively (fig. 11.1, p. 92).
- In case of the as-prepared CN_x films, several C—N bonding configurations could be detected. The comparison of the obtained PES and NEXAFS spectra with CN_x-related literature reveals the presence of three main bonding configurations: (i) N in graphite-like environment, (ii) N in pyridine-like environment and (iii) C—N triple bonds. The presence of C—N triple bonds, i. e. nitrile species, indicated by the PES spectra is supported by NEXAFS. Note that NEXAFS ranks among the methods able to distinguish this type of bonding environments unambiguously. In addition, the PES spectra deliver indications for the presence of (iv) pyrrolic N.
- According to the results obtained from the bulk method HAXPES, for the films CN_x-5% and — to a certain extend — CN_x-25% nitrogen is mainly

incorporated into the film in graphite-like environments (fig. 10.1, p. 83). The spectra give clear indications for the presence of a relatively ordered graphitic structure, which seems to become more disordered in the vicinity of the surface according to XPS and SRPES (fig. 10.2, p. 87 and 10.3, p. 88). A rather good correlation could be found for the as-prepared films between peak N3 (NEXAFS, fig. 12.1, p. 105) and N3 (XPS, fig. 10.2, p. 87 and 10.3, p. 88), both mainly associated with nitrogen in graphite-like environment: The corresponding peaks are strongest for the CN_x-5% film, decrease for the CN_x-25% and CN_x-50% ones, respectively, and are lowest for the CN_x-75% and CN_x-100% films. On the other hand, the strong peak N3 lying at lower binding energies in the PES spectra in case of the CN_x-100%, h.p. film might be explained with an increased presence of pyrrolic nitrogen rather than graphite-like N.

- The NEXAFS N K-spectrum of the oxygen plasma treated CN_x-5% films reveals a considerably stronger presence of nitrogen in graphite-like environment in comparison with the as-prepared film indicating that this bonding configuration is the most stable one against oxygen plasma.
- The surface-sensitive techniques NEXAFS and SRPES/XPS deliver clear indications of an enhanced presence of C—O bonds on the surface for the oxygen plasma treated and cerium oxide covered carbonaceous films. Accordingly, oxygen reacts chemically with the surface of the carbon film during both processes.

13.2 Correlations between the chemical composition and the etching behaviour of the CN_x films in oxygen plasma and cerium oxide deposition

It is noticable that the CN_x-5% and CN_x-25% film both exhibit a high resistance against oxygen plasma impact in comparison with the CN_x films deposited at higher nitrogen concentrations in the process gas, which finds expression in the etching rate comparable to the nitrogen-free a-C film (fig. 5.1, p. 40). This effect cannot be explained with considerations regarding the nitrogen concentration, because the CN_x-25% film exhibits a considerably higher nitrogen concentration in comparison with the CN_x-5% film according to EDX (fig. 8.3, p. 70). However, these are the two films which exhibit the highest fraction of nitrogen in a graphite-like environment in the bulk according to HAXPES (fig. 10.1, p. 83). Therefore, it can be concluded that CN_x films with a high portion of nitrogen in a graphite-like environment are most stable against oxygen plasma in comparison with structures containing a lower fraction of this bonding environment.

On the other hand, the lowest resistance against plasma etching exhibit the CN_x layers deposited at higher nitrogen content in the process gas, namely CN_x-100%, h.p.. Solely for this as-prepared sample, the PES C 1s core-level spectra exhibit a peak C4 in the bulk as well as in the near-surface regions, i. e. independently on the information depths of the used photon energies. For the CN_x-100%,

h.p. layer, this state vanishes in the surface regions after the oxygen treatment. Cerium oxide deposition leads to a complete degradation of the state also in the bulk of the sample. From overall developments of the presented PES and NEXAFS spectra, peak C4 initially related to several bonding environments (nitrile species, sp^3 C—N and/or sp^2 C—N bonds) can be preferentially associated to the latter bonding environment after all. These species are known to have the capability to form volatile gases such as N_2 and C_2N_2, which subsequently desorb, resulting in a film-surface etching commonly referred to as chemical sputtering [90].

Concluding remarks

Summary and conclusions

The present study is focused on the application of carbonaceous films, that is a-C and CN_x films, as interlayers for the fabrication of highly porous cerium oxide films on commercial flat silicon substrates. The morphology of the cerium oxide/carbon bilayers has been investigated by means of SEM and TEM. In addition, structural investigations of the carbonaceous films by means of various spectroscopic techniques have been performed. The most important results can be summarized as follows:

- The preparation of porous cerium oxide/carbon bilayers on silicon is possible, if carbonaceous interlayers in the form of a-C or CN_x films are used between the cerium oxide film and the silicon substrate. The formation of such porous structures requires the presence of an optimal amount of reactive species in the process gas. In this regard, argon/oxygen, argon/hydrogen and argon/water vapour gas mixtures can be used. The morphology of the final bilayer is strongly affected by the parameters of the cerium oxide deposition. In particular, this includes the concentration of the reactive gas component in the process gas, the cerium oxide deposition rate, the cerium oxide film thickness and the type of the used carbonaceous interlayer. The obtained bilayers exhibit compact, tree-like or noodle-like cross-sectional structures depending on the deposition conditions.

- High porosity of the cerium oxide/carbon bilayer is correlated with a large fraction of cerium in the 3+ oxidation state. This effect can be explained by the formation of smaller crystals of cerium oxide and the formation of cerium carbides. The highest fraction of Ce^{3+} was found near the interface between the cerium oxide films and the carbon support.

- It was found out that platinum-doping of the cerium oxide film via co-sputtering of platinum wires does not considerably influence the porous film growth when argon/oxygen is used as the process gas. The investigated films exhibited Pt concentrations up to 28%.

- The CN_x films prepared at the lowest nitrogen concentrations in the process gas exhibit a high fraction of nitrogen in graphite-like environments. These films exhibit a relatively high etching resistance against oxygen plasma, which can be explained with a high oxygen plasma resistance of this bonding configuration.

- Increasing amount of nitrogen in the process gas leads to the nitrogen incorporation into the CN_x films via the formation of pyrrole, pyridine and nitrile species.

- During cerium oxide deposition, etching of the carbonaceous support takes place. A correlation between the etching rate of the carbon support and the nitrogen concentration in the as-prepared CN_x films could be found.
- Indications of a considerable removal of nitrogen from the CN_x films during the cerium oxide deposition in the presence of oxygen could be found by means of XPS.
- The results clearly indicate that oxygen chemically reacts with the carbon atoms of the carbonaceous films during the cerium oxide deposition under the formation of C—O bonds. This result supports the hypothesis that carbon is etched during the deposition of cerium oxide under the formation of gaseous products containing carbon and oxygen.
- Indications were found regarding a low etching resistance of sp^2 C—N bonding configurations. This effect can be explained by the capability of this bonding environment to form volatile gaseous products, such as N_2 and C_2N_2 leading to an intense chemical etching of CN_x films with a high fraction of nitrogen bound in this bonding environment.

The obtained results deliver a possibility, how to prepare cerium oxide-based thin film catalysts with a large surface on silicon substrates. This has practical relevance for on-chip applications, where the use of this type of catalyst is required. Concrete applications might be gas sensors or micro fuel cells.

Look into the future

The next step towards the application of the layer systems investigated in the frame of this work is testing in a real fuel cell system. It has to be investigated to what extent the improved morphology of the CeO_x-Pt catalyst layer influences the output power of the fuel cell. Furthermore, a more detailed study of the growth mechanism of the porous cerium oxide/carbon bilayers would be interesting in order to answer open questions, e. g. why high concentrations of the reactive process gas components suppress etching of the carbonaceous support.

Bibliography

[1] S. Litster and G. McLean *Journal of Power Sources*, vol. 130, pp. 61 — 76, 2004.

[2] Y. Shao, G. Yin, and Y. Gao *Journal of Power Sources*, vol. 171, pp. 558 — 566, 2007.

[3] Y. Wang, K. Chen, J. Mishler, S. Cho, and X. Cordobes Adroher *Applied Energy*, vol. 88, pp. 981 — 1007, 2011.

[4] A. Trovarelli, *Catalysis by Ceria and Related Materials.* London: Imperial College Press, 2002.

[5] H. Idriss, M. Scott, J. Llorca, S. Han, W. Chiu, P.-Y. Sheng, A. Yee, M. Blackford, S. Pas, A. Hill, F. Alamgir, R. Rettew, C. Petersburg, S. Senanayake, and M. Barteau *CHEMSUSCHEM*, vol. 1, pp. 905 — 910, 2008.

[6] P. Sheng, W. Chiu, A. Yee, S. Morrison, and H. Idriss *Catalysis Today*, vol. 129, pp. 313 — 321, 2007.

[7] Y. Suchorski, R. Wrobel, S. Becker, B. Strzelczyk, W. Drachsel, and H. Weiss *Surface Science*, vol. 601, pp. 4843 — 4848, 2007.

[8] M. Václavů, I. Matolínová, J. Mysliveček, R. Fiala, and V. Matolín *J. Electrochem. Soc.*, vol. 156, pp. B938 — B942, 2009.

[9] V. Matolín, I. Matolínová, M. Václavů, I. Khalakhan, M. Vorokhta, R. Fiala, I. Píš, Z. Sofer, J. Poltierová-Vejpravová, T. Mori, V. Potin, H. Yoshikawa, S. Ueda, and K. Kobayashi *Langmuir*, vol. 26, pp. 12824 — 12831, 2010.

[10] K.-B. Min, S. Tanaka, and M. Esashi *J. Micromech. Microeng.*, vol. 16, pp. 505 — 511, 2006.

[11] G. Lu, C. Wang, T. Yen, and X. Yhang *Electrochemica Acta*, vol. 49, pp. 821 — 828, 2004.

[12] T. Pichonat and B. Gauthier-Manuel *J. Micromech. Microeng.*, vol. 15, pp. S179 — S184, 2005.

[13] R. Fiala, I. Khalakhan, I. Matolínová, M. Václavů, M. Vorokhta, Z. Sofer, S. Huber, V. Potin, and V. Matolín *J. Nanosci. Nanotechnol.*, vol. 11, pp. 5062 — 5067, 2011.

[14] I. Matolínová, R. Fiala, I. Khalakhan, M. Vorokhta, Z. Sofer, H. Yoshikawa, K. Kobayashi, and V. Matolín *Appl. Surf. Sci.*, vol. 258, pp. 2161 — 2164, 2012.

[15] I. Khalakhan, M. Dubau, S. Haviar, J. Lavková, I. Matolínová, V. Potin, M. Vorokhta, and V. Matolín *Ceramics International*, vol. 258, pp. 2161 — 2164, 2012.

[16] J. Lavková, I. Khalakhan, M. Chundak, M. Vorokhta, V. Potin, V. Matolín, and I. Matolínová *Nanoscale*, vol. 7, pp. 4038 — 4047, 2015.

[17] S. Haviar, M. Dubau, J. Lavková, I. Khalakhan, V. Potin, I. Matolínová, and V. Matolín *Sc. Adv. Mat.*, vol. 6, pp. 1278 — 1285, 2014.

[18] S. Aisenberg and R. Chabot *J. Appl. Phys.*, vol. 42, pp. 2953 — 2958, 1971.

[19] A. Grill *Diam. Rel. Mat.*, vol. 8, pp. 478 — 434, 1999.

[20] V. Kulikovsky, P. Bohac, F. Franc, A. Deineka, V. Vorlicek, and L. Jastrabik *Diam. Rel. Mat.*, vol. 10, pp. 1076 — 1081, 2001.

[21] J. Schwan, S. Ulrich, H. Roth, H. Ehrhardt, S. R. P. Silva, J. Robertson, R. Samlenski, and R. Brenn *J. Appl. Phys.*, vol. 79, pp. 1416 — 1421, 1996.

[22] C. Mortimer and U. Müller, *Das Basiswissen der Chemie*. Stuttgart: Georg Thieme Verlag, 2003.

[23] H. Haken and H. Wolf, *Atom- und Quantenphysik*. Berlin-Heidelberg: Springer-Verlag, 1990.

[24] F. Richter *Phys. Bl.*, vol. 52, no. 4, 1996.

[25] J. Robertson *Mat. Sci. Eng.*, vol. 37 4 — 6, pp. 129 — 289, 2002.

[26] Y. Lifshitz *Phys. Rev. Lett.*, vol. 62, pp. 1290 — 1293, 1989.

[27] M. Tamor and C. Wu *J. Appl. Phys.*, vol. 67 (2), pp. 1007 — 1012, 1990.

[28] M. Cohen *Phys. Rev. B.*, vol. 32, pp. 7988 — 7991, 1985.

[29] A. Liu and M. Cohen *Phys. Rev. B.*, vol. 41, pp. 10727 — 10734, 1990.

[30] N. Hellgren, J. Guo, Y. Luo, C. Søathe, A. Agui, S. Kashtanov, J. Nordgren, H. øAgren, and J.-E. Sundgren *Thin Solid Films*, vol. 471, pp. 19 — 34, 2005.

[31] G. Lazar, B. Bouchet-Fabre, K. Zellama, M. Clin, D. Ballutaud, and C. Godet *J. Appl. Phys.*, vol. 104, no. 073534, 2008.

[32] R. Kurt, R. Sanjines, A. Karimi, and F. Levy *Diam. Rel. Mat*, vol. 9, pp. 566 — 572, 2000.

[33] C. Ronning, H. Feldermann, R. Merk, H. Hofsäss, P. Reinke, and J.-U. Thiele *Phys. Rev. B*, vol. 58, pp. 2207 — 2215, 1998.

[34] W. J. Gammon, O. Kraft, A. C. Reilly, and B. C. Holloway *Carbon*, vol. 41, pp. 1917 — 1923, 2003.

[35] N. Hellgren, K. Macak, E. Broitman, M. P. Johansson, L. Hultman, and J.-E. Sundgren *J. Appl. Phys.*, vol. 88, pp. 524 — 532, 2000.

[36] S. Bhattacharyya, M. Lübbe, P. Bressler, D. Zahn, and F. Richter *Diam. Rel. Mat*, vol. 11, pp. 8 — 15, 2002.

[37] I. Jimenez, W. M. Tong, D. K. Shuh, B. C. Holloway, M. A. Kelly, P. Pianetta, L. J. Terminello, and F. J. Himpsel *Appl. Phys. Lett.*, vol. 74, pp. 2620 — 2622, 1999.

[38] S. Haviar, *Preparation and characterization of nanostructures for catalysis and gas detection.* PhD thesis, MFF UK in Prague, 2014.

[39] D. Hoffman, J. Thomas, and B. Singh, *Handbook of Vacuum Science and Technology.* Academic Press.

[40] J. Musil, P. Baroch, J. Vlček, K. Nam, and J. Han *Thin Solid Films*, vol. 475, pp. 208 — 218, 2005.

[41] S. Jäger, B. Szyszka, J. Szczyrbowski, and G. Bräuer *Surf. Coat. Tech.*, vol. 98, pp. 1304 — 1314, 1998.

[42] R. Egerton, *Physical Principles of Electron Microscopy.* New York: Springer Science + Business Media, 2007.

[43] B. Bhushan, ed., *Springer Handbook of Nanotechnology.* Berlin Heidelberg: Springer, 2010.

[44] R. Wirth *Chem. Geology*, vol. 261, pp. 217 — 229, 2009.

[45] N. Yao, *Focused Ion Beam Systems.* Cambridge: Cambridge University Press, 2007.

[46] D. Williams and C. Carter, *Transmission Electron Microscopy.* New York: Springer Science + Business Media, 2009.

[47] D. Briggs and M. Seah, eds., *Practical Surface Analysis*, vol. Auger- and X-ray Photoelectron Spectroscopy. Chichester and Frankfurt am Main: John Wiley & Sons and Otto Salle Verlag GmbH & Co, 1990.

[48] J. Vickerman and I. Gilmore, eds., *Surface Analysis The Principal Techniques.* Chichester: John Wiley & Sons, 2009.

[49] "http://www.lasurface.com/xps/imfp.php."

[50] S. Tanuma, C. Powell, and D. Penn *Surf. Interf. Anal.*, vol. 21, p. 165, 1993.

[51] "https://vuo.elettra.eu/services/elements/webelements.html."

[52] "www.kolibrik.net."

[53] T. Skála, F. Šutara, M. Škoda, K. Prince, and V. Matolín *J. Phys.: Condens. Matter*, vol. 21, no. 055005, 2009.

[54] A. Bianconi *Applic. Surf. Sci.*, vol. 6, pp. 392 — 418, 1980.

[55] J. Stöhr, *NEXAFS Spectroscopy.* Berlin-Heidelberg: Springer-Verlag, 1992.

[56] I. Ahmad, S. Roy, P. Maguire, P. Papakonstantinou, and J. McLaughlin *Thin Solid Films*, vol. 482, pp. 45 — 49, 2005.

[57] J. Ripalda, E. Roman, N. Diaz, L. Galan, I. Montero, G. Comelli, A. Baraldi, S. Lizzit, A. Goldoni, and G. Paolucci *Phys. Rev. B*, vol. 60, pp. R3705 — R3708, 1999.

[58] A. Mikmeková, M. Urbánek, T. Fořt, R. Di Mundo, and O. Caha *Adv. Mat. Res.*, vol. 6, pp. 3298 — 3304, 2012.

[59] Z. Czigany, J. Neidhardt, J. Brunell, and L. Hultman *Ultramicroscopy*, vol. 94, pp. 163 — 173, 2003.

[60] A. Trovarelli, C. de Leitenburg, M. Boaro, and G. Dolcetti *Catalysis Today*, vol. 50, pp. 353 — 367, 1999.

[61] L. Wu, H. Wiesmann, A. Moodenbaugh, R. Klie, Y. Zhu, D. Welch, and M. Suenaga *Phys. Rev. B*, vol. 69, no. 125415, 2004.

[62] J. Lavková, *Electron microscopy and spectroscopy study of nanostructured thin film catalysts for micro fuel cell application.* PhD thesis, MFF UK in Prague and Université de Bourgogne, 2016.

[63] N. Hellgren, M. Johansson, E. Broitman, L. Hultman, and J.-E. Sundgren *Appl. Phys. Lett.*, vol. 78, pp. 2703 — 2705, 2001.

[64] K. Boyd, D. Marton, S. Todorov, A. Al-Bayati, J. Kulik, R. A. Zuhr, and J. Rabalais *J. Vac. Sci. Tech. A*, vol. 13, pp. 2110 — 2122, 1995.

[65] S. Souto, M. Pickholz, M. Santos, and F. Alva *Phys. Rev. B*, vol. 57, pp. 2536 — 2540, 1998.

[66] P. Hammer, N. Victoria, and F. Alvarez *J. Vac. Sci. Technol. A*, vol. 16, pp. 2941 — 2949, 1998.

[67] E. Cappelli, D. Trucchi, S. Kaciulis, S. Orlando, A. Yanya, and A. Meyyi *Thin Solid Films*, vol. 519, pp. 4059 — 4063, 2011.

[68] N. Hellgren, M. P. Johansson, E. Broitman, L. Hultman, and J.-E. Sundgren *Phys. Rev. B*, vol. 59, pp. 5162 — 5169, 1999.

[69] J. Pels, F. Kaptejijin, J. Moulijn, Q. Yhu, and K. Thomas *Carbon*, vol. 33, pp. 1641 — 1653, 1995.

[70] Y. Wang, Y. Shao, D. Matson, J. Li, and Y. Lin *ACS Nano*, vol. 4, pp. 1790 — 1798, 2010.

[71] P. Tamilarasan and S. Ramaprabhu *J. Appl. Phys.*, vol. 117, no. 144301, 2015.

[72] R. Haerle, E. Riedo, A. Pasquarello, and A. Baldereschi *Phys. Rev. Lett. B*, vol. 65, no. 045101, 2001.

[73] J. Diaz, G. Paolicelli, S. Ferrer, and C. F. *Phys. Rev. B*, vol. 54, pp. 8064 — 8069, 1996.

[74] G. Barth, R. Linder, and C. Bryson *Surf. Int. Anal.*, vol. 6 — 7, pp. 307 — 311, 1988.

[75] B. Angleraud, N. Mubumbila, P. Tessier, V. Fernandez, and G. Turban *Diam. Rel. Mat.*, vol. 10, pp. 1142 — 1146, 2001.

[76] J. Majumdar, S. Das, T. Shripathi, and R. Hippler *Chem. Phys. Lett.*, vol. 524, pp. 62 — 67, 2012.

[77] A. Majumdar, S. Das, T. Shripathi, J. Heinicke, and R. Hippler *Surf. Sci.*, vol. 609, pp. 53 — 61, 2013.

[78] J. Shi, Y. Xu, and J. Yhang *Thin Solid Films*, vol. 483, pp. 169 — 174, 2005.

[79] P. Hammer and F. Alvarez *Thin Solid Films*, vol. 398 — 399, pp. 116 — 123, 2001.

[80] S. Rodil and S. Muhl *Diam. Rel. Mat*, vol. 13, pp. 1521 — 1531, 2004.

[81] S. Bhattacharyya, C. Cardinaud, and G. Turban *J. Appl. Phys.*, vol. 83, pp. 4491 — 4500, 1998.

[82] R. Gago, I. Jimenez, J. Neidhardt, B. Abendroth, I. Caretti, L. Hultman, and W. Möller *Phys. Rev. B*, vol. 71, no. 125414, 2005.

[83] B. Bouchet-Fabre, K. Zellama, C. Godet, D. Ballutaud, and T. Minéa *Thin Solid Films*, vol. 482, pp. 156 — 166, 2005.

[84] I. Shimoyama, G. Wu, T. Sekiguchi, and Y. Baba *Phys. Rev. B*, vol. 62, pp. R6053 — R6056, 2000.

[85] J. Diaz, S. Anders, X. Zhou, E. J. Moler, S. A. Kellar, and Z. Hussain *Phys. Rev. B*, vol. 64, no. 125204, 2001.

[86] A. Kuznetsova, I. Popova, J. T. J. Yates, M. J. Bronikowski, C. B. Huffman, J. Liu, R. E. Smalley, H. H. Hwu, and J. G. Chen *J. Am. Chem. Soc.*, vol. 123, pp. 10699 — 10704, 2001.

[87] A. Ganguly, S. Sharma, P. Papakonstantinou, and J. Hamilton *J. Phys. Chem. C*, vol. 115, pp. 17009 — 17019, 2011.

[88] A. Hitchcock, M. Tronc, and A. Modelli *J. Phys. Chem.*, vol. 93, p. 3068, 1989.

[89] J. Horsley, J. Stöhr, A. Hitchcock, D. Newbury, A. Johnson, and F. Sette *J. Chem. Phys.*, vol. 83, pp. 3146 — 3153, 1985.

[90] J. Neidhardt and L. Hultman *J. Vac. Sci. Tech. A*, vol. 25, pp. 633 — 644, 2007.

List of Figures

1.1 Growth model proposed for cerium oxide films prepared on an amorphous carbon on silicon via magnetron sputtering of a cerium oxide target using an argon/oxygen gas mixture as the process gas [17]. 11

1.2 Schematic view of the crystal structure of a) graphite and b) diamond (taken from [22]). 13

1.3 Schematic view a various C—N bonding configurations. 14

2.1 Schematic cross-sectional view of a common magnetron sputtering system. Some of the magnetic (red) and electric (blue) field lines are shown for illustration. 20

2.2 Schematic view of the construction used for introducing water vapour into the deposition chamber used for cerium oxide deposition. 22

2.3 Schematic view of the arrangement of the platinum wires on the cerium oxide target used for the deposition of platinum-doped cerium oxide films. 23

2.4 Schematic view of the glow discharge device used for the oxygen plasma treatment. 23

3.1 Dependence of the probability P that an electron excited at the distance d below the surface reaches the surface of the sample. The quantity d is given in units of the inelastic mean free path of the exited electron (figure taken from [49]). 28

3.2 Dependence of the PES information depth on the incident photon energy for 3λ. 28

4.1 Schematic view of the layer systems prepared for the study regarding the adhesion improvement of carbonaceous films on siicon substrates. 35

4.2 SEM micrographs of the various as-prepared CN_x films. 38

4.3 AFM images of the as-prepared a-C and CN_x-100%, h.p. film. The determined roughness values R_a are given below. 38

5.1 Determination of the etching rate of carbonaceous films on silicon substrates in oxygen plasma. Left: Schematic view of the sample used for the step-height measurement for the determination of the thickness of the layer etched off; right: Relative etching rate depending on the nitrogen concentration in the process gas. 40

5.2 Overview about the SEM micrographs of the various CN_x films treated in oxygen plasma for 20 minutes. 41
5.3 SEM micrographs amd TEM images of the oxygen plasma treated a-C and CN_x-100%, h.p. film for two different durations of plasma treatment. 42
5.4 AFM images of oxygen plasma treated a-C and CN_x-100%, h.p. film for two different durations of plasma treatment. 43
5.5 Roughnes values obtained from the AFM images for the a-C and CN_x-100%, h.p. film depending on the duration of oxygen plasma treatment. 44
5.6 SEM micrographs of untreated and oxygen plasma treated bulk substrates, namely the graphite foil and the nanoGDL. In case of the graphite foil, the corresponding AFM images are likewise given. 45

6.1 Relative deposition rate of cerium oxide depending on the oxygen partial pressure in the used process gas (total gas pressure 0.4 Pa). 47
6.2 SEM micrographs of 20 nm cerium oxide films on silicon substrates with either an a-C or CN_x-100%, h.p. interlayer deposited at various oxygen partial pressures in the process gas used for the cerium oxide deposition. For selected cerium oxide/CN_x-100%, h.p. bilayers, the corresponding TEM images are additionally shown. The cerium oxide deposition rate was 0.2 nm/min in all cases. 48
6.3 SEM micrographs of cerium oxide films deposited on silicon substrates with either the a-C or CN_x-100%, h.p. interlayer in dependence on the cerium oxide film thickness. The cerium oxide film was deposited in argon/oxygen with $p_{O_2} = 1$ mPa at the deposition rate of 0.2 nm/min. 51
6.4 SEM micrographs of 20 nm cerium oxide films deposited on silicon substrates with either an a-C or CN_x-100%, h.p. interlayer for various cerium oxide depositon rates. The used process gas was argon/oxygen with $p_{O_2} = 0.4$ mPa. 52
6.5 SEM micrographs of 10 nm cerium oxide films deposited on silicon substrates at $p_{O_2} = 1$ mPa with various carbonaceous interlayers at two different cerium oxide deposition rates. 53
6.6 Determination of the etching rate of carbonaceous films on silicon substrates during cerium oxide deposition for the various CN_x supports. Left: schematic view of the sample used for the step-height measurement; right: relative etching rate depending on the nitrogen concentration in the process gas used for the CN_x film preparation. 54
6.7 SEM micrographs of cerium oxide films with 10 nm thickness deposited in various argon/hydrogen gas mixtures. The cerium oxide deposition rate was ≈ 0.2 nm/min. 55

6.8 SEM micrographs of 20 nm cerium oxide films deposited on silicon substrates with either the a-C or CN_x-100%, h.p. interlayer in gas mixtures argon/water vapour with various partial pressures p_{H_2O}. For the cerium oxide/CN_x-100%, h.p. bilayers, the corresponding TEM images are additionally shown. The cerium oxide deposition rate was 0.2 nm/min. 57

7.1 SEM micrographs of 20 nm thick cerium oxide films doped with three different concentrations of platinum on various substrates. The micrographs corresponding to undoped cerium oxide are given for comparison. All films were deposited at 1 mPa oxygen partial pressure in the process gas and 0.2 nm/min deposition rate. 61
7.2 SEM micrographs of 20 nm cerium oxide films doped with two different concentrations of platinum on nanoGDL substrates (bare nanoGDL, nanoGDL with 200 nm CN_x-50% (double layer) or 200 nm CN_x-100%, h.p. (single layer), respectively). The cerium oxide films were deposited in argon/oxygen with $p = 1$ mPa; the deposition rate was 0.2 nm/min. 62

8.1 Schematic view of the EDX measurement on the CN_x films deposited on the graphite foil with a Pt interlayer. The first situation (1) is valid when Pt peaks are visible in the EDX spectrum. In case (2) the EDX signal originates only from the CN_x film and Pt is not visible in the spectrum. 65
8.2 EDX spectra of the CN_x-50% film deposited on the graphite foil with a 50 nm platinum interlayer for two different primary electron energies: a) Electron energy 3 keV — no platinum peaks are visible in the spectrum indicating that the signal originates exclusively from the CN_x film; b) Electron energy 10 keV — a strong platinum peak is visible indicating that part of the EDX signal originates from areas below the CN_x film. 69
8.3 Nitrogen concentration in the CN_x films depending on the nitrogen concentration in the process gas during film deposition determined from EDX, XPS and EELS. 70
8.4 Nitrogen concentration in the CN_x films either after 10 minutes of oxygen plasma treatment or the deposition of the cerium oxide film with 2 nm thickness in comparison with the corresponding as-prepared films determined from XPS. 70
8.5 Survey spectra of the CN_x100%, h.p. film. Left: as-prepared; right: after 10 minutes of oxygen plasma treatment. 71
8.6 Oxygen concentration prior to and after 10 minutes of oxygen plasma treatment determined from XPS. 71

9.1 Spectra Ce 3d of the 2 nm cerium oxide films deposited on a) a-C and b) CN_x-100%, h.p. in argon/oxygen at various oxygen partial pressures. The spectra have been normalized to the same height. . 74

9.2 Spectra Ce 3d of cerium oxide films deposited on a) a-C and b) CN_x-100%, h.p. in argon/oxygen at $p_{O_2} = 1$ mPa and 0.2 nm/min deposition rate. The cerium oxide film thickness is 2, 10 and 20 nm. The spectra have been normalized to the same height. 76
9.3 Spectra Ce 3d of a 2 nm cerium oxide films deposited on CN_x-100%, h.p. (top) and a-C (bottom), respectively. The spectra of the films deposited in argon/water vapour are compared with the spectra of the films prepared in argon/oxygen at the same partial pressure of the reactive gas component, which was 10 mPa. The cerium oxide deposition rate was 0.2 nm/min. The spectra have been normalized to the same height. 77

10.1 HAXPES a) N 1s and b) C 1s spectra of the as-prepared films deposited in various argon/nitrogen gas mixtures with nitrogen concentrations reaching from 0% to 100%. The spectra are normalized to the same height. 83
10.2 Summary of the C 1s (left) and N 1s (right) core-level spectra of the as-prepared carbonaceous films CN_x-5%, CN_x-25% and CN_x-50%. The spectra are normalized to the same height. 87
10.3 Summary of the C 1s (left) and N 1s (right) core-level spectra of the as-prepared carbonaceous films CN_x-75%, CN_x-100% and CN_x-100%, h.p.. The spectra are normalized to the same height. . 88

11.1 Photoelectron spectra of the as-prepared, oxygen plasma treated and cerium oxide covered carbonaceous films obtained from the HAXPES measurement. Left: C 1s spectra; right: N 1s spectra. The spectra are normalized to the same height. 92
11.2 HAXPES valence band (VB) spectra of the a) as-prepared and b) oxygen plasma treated carbonaceous films. 93
11.3 Summary of the C 1s core level spectra of the oxygen plasma treated a-C film (right); the spectra of the as-prepared film are shown for comparison (left). 94
11.4 Summary of the C 1s and N 1s core level spectra of the oxygen plasma treated CN_x-50% film; the spectra of the as-prepared film are shown for comparison. All spectra are normalized to the same height. 95
11.5 Summary of the C 1s and N 1s core level spectra of the oxygen plasma treated CN_x-100%, h.p. film; the spectra of the as-prepared film are shown for comparison. All spectra are normalized to the same height. 96
11.6 Summary of the a) C 1s and b) N 1s core level spectra of the CN_x-100%, h.p. film (as-prepared and after various durations of oxygen plasma treatment). 97
11.7 Summary of the C 1s spectra of the cerium oxide covered a-C film; the spectra of the as-prepared film are shown for comparison. The spectra are normalized to the same height. 98
11.8 Summary of the C 1s and N 1s spectra of the cerium oxide covered CN_x-5% film; the spectra of the as-prepared film are shown for comparison. The spectra are normalized to the same height. . . . 99

11.9 Summary of the C 1s and N 1s spectra of the cerium oxide covered CN_x-50% film; the spectra of the as-prepared film are shown for comparison. The spectra are normalized to the same height. . . . 100
11.10 Summary of the C 1s and N 1s spectra of the cerium oxide covered CN_x-100% film; the spectra of the as-prepared film are shown for comparison. The spectra are normalized to the same height. . . . 101
11.11 Summary of the a) C 1s and b) N 1s core level spectra of the CN_x-100%, h.p. film (as-prepared, after 40 min of oxygen plasma treatment and the deposition of a cerium oxide film with 5 nm and 20 nm thickness, respectively). 101

12.1 Absorption spectra of the as-prepared, oxygen plasma treated and cerium oxide covered carbonaceous films obtained from NEXAFS. Left: C K-edge; left: N K-edge. 105

List of Tables

3.1 Summary of the photoionization cross-sections for the used photon energies taken from the ELETTRA homepage [51]. 29

4.1 List of the deposited thick CN_x films. 33
4.2 List of the prepared films regarding the solution of the delamination problem. Additionally, it is given whether delamination was observed or not (yes/no). A — means that the corresponding type of the carbonaceous film was not considered. 36
4.3 Overview about the carbonaceous films prepared for the present work. The labels are used in the whole thesis. The total gas pressure refers to the deposition of the top layer in case of the double layers. 37

7.1 Summary of the Pt concentrations depending on the number of the used Pt wires determined with XPS. 59

10.1 List of the types of photoelectron spectroscopies and primary photon energies used for depth profiling of the chemical composition of the CN_x films. The corresponding information depth calculated for the C 1s and N 1s electrons according to [49, 50] is given. . . . 84
10.2 Nitrogen concentrations in the as-prepared CN_x films for two different PES information depths. 86

Abbreviations

a-C	amorphous carbon
AFM	Atomic Force Microscope
CN_x	nitrogenated amorphous carbon
DC	direct current
EDX	Energy-dispersive X-ray Spectroscopy
EELS	Electron Energy Loss Spectroscopy
HAXPES	Hard X-ray Photoelectron Spectroscopy
GDL	Gas Diffusion Layer
NEXAFS	Near-edge X-ray Absorption Fine Structure Spectroscopy
PES	Photoelectron Spectroscopy
RF	Radio-frequency
SEM	Scanning Electron Mircrocopy
SRPES	Synchrotron-Radiation Photoelectron Spectroscopy
TEM	Transmission Electron Microscopy
XPS	X-ray Photoelectron Spectroscopy

Poděkování

Na tomto místě bych rád poděkoval všem, kteří k této práci přispěli. Na prvním místě děkuji Ivě Matolínové za vedení práce a konzultační činnost během studia. Zejména bych chtěl vyzdvihnout časově náročné zpracování dat z PES. Dále děkuji následujícím lidem, kteří mě podpořili experimentální činností a ochotně se mnou sdíleli své znalosti:

- AFM: Ivan Khalakhan
- XPS (Praha): Tomáš Duchoň, Marie Aulická, Misha Vorohta
- XPS, SRPES, NEXAFS (Elettra): Iva Matolínová, Tomáš Skála, Nataliya Tsud, Klára Ševčíková, Sofia Bercha, Misha Vorohta
- TEM+FIB: Valerie Potin, Jaroslava Lavková

V neposlední řadě chci poděkovat Standovi Haviarovi, který mi svou ochotou a přátelskou povahou výrazně usnadnil první kroky na této katedře. Na závěr děkuji všem, kteří mě během studia podpořili, ať už to bylo vědeckou konzultační činností nebo povzbuzujícími slovy.